DOES BONE-TO-CARTILAGE FLUID TRANSPORT EXIST AND IS IT RELEVANT TO JOINT HEALTH?

by

Brady David Hislop

A dissertation submitted in partial fulfillment
of the requirements for the degree

of

Doctor of Philosophy

in

Mechanical Engineering

MONTANA STATE UNIVERSITY
Bozeman, Montana

January 2024

DEDICATION

To Mom, Dad, Cali, Jeff and Lisa, thank you for everything, I would not be here without your belief.

VITA

Brady David Hislop was born in Kalispell, Montana on February 7th, 1996. He attended Polson High School and graduated in 2014. He went on to receive his Bachelor of Science in Mechanical Engineering in 2019 from the University of Idaho.

TABLE OF CONTENTS

TABLE OF CONTENTS CONTINUED

TABLE OF CONTENTS CONTINUED

TABLE OF CONTENTS CONTINUED

TABLE OF CONTENTS CONTINUED

LIST OF TABLES

Table Page

LIST OF FIGURES

Figure Page

LIST OF FIGURES CONTINUED

Figure Page

LIST OF FIGURES CONTINUED

Figure Page

LIST OF FIGURES CONTINUED

Figure Page

LIST OF FIGURES CONTINUED

Figure Page

LIST OF FIGURES CONTINUED

Figure Page

LIST OF FIGURES CONTINUED

Figure Page

LIST OF FIGURES CONTINUED

Figure Page

ABSTRACT

Osteoarthritis (OA) afflicts millions of people each year. The onset of OA has been associated with many factors including increased bone-cartilage fluid transport, yet a cure remains elusive. To implicate bone-cartilage fluid transport in the progression of OA, further studies are needed on fluid transport in health. Recent studies have challenged the assumption that no fluid transport occurs between bone and cartilage in healthy joints. However, many gaps remain in our understanding of bone-to-cartilage fluid transport, including 1) do fluid pressure gradients develop at the bone-cartilage interface, 2) do traumatic injuries impact subchondral bone stiffness, and synovial fluid metabolism 3) do larger molecules move from bone-to-cartilage and does cyclic loading enhance such movement, 4) what material properties influence bone-to-cartilage fluid transport 5) do distinct metabolism changes occur with osteoarthritis, evaluated using a novel clustering method. Our results showed the development of fluid pressure gradients at the osteochondral interface, and that cyclic compression enhances bone-cartilage fluid transport. Furthermore, our results showed that proteoglycan loss, and decreased subchondral bone stiffness increased bone-cartilage fluid transport. Finally, we showed that in the first week after traumatic joint injuries (e.g., ACL tears) subchondral bone volume decreases, and subchondral bone stiffness increases, while the synovial fluid metabolism shifts. In conclusion, we showed that osteochondral fluid transport is enhanced by cyclic compression for larger molecules than previously studied (3kDa dextran), and that material parameters changes associated with the progression of OA alter bone-cartilage fluid transport. These studies provide novel understanding of bone-to-cartilage fluid transport, leading us one step closer to understanding OA as a whole joint disease.

INTRODUCTION

Our joints provide us with the ability to perform many actions with ease including walking, running, jumping, throwing, lifting and many other activities. A key player in these amazing capabilities is fluid within our joints. Fluid is found within joint tissues, between articulating surfaces, and helps with lubrication, load support and nutrition transport. However, as we age, suffer injuries, and/or become obese to name a few factors our joints begin to degrade, leading to altered fluid movement and properties. These alterations to fluid properties can lead to stiffer joints, mixing of bone and cartilage fluid environments, and lessened mechanical support, each of which can lead to increased joint degradation. Yet the potential for altered fluid movement particularly between bone and cartilage to lead to joint degradation is understudied. Therefore, we need to address critical gaps in our understanding bone-cartilage fluid transport in health and disease to mitigate joint degradation. These gaps include how fluid moves between bone and cartilage and how bone structure changes in response to joint injury. Another gap is how the metabolism of synovial fluid, which interfaces with bone and cartilage, changes in response to joint injury. By addressing these critical gaps, we will provide improved understanding of fluid movement between bone and cartilage in health and disease. Further, results from addressing these gaps may point to potential therapeutic targets (**Figure 1.1**).

To address the critical gaps above we performed five studies. 1) we modeled fluid pressure gradients in an osteochondral core, 2) we quantified the deterioration of mechanical and structural properties of subchondral bone, and the dysregulation of synovial fluid metabolism, 3) we quantified the transport of 3kDa dextran molecules from bone-to-cartilage during cyclic compression, 4) we modeled the movement of fluid from bone-to-cartilage during cyclical

compression, 5) we developed a novel untargeted metabolomics workflow to identify the metabolites which consistently co-cluster. These studies showed that fluid pressure gradients developed at the bone-cartilage (i.e., osteochondral) interface. Subchondral bone loss occurs, is driven by catabolism, and distinct metabolic profiles arise in synovial fluid within a week of traumatic joint injuries. Cyclic compression enhances fluid transport from bone-to-cartilage and is driven by fluid pressure gradients. Combining multiple clustering solutions together using ensemble clustering combined with clustering optimization improves the identification of the underlying groups in the data.

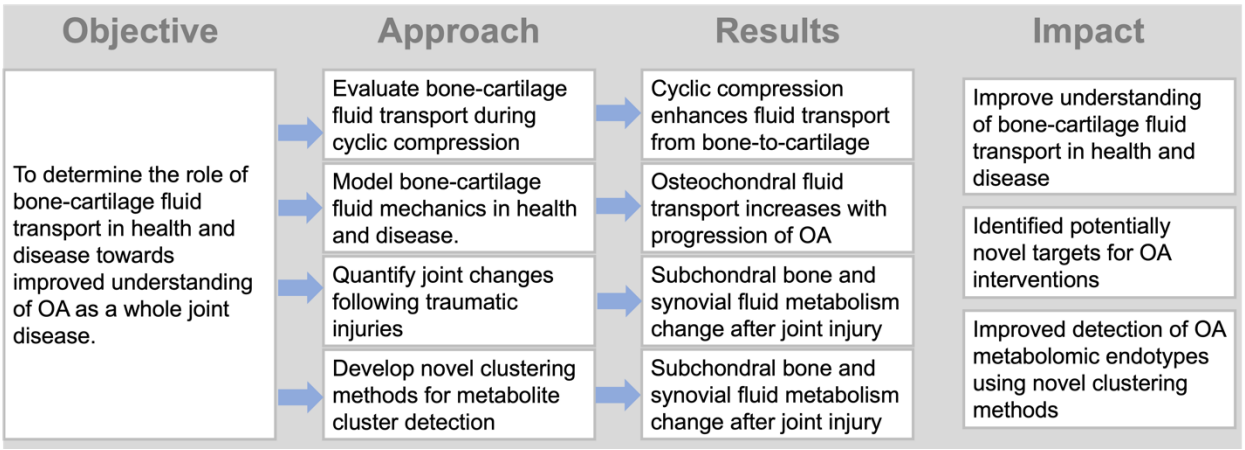

Figure 1.1 Schematic of dissertation studies. Outlining the overarching objective, approaches taken to achieve objective, results, and the impact of these studies.

Chapter 2 provides detailed background on key tissues, diseases, and methodologies for the studies performed for this dissertation.

Chapter 3 outlines the use of a finite element model of an osteochondral core, for the study of fluid pressure gradients at the osteochondral interface. The main goal of this study was to elucidate the mechanics driving the transport of fluid between bone and cartilage.

Chapter 4 addresses the early subchondral bone changes in mice hind limbs following a traumatic injury. In this study we show that subchondral bone, and the synovial fluid metabolic profiles change within 7 days of injury.

Chapter 5 demonstrates that convective fluid transport is a pathway through which cartilage receives fluid. These studies create a new paradigm in our understanding of how cartilage receives its fluid, and ultimately its nutrients.

Chapter 6 expands on the finite element model of Chapter 1 by incorporating new cartilage constitutive models and performing a sensitivity analysis. This chapter addresses the critical gap in our understanding of how mechanical changes to bone and cartilage, impact fluid transport between the tissues.

Chapter 7 demonstrates how the selection of different clustering methods impact the groups discovered within a data set. This chapter outlines a novel method for determining the optimal groups within a data set.

Chapter 8 provides concluding comments on the studies outlined in this document. This chapter also discusses future directions for each study presented.

CHAPTER TWO

BACKGROUND

2.1 Articular Cartilage

2.1.1 Overview

Articular cartilage (AC) is complex avascular biological tissue that allows for joint articulation, with extremely low frictional coefficients ($\mu<0.01$) allowing for smooth movement[1]. Furthermore, AC is responsible for distributing the high compressive loads seen in our joints, ensuring minimal damage is incurred during loading bouts [2, 3]. Thus, the loss of articular cartilage function is directly tied to the progression of OA.

2.1.2 Structure

AC is made up of 60-85% water and electrolytes, 10-20% type II collagen, and 5-10% proteoglycans [4]. Within this complex structure reside chondrocytes, the sole cells within cartilage, which make up ~5-10% by volume of the tissue. Structurally AC varies with depth from the articular surface. This depth-dependent structure is typically considered to have three layers, the superficial, middle, and deep zones. Each of these zones has a distinct collagen fiber orientation, proteoglycan content, and amount of water.

The superficial zone of AC represents the top ~15% of the tissue. This region of AC contains approximately ~85% water and electrolytes, with the remaining ~15% split between type II collagen and proteoglycans. Type II collagen within this region is parallel to the articular surface, and the chondrocytes a flatter phenotype.

The middle zone of AC represents ~55% of the tissue. This region can be thought of as a transition region with water content varying from ~83% down to ~74.5% near the deep zone of AC. The collagen fibers of this region or more randomly oriented, and the chondrocytes have shifted to a rounder phenotype.

The deep zone of AC represents ~30% of the tissue. Within the deep zone the water content varies from 70-74.5%, and the collagen fibers are perpendicular to the articular surface. Chondrocytes in this region have shifted towards a more hypertrophic phenotype and are found in columnar stacks.

2.1.3 Mechanics

The mechanics of AC are influenced by osmotic swelling, collagen fibrils, and the movement of water within the matrix [2, 3]. The modelling of cartilage responses to mechanical loading is considered in the section “Finite Element Modeling of the Osteochondral unit”. The osmotic swelling of cartilage is caused by the proteoglycans within the matrix [5]. In AC the most common proteoglycan is aggrecan, which is made up of a hyaluronic acid backbone with charged side chains[6]. Osmotic swelling creates a pre-stress on the collagen fiber network, helping support the large compressive joint loads [3].

The collagen fiber network plays a crucial role in cartilage mechanics [4, 7]. In an unloaded state, collagen fibrils are crimped (i.e., wavy) and support no mechanical load [4, 7]. In a loaded state, the collagen fibrils straighten out and begin to support tensile load seen on the tissue during large compressive loads [4, 7]. Furthermore, given the impermeable nature of the collagen fibrils fluid movement is easiest parallel to the collagen fibril orientation [8].

Interstitial fluid of AC is another critical component of the mechanical load support [2]. Fluid exudation is slowed by the proteoglycans, and directed by the collagen fiber orientation, leading to the pressurization of the cartilage tissue [2]. This pressurization protects chondrocytes from excessive mechanical loads.

The complex nature of articular cartilage mechanics creates different stress environments in zone of the tissue (e.g., superficial zone). This causes chondrocytes in each zone of articular cartilage to experience different strain magnitudes during loading [9]. Thus, within each layer of articular cartilage the chondrocytes will experience different mechanical signals, likely leading to different biological responses.

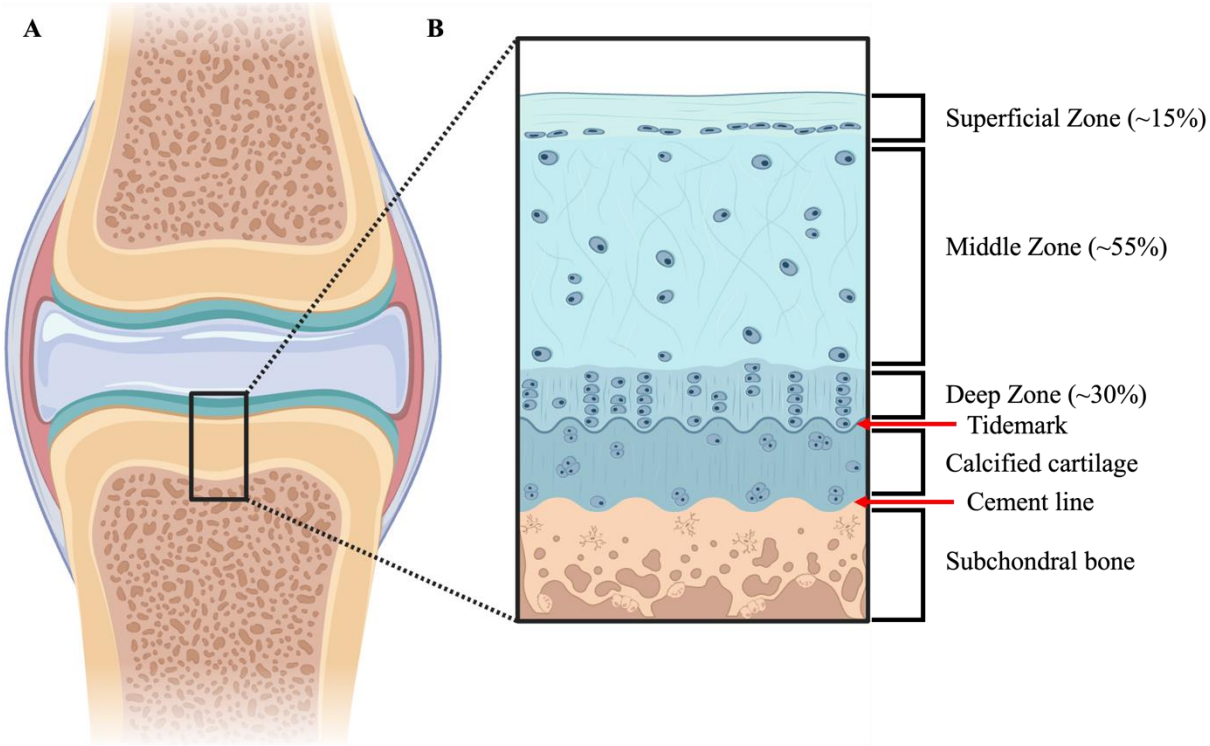

Figure 2.1 Schematic of coronal cross-section of knee joint, and osteochondral unit. A) Coronal cross section of healthy knee joint. B) Schematic of osteochondral unit in the joint, showing the three regions of uncalcified cartilage, the osteochondral interface, and subchondral bone. Figure created on BioRender.

2.1.4 Chondrocyte Mechanotransduction

The avascular nature of AC ensures that chondrocytes must rely on fluid movement for both mechanical stimulation and nutrients [10]. Chondrocytes are mechanically sensitive cells that respond to compressive loads, and fluid shear stresses [11-13]. This ability to "sense" their mechanical environment is thought to be driven by the pericellular matrix (PCM) that encapsulates chondrocytes [14]. The PCM is a thin region of tissue densely packed with proteoglycans (e.g., aggrecan, and decorin), and type II, VI, and IX collagen fibrils [14]. Furthermore, the PCM is thought to influence the mechanosensation of the chondrocytes in a zone-dependent manner [14]. Thus, changes to the PCM, and the extracellular matrix of cartilage could change mechanical forces and fluid environment experience by the chondrocytes likely metabolism [14].

2.2 Osteochondral Interface

The osteochondral interface separates subchondral bone from uncalcified cartilage [15] and plays a key role in transferring compressive loads from cartilage to subchondral bone [16]. This region of tissue contains the tidemark, calcified cartilage, and the cement line [15]. The tidemark is a thin (<5 μm) densely mineralized region that attaches uncalcified cartilage to calcified cartilage [17]. Calcified cartilage provides a transition from subchondral bone into articular cartilage [18].

Fluid transport across the osteochondral interface is a potential mechanism for cartilage nutrition [19, 20]. Until recently the osteochondral interface was considered impermeable to fluid transport, suggesting that cartilage received its nutrients solely from synovial fluid [10]. The impermeability was associated with the dense mineralization of the tidemark and calcified

cartilage. However, a recent study found that regions of uncalcified cartilage extended into bone marrow cavities providing a direct mechanism for osteochondral fluid transport [21]. Furthermore, recent studies have shown that small molecules diffuse from subchondral bone to cartilage [19, 20, 22]. In these studies, researchers investigated the ability of molecules from 376 Da to 1.55 kDa in size to diffuse from subchondral bone to uncalcified cartilage, establishing that osteochondral interface is permeable. In an expansion of their original studies, they also found an increased osteochondral fluid transport in OA joints [19]. These results suggest that osteochondral fluid transport occurs, but most biological molecules of significance are larger. Thus, in chapters 5 and 6 we expand on these results by studying the effects of cyclic compression on osteochondral fluid transport of a larger molecule than previously studies (3kDa Dextran).

2.3 Subchondral Bone

Subchondral bone plays a critical role in joint mechanics and biology. The structural support and mechanical properties of subchondral bone are important to joint homeostasis, as changes to bone volume, and mineralization can directly impact the loads incurred by articular cartilage [23]. Subchondral bone is highly metabolically active compared to articular cartilage [24, 25], due to its exposure to vasculature and fluid transport. Thus, to consider OA as a whole joint disease subchondral bone mechanics and biology, and the impact of subchondral bone on bone and cartilage mechanosensation need to be considered.

The subchondral bone plate is made of cortical bone and densely populated with osteocytes, the master regulators of bone remodeling [24, 25]. Osteocytes reside within lacunae that are connected to one another through a dense canalicular network[26]. The lacunar-

canalicular system (LCS) is the main conduit through which bone fluid transport occurs allowing osteocytes to communicate with each other [26]. In addition, bone is densely vascularized, providing bone cells with oxygen, hormones, growth factors and neurotransmitters [27]. Given the densely mineralized and low volume of water in bone and the dense vasculature of bone, the LCS and bone vasculature are likely the mechanisms through which osteochondral fluid transport can occur. Bone cells produce cytokines, proteases, and have direct supply of nutrients from vasculature [28, 29]. Thus, the transfer of any of these molecules from bone into cartilage could directly impact chondrocyte metabolism.

The subchondral bone epiphyseal region is found directly below the subchondral bone plate. This region is made up of trabecular bone and forms bone marrow cavities. Within the bone marrow cavities reside osteoblasts (bone forming cells), and osteoclasts (bone resorbing cells) [30]. Recent evidence suggests that uncalcified cartilage can be directly connected to bone marrow cavities [21] implicating these cavities as another potential mechanism for bone-to-cartilage fluid transport. Furthermore, after traumatic injuries subchondral epiphyseal bone volume decreases and does not recover with as OA progresses as the subchondral bone plate does. Thus, cavities from uncalcified cartilage to bone marrow cavities and structural changes to subchondral epiphyseal bone could alter bone-cartilage fluid transport.

Subchondral bone plate mechanical, structural and metabolic changes are early signs of the onset of OA [11, 13, 31-43]. Recent studies have shown that within 7 days of traumatic joint injuries the subchondral bone plate thins, and subchondral epiphyseal bone volume decreases [34, 42, 44-46]. Further work has shown that the initial loss of bone switches to a sclerotic phenotype as the joint progresses towards OA [34]. This shift to a sclerotic phenotype is thought

to be due to an imbalance in bone remodeling, which may be due to increase osteocalcin, in tandem with decreased calcitonin [47]. Importantly, it isn't known if bone modulus rapidly changes after injury, before the sclerotic phenotype occurs, we explore this question in chapter 3. Previous studies of OA have shown that subchondral bone hardness decreases compared to osteoporosis, suggesting a less mineralized bone matrix [48]. In tandem with these structural and mechanical changes studies have found distinct shifts in cortical bone metabolism, and synovial fluid metabolism, suggesting confounding effects of OA [37, 39]. These mechanical, structural, and metabolic changes to subchondral bone likely influence joint fluid mechanics.

2.4 Osteoarthritis

Osteoarthritis (OA) is the most prevalent disability worldwide affecting more than 500 million people each year [49], and costing health care systems billions of dollars [50]. To date patients typically undergo treatments that offset the need for total joint replacement but fail to cure the disease [51]. The lack of cure and financial burden of OA motivate the need to understand the pathology of OA.

Cartilage and bone undergo mechanical, structural and biological changes with the progression of OA. During the early stages of OA progression, cartilage loses proteoglycan content, especially in the superficial zone [52], impacting the permeability and mechanics of the tissue. As the OA progression continues cartilage experiences fibrillation, thinning and eventually bone on bone contact occurs [53]. Coupled with these mechanical and biological changes are distinct shifts in chondrocyte metabolism that likely impact OA progression [13, 52, 54]. Similarly, subchondral bone sees increases in permeability [55], and changes in subchondral

bone modulus with OA progression [56]. A potential explanation for these degenerative joint changes may be the restarting of the endochondral ossification process [57].

The onset of OA is a complicated puzzle that requires a great deal of further study. The above discussion covers just a few of the many potential mechanisms of this degenerative disease. However, many of these factors are entangled, for example, the mechanical changes to the joint will impact cellular metabolism, and the impacted metabolism will lead to further mechanical changes. Thus, to understand the pathology of OA the mechanical, structural, and biological changes of all joint tissues need to be understood.

2.5 Post-Traumatic Osteoarthritis

Post-traumatic osteoarthritis (PTOA) is a subset of the OA that is characterized by the onset of the disease after a traumatic injury. Recent studies have shown that upwards of 50% of people who tear their ACLs will develop OA in 10-20 years [58]. This is particularly troublesome for young athletes (e.g., college and high school athletes) as they are prone to develop PTOA in their 30s and 40s, long before they are eligible for total joint replacements. The onset of PTOA is not well understood. Many studies [11, 13, 31-43] have investigated the early response of our joints to such injuries, finding mechanical, structural, and biological shifts.

Subchondral bone loss occurs rapidly after traumatic injuries and could lead to the onset of PTOA[34, 39, 42, 44, 45]. Interestingly the subchondral bone shifts to a sclerotic phenotype as OA progresses in the joint [34]. Osteophytes also form as the joint progresses towards PTOA and are thought to be a mechanism the joint uses to try to offset mechanical changes to the joint [59]. Along with the structural changes to the joint, recent evidence has suggested that subchondral bone could increase in stiffness in the first week after injury, as we discuss in chapter 4.

Furthermore, studies suggest that following traumatic injuries both metabolic and mechanical shifts occur [37, 39].

Cartilage is also significantly impacted by traumatic injures with shifts in metabolism and mechanical properties [60]. Impact loads experienced during traumatic injures such as ACL ruptures and may be at the root of the onset of PTOA. These large nearly instantaneous loads can lead to cartilage microcracks and have been shown to lead to chondrocyte death within the impacted region [61], leading to the complete loss of regenerative ability. Cartilage also undergoes significant shifts in metabolism following traumatic injuries with increases in the expression of inflammatory markers such as MMP-3 [54]. Furthermore, recent studies including the study presented in chapter 4 demonstrate the distinct shift of synovial fluid within the first week of injury [39].

The driving force behind the rapid development of PTOA after joint injuries remains unknown. A potential but underexplored mechanism for the rapid development of PTOA is changes in bone-cartilage fluid transport. The effect of vascularization of cartilage, and increased bone-cartilage crosstalk are all established in OA [41, 47, 52, 54]. However, several critical gaps remain in our understanding of how bone-cartilage fluid transport is altered immediately after joint injury including 1) do microcracks across the bone-cartilage interface lead to influx of bone produced markers to cartilage? 2) does subchondral bone modulus change rapidly and does it impact bone-cartilage fluid transport? 3) does immediate mixing of the cartilage and bone fluid lead to shifts in metabolism? Bone-cartilage fluid transport remains understudied in both health and disease but could play a critical role in both. We investigate subchondral bone modulus for rapid changes, and model changes in bone-cartilage fluid transport in health and disease in

chapters 4 and 6. However, additional work is needed beyond these studies to understand the impact of bone-cartilage fluid transport changes in PTOA progression.

2.6 Finite Element Modeling of the Osteochondral Unit

Finite element modeling (FEM) is a numerical approach to solving complex continuous systems [62]. To solve these complex systems FEM discretizes a continuous system into a set of nodes. These nodes are connected and influence each other. Nodes make elements of finite size, thus, and each element can be assigned a set of parameters describing the expected response. After discretizing a geometry into finite elements, a set of boundary conditions must be specified, creating the boundary value problem.

Constitutive modeling is a numerical technique for describing physical systems that approximates responses by averaging over a finite region. In cartilage mechanics, the current state of the art model was proposed by Pierce et al. [2], incorporating the proteoglycan solid matrix, collagen fiber network, and interstitial fluid. To extend this model, Wang et al. [3] proposed the addition of osmotic swelling to solid strain energy function. Osmotic swelling is caused by the charged proteoglycans within the solid matrix. However, for the studies we present here we utilized 2016 model proposed by Pierce et al. [2]. In biphasic models such as the 2016 model the solid and fluid components are considered isochoric, thus, any volumetric changes occur through pore deformation with exudation of fluid. To model the proteoglycan solid matrix, Pierce et al. assumed a Neo-Hookean strain energy function. The collagen fiber fabric was modeled with an exponential fiber power law, which must be coupled with a solid matrix. Therefore, in this model the proteoglycan solid matrix and collagen fiber network were coupled.

Constitutive modeling of bone is much less developed than that of the cartilage. Osteochondral models often assume a rigid body for bone given bone's ~1000 times greater stiffness. However, recent studies have applied biphasic isotropic elastic [63], and biphasic poroelastic models to subchondral bone [64]. Further work is needed on the subchondral bone constitutive modeling.

2.7 Agglomerative Hierarchical Clustering

Degenerative joint changes associated with OA often coincide with shifts in joint biology [31, 32, 37, 39, 65-68]. To detect these biological shifts researchers, use omics techniques, which provide sensitive measurement of individual genes, transcripts, proteins, and metabolites [69]. A key question asked through these analyses is which biomarkers (e.g., metabolites) had similar responses. In order to identify these similar responses researchers, use clustering. Clustering is an unsupervised machine learning technique that identifies groups in high-dimensional unlabeled data, such as that from omics. Thus, through clustering researchers can identify groups of biomarkers, and patient endotypes associated with disease perturbations.

Agglomerative hierarchical clustering (AHC) combines variables into clusters until a single cluster containing all variables is obtained [70]. The AHC algorithm relies on a distance/dissimilarity measure and a linkage function. The distance/dissimilarity measure is defined as the pairwise difference (e.g., correlation) between variables in the data. After calculating the distance/dissimilarity AHC uses a linkage function to determine the order in which variables are combined into clusters. First, the linkage function creates a new cluster by combining the variables with the smallest pairwise distance/dissimilarity (i.e., the most similar variables in the data). Next, the distance/dissimilarities between the newly formed clusters and

the other clusters are updated using a criterion specific to each linkage function. These steps are repeated until a single cluster containing all variables is achieved. Finally, to select the clusters of interest a "flat cut" (see Chapter 7) is made into the tree-structure representing the AHC solution.

2.8 Clustering Optimization

Clustering is crucial technique for identifying biomarkers of interest [11, 13, 31, 32, 39, 71, 72]. As discussed in section 2.7, clustering allows researchers to identify variables (e.g., metabolites) with similar responses. Omics researchers often analyze the identified clusters for biological pathways, thus, selecting the optimal number of clusters is crucial. However, there is no one-size fits all clustering algorithm, suggesting that the selection of one algorithm over another will impact the resulting clusters. Therefore, a pitfall of clustering is the lack of consensus on which clustering algorithm to use, and how many clusters is appropriate. We address the challenge of clustering algorithm selection in chapter 7.

Clustering optimization techniques have been developed, to determine the optimal number of clusters for a given clustering algorithm [73-76]. To determine the optimal number of clusters, clustering optimization determines the closeness of variables in clusters (i.e., intra-clusters spread), and the separation of clusters (e.g., distance/dissimilarity between cluster centers). There are a broad range of clustering optimization techniques including the Silhouette width [75], Davies-Bouldin Index [74], Calinski-Harabasz index [73], and the PBM index [77]. However, most clustering optimization algorithms are simply a ratio of the closeness to separation or vice versa. Thus, the optimal number of clusters can be determined by generating a set of clustering solutions containing 2 – N clusters (where N must be less than half the number

of variables in the data), calculating the optimization index for each clustering solution, and finally determining which index is best (e.g., the maximum Silhouette width is optimal).

CHAPTER THREE

DEVELOPMENT AND ANALYTICAL VALIDATION OF A FINITE ELEMENT MODEL OF FLUID TRANSPORT THROUGH OSTEOCHONDRAL TISSUE

Contribution of Authors and Co-Authors

Manuscript(s) in Chapter(s) 1

Author: Brady David Hislop

Contributions: Model development and analysis, manuscript drafting, revision of manuscript

Co-Author: Chelsea M. Heveran

Contributions: Manuscript drafting, revision of manuscript

Co-Author: Ronald K. June

Contributions: Manuscript drafting, revision of manuscript

Manuscript Information

Brady David Hislop, Chelsea M. Heveran, Ronald K. June

Journal of Biomechanics

Status of Manuscript:
☐ Prepared for submission to a peer-reviewed journal
☐ Officially submitted to a peer-reviewed journal
☐ Accepted by a peer-reviewed journal
☒ Published in a peer-reviewed journal

Elsevier
Volume 123
https://doi.org/10.1016/j.jbiomech.2021.110497

Abstract

Fluid transport is critical to joint health. In this study we evaluate an unexplored component of joint fluid transport –fluid transport between cartilage and bone. Such transport across the cartilage-bone interface could potentially provide chondrocytes with an additional source of nutrients and signaling molecules. A biphasic viscoelastic model using an ellipsoidal fiber distribution was created with three distinct layers of cartilage (superficial zone, middle zone, and deep zone) along with a layer of subchondral bone. For stress-relaxation in unconfined compression, our results for compressive stress, radial stress, and effective fluid pressure were compared with established biphasic analytical solutions. Our model also shows the development of fluid pressure gradients at the cartilage-bone interface during loading. Fluid pressure gradients that develop at the cartilage-bone interface show consistently higher pressures in cartilage following the initial loading to 10% stain, followed by convergence of the pressures in cartilage and bone during the 400 s relaxation period. These results provide additional evidence that fluid is transported between cartilage and bone during loading and improves upon estimates of the magnitude of this effect through incorporating a realistic distribution and estimate of the collagen ultrastructure. Understanding fluid transport between cartilage and bone may be key to new insights about the mechanical and biological environment of both tissues in health and disease.

3.2 Introduction

Joint injuries frequently progress to debilitating osteoarthritis (OA), a leading cause of disability worldwide. For example, 40% of patients who experience a traumatic joint injury will

develop post-traumatic OA (PTOA) within 10 years [58]. Cartilage and subchondral bone serve as the key structural components of our joints, with cartilage serving as the load-bearing tissue and subchondral bone providing structural support. Cartilage is a smooth avascular tissue that relies on its surrounding environment for nourishment. The current paradigm for joint fluid transport is that cartilage receives its nutrients through the synovial fluid and lymph nodes [10]. By contrast, bone is vascularized, which allows the rapid transport of nutrients as well as cytokines [27].

It is possible that fluid is transported directly between bone and cartilage. This transport could potentially increase the nutrients and signaling molecules available to chondrocytes compared with transport from the synovial fluid and lymph alone. A previous study showed that following traumatic injuries cartilage lymph nodes experienced decreased fluid uptake [78]. These results suggest that other fluid transport mechanisms, such as transport between cartilage and bone, play a role in joint fluid transport. Imaging studies of the cartilage-bone interface show the transport of solutes *in vivo* between the subchondral bone and calcified cartilage [19, 20]. Further, a poroelastic finite element model demonstrated that joint loading and unloading promotes fluid movement between cartilage and bone [64]. However, specific gaps in knowledge still remain about how fluid is transported between these tissues.

The underlying mechanics responsible for fluid transport are still heavily debated, with differing results between models using either a viscoelastic solid matrix or poroelastic approach [64, 79, 80]. Prior models of cartilage mechanics either neglect collagen fibers or model collagen fibers in a simplified manner to reduce model complexity [64, 80]. Stender *et al* approximate collagen ultrastructure with an anisotropic fiber distribution. Here, we improve

upon this estimate by using an ellipsoidal fiber distribution [81, 82]. The ellipsoidal fiber distribution mimics the Benninghoff arcade geometry seen in articular cartilage with zone-dependent fiber orientation [83]. Incorporating this fiber distribution into an osteochondral fluid transport model is important because the orientation of collagen fibers influences the mechanical environment, and potentially fluid transport properties, of cartilage [81, 82, 84]. Additionally in this study, we use a viscoelastic solid phase. Many previous studies assume poroelasticity [64, 85] of the solid phase, but this assumption is challenged by observations of cartilage viscoelastic behavior in pure shear [86, 87]. A biphasic viscoelastic model was chosen with the goals of capturing the viscoelastic responses of the extracellular matrix and collagen fibers as well as the interactions between the solid phase and water.

The overall objective of this study is to develop a finite element model of cartilage-bone fluid transport for fluid pressure gradients and radial size effects [88]. We hypothesize that fluid is transported between cartilage and bone during physiological loading/unloading and is driven by cartilage elastic recoil. Therefore, the three goals of this study are: (i) develop a finite element model of fluid transport in osteochondral tissue mimicking an unconfined compression experiment at physiologically relevant loads (ii) validate the finite element model against established analytical solutions and experimental data; and (iii) quantify fluid pressure gradients at the cartilage-bone interface.

3.3 Methods

3.3.1 Model Geometry

Osteochondral cylinders (1-2 mm diameter and 4 mm height) were modeled in FEBio [89, 90] using quarter symmetry (**Figure 3.1**). Boundary conditions simulated confined

compression with impermeable boundaries and fixed displacements (zero displacement) perpendicular to each cut surface (perpendicular to x and y axes of Figure 1A). There are not constraints on the radial edges of the model. To minimize nonlinear effects and computational complexity, a single body geometry was selected with hexahedral and penta mesh elements. Spatially dependent cartilage and bone material models were defined according to a 50-15-25-10 percentage split of bone, deep, middle, and superficial cartilage zones, respectively, using an in-house MATLAB code (**Figure 3.1**).

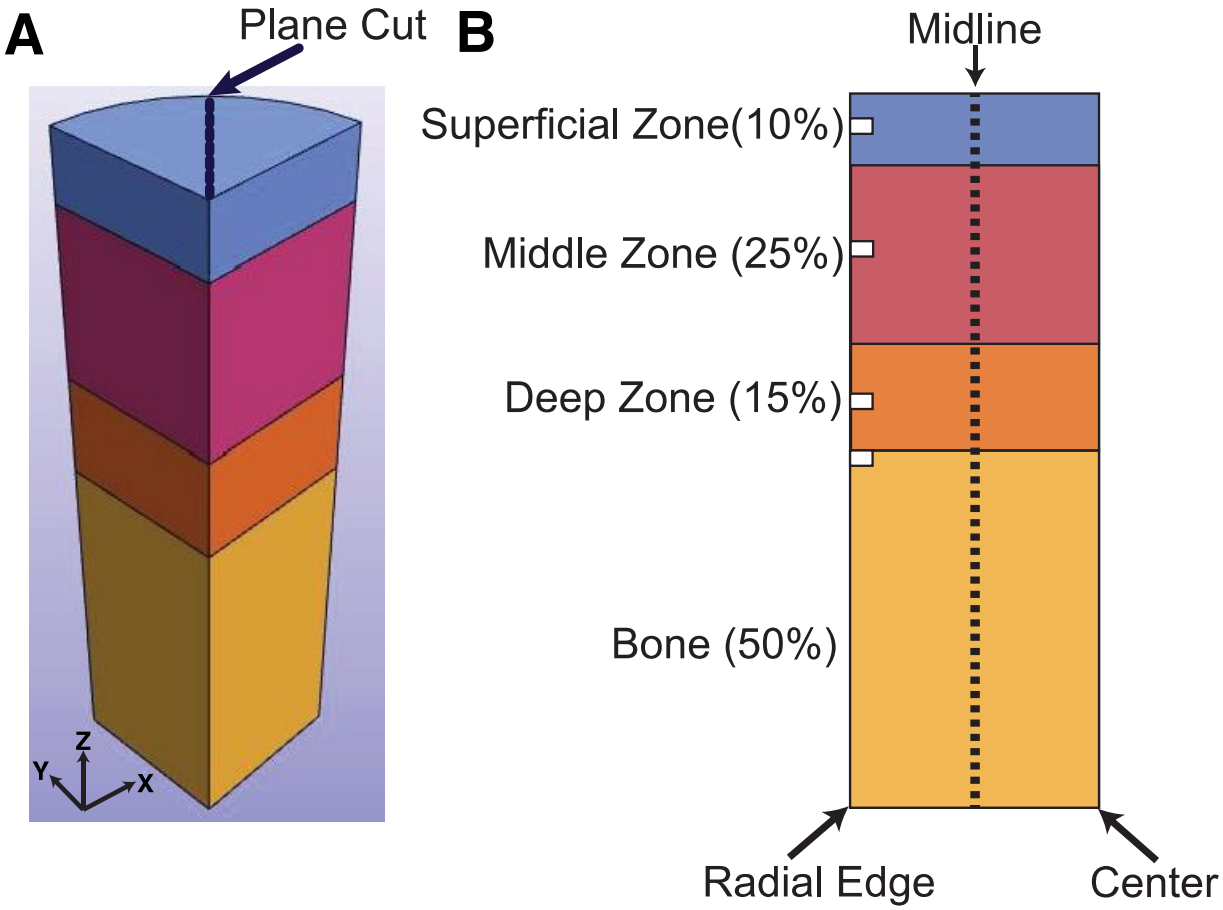

Figure 3.1 Finite element model of osteochondral tissue A) Mesh showing plane cut for evaluation; B) Schematic of cartilage layers and bone. White rectangles represent the locations analyzed in figures 3.2-3.5

3.3.2 Cartilage Constitutive Model and Material Properties

A viscoelastic neo-Hookean ellipsoidal fiber distribution model [81, 82, 84] was chosen for cartilage. Such modeling combines the tensile properties of collagen fibers and the biphasic viscoelastic response of the remaining matrix components and their bound water. The viscoelastic neo-Hookean model of the remaining matrix was applied to each layer of the tissue (v=0.499, relaxation time = 120s) [85]. A depth-dependent elastic modulus of the tissue was derived and applied to each layer of cartilage, using data from Walhquist *et al*. [91]:

$$E(MPa) = 5.839 - 5.7766Z + 4.0239Z^2 - 1.3551Z^3 \ (1)$$

where Z is the height from the cartilage-bone interface. In addition, an ellipsoidal fiber distribution [81, 82] was applied to each layer of cartilage independently with superficial zone fibers parallel to the superficial surface ($\beta = (2.5,2.5,2.5), \zeta = (4,4,2)$), middle zone fibers uniformly distributed ($\beta = (3.5,3.5,3.5), \zeta = (4,4,4)$), and deep zone fibers perpendicular to the superficial surface $\big(\beta = (2.5,2.5,2.5), \zeta = (2,2,4)\big)$, with β defining the elastic modulus along each axis, and ζ defining the spatial distribution of fibers. The elastic modulus of the fibers modeled in each layer of cartilage is independent of orientation (**Figure A2.D**). Whereas the spatial distribution of the fibers varies in each layer modeled. For example, to model the parallel fibers of the superficial zone we choose ellipsoid semi-axes of (4, 4, 2) which generates a disc-like ellipsoid with a greater distribution of collagen fibers orthogonal to the z-axes (**Figure A2.**). The spatial distribution of collagen fibers for each cartilage layer modeled can be seen in the supplemental information (**Figure A2.A-C**). The biphasic nature of the tissue was accounted for through the implementation of the Holmes-Mow permeability function [92], modeling the strain-dependent permeability of cartilage ($k_o = 6.2e^{-16}, M = 0.4, \alpha = 2.2$), where k_o defines the

initial permeability, α defines the rate at which permeability approaches zero, and M is constant for the exponential fit.

3.3.3 Bone Constitutive Model and Material Properties

Previous computational studies of the osteochondral tissues have modeled bone as a rigid body given the large difference in modulus between cartilage and bone (bone ~1000x greater). However, rigid body mechanics cannot be adapted for biphasic materials. Therefore, the bone was modeled as a biphasic isotropic elastic material (E= 17GPa, v= 0.29, φ= 5.5%) [93, 94] throughout the geometry. Isotropic elastic models are considered effective for modeling the mechanical properties of bone [93, 95] while allowing for the implementation of biphasic properties. Given the relatively low levels of bone deformation during the simulated loading, the bone permeability was set as spatially constant ($1e^{-17}$) [94].

3.3.4 Model Validation: Replication of Analytical Results and Fitting Experimental Data

Stress-relaxation was simulated using two simulation steps: a ramped compression step (0.1 seconds, 2 mm/s loading rate) followed by a hold at 10% strain for 400s. Vertical and radial mesh convergence studies were performed to determine the appropriate mesh size for this model. Effective fluid pressures of each mesh were studied to determine the appropriate mesh size, using a threshold of <5% change to determine convergence. Additionally, three radial sizes were studied (0.5, 0.75, 1 mm) to determine the effect of radius on the physical parameters of the model as predicted analytically [88]. Each model's results were analyzed for vertical and radial stress relaxation, effective fluid pressure relaxation, and differences in these physical parameters for the various radii to compare against validated analytical solutions [88]. Analytical predictions

included increased magnitude of compressive stress with increased radius. All results during this study were analyzed in PostView [89, 90] a post-processing software developed to support FEBio. All simulations were run on the Hyalite Cluster at Montana State University [96] using 8 cores and 4GB RAM per core to achieve rapid solutions (~4 hrs).

Experimental validation studies were performed by curvefitting the novel finite element model to published data. Data consisted of unconfined compressive stress relaxation experiments on twelve bovine explants of middle zone cartilage [97]. An ensemble average of the n=12 load curves was generated over the first 400 seconds of relaxation. We then modified the finite element model to simulate these experiments. Using the Levenberg-Marquardt optimization feature of FEBio, we minimized the difference between the model's predicted reaction force and the ensemble average reaction force from the experimental data by varying the material parameters in the model. These parameters were the stress relaxation time, the viscoelastic coefficient, and a scaling factor for eqn. (1). We compared the model fit to the ensemble data as well as the fitted parameters to literature values to assess the ability of the model to simulate experimental data.

3.4 Results

3.4.1 Mesh Convergence

Evaluation of the effective fluid pressure across three vertical mesh sizes (100, 200, 300 layers) revealed a <5% increase in effective fluid pressure between 100 and 200 layers, and 200 and 300 layers (**Figure A1.B**). Whereas, in the radial mesh study (8, 12, 16 radial slices) we saw increases in effective fluid pressure of 11.1% and 4.7% between 8 and 12, 12 and 16,

respectively (**Figure A1.A**). Given these results, we built our mesh with 8 theta segments, 12 radial slices, and 100-vertical layers.

3.4.2 Experimental Validation

To assess the accuracy of this model, the parameters are fitted to unconfined compressive stress relaxation data from middle-zone cartilage explants. The optimized parameters for stress relaxation time, the viscoelastic coefficient, and the scaling factor for elastic modulus captured the dynamics of unconfined stress relaxation of cartilage (**Figure 3.2**). The model estimated the peak load within 0.09 N (~5% error), while also capturing the equilibrium load (load experienced after 400 seconds of relaxation.) within about 0.01 N (~5% error). The model was less accurate in capturing the dynamics of the relaxation response. A key difference was that the model's initial response was much steeper than the data.

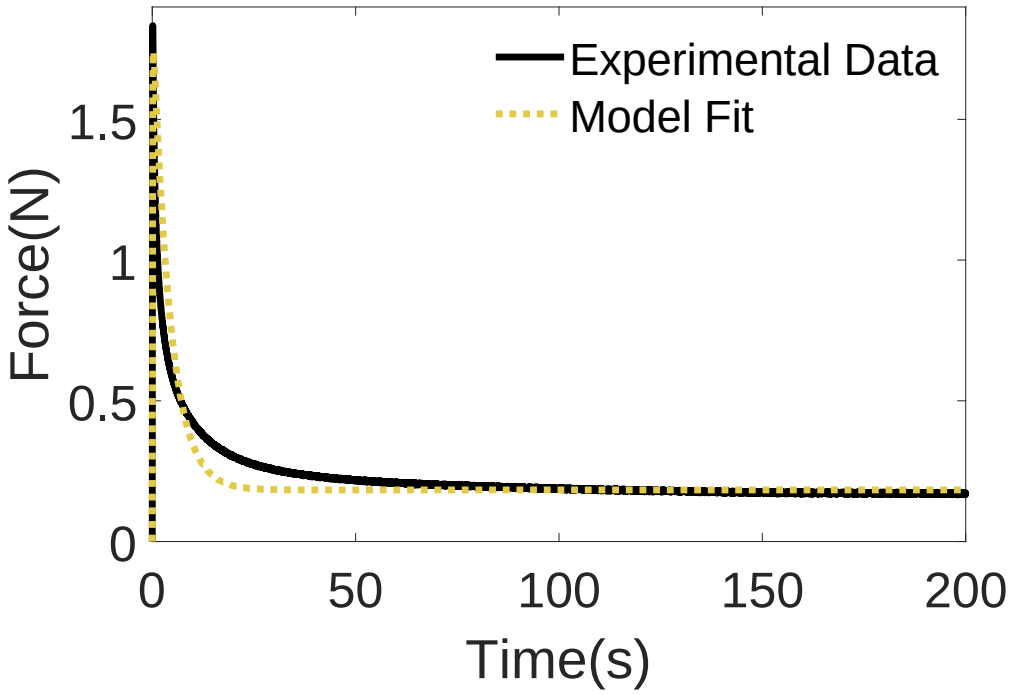

Figure 3.2 Validation of model against experimental stress-relaxation data [97].

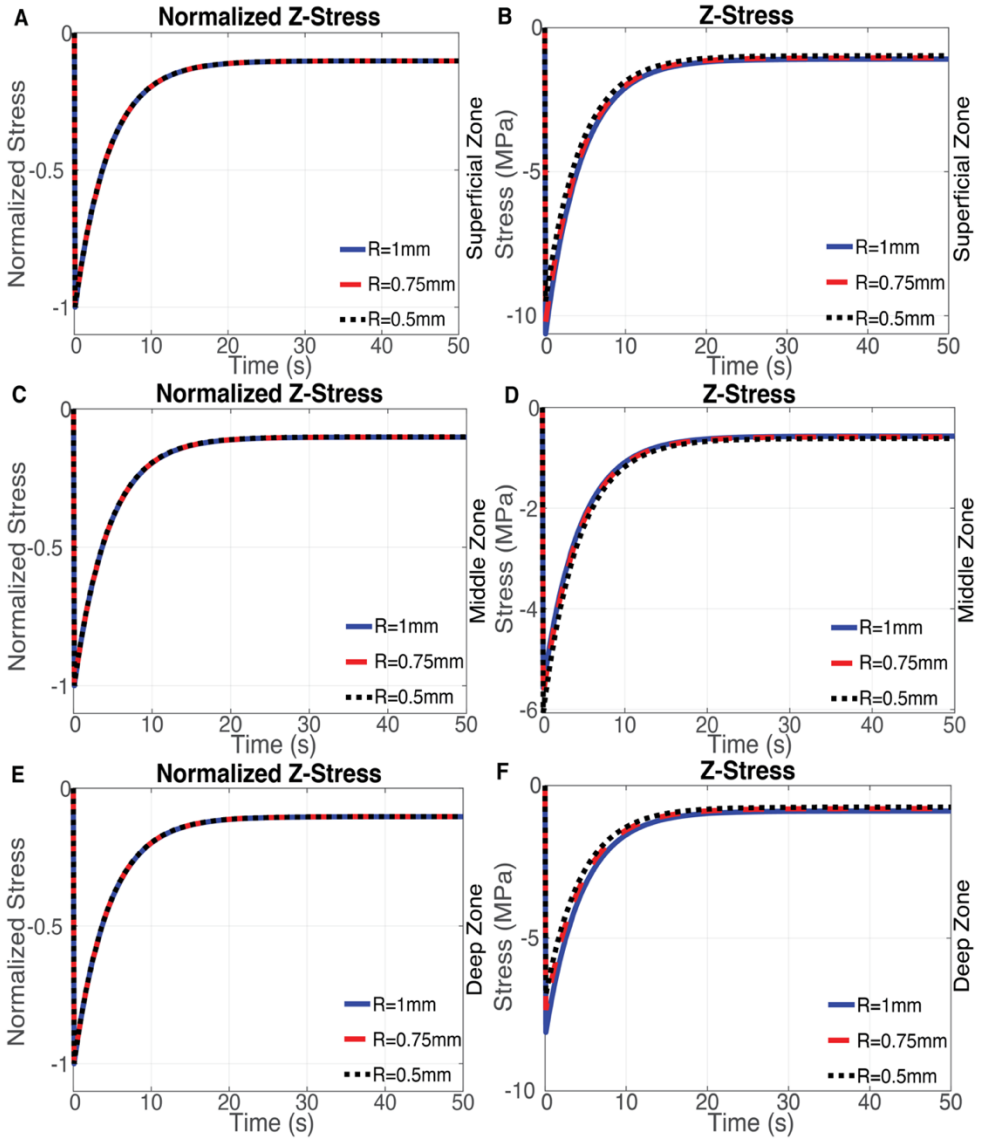

Figure 3.3 Compressive stress as a function of time for three radii. Normalized to peak compressive stress (left column) and absolute stress (right column) at location of interest and compressive stress at mid-depth of the superficial-zone (A-B), middle-zone (C-D), and deep-zone (E-F).

3.4.3 Compressive Stress Relaxation

Compressive stress relaxation in the z-direction was observed within both cartilage and bone elements. Detailed inspection along the radial edge revealed z-direction relaxation throughout each layer of cartilage (superficial, middle, and deep; **Figure 3.3A-F**). Further

evaluation revealed stress relaxation along the midline and center of the tissue for each layer. Additionally, stress relaxation was observed throughout the bone, with decreasing levels of compressive stress with depth from the cartilage-bone interface.

Radial mesh studies revealed identical relaxation profiles across each radial mesh size (1, 0.75 and 0.5 mm). We also found that levels of compressive stress had a direct relationship with decreases in radial mesh size. Suggesting that our mesh size is appropriate for modeling the expected decreases in compressive stress with reductions in the radius of the model.

Equilibrium compressive stress in the z-direction is proportional to the loading rate (Supplemental Figure 3). We found that with increases in loading rate from 0.2 mm/s to 2 mm/s, the compressive stress at peak load increased by 595 kPa. These results suggest that our model is capable of modeling the strain rate sensitivity of cartilage.

3.4.4 Radial Stress Relaxation

Radial stress relaxation at the radial edge (r=R) of cartilage was observed through each layer of the tissue. The middle zone of cartilage showed negative overall radial stress (**Figure 3.4C-D**), while the superficial zone showed an increase in radial stress from 0.5 mm to 1 mm (**Figure 3.4F**). Similar relaxation was seen at the radial edge of bone throughout most of the depth. However, near the bottom of the bone, a wave response was observed following the initial load.

Slight deviations in normalized relaxation profiles were observed between each radial mesh size in the deep zone of cartilage with the 0.5mm radius experiencing a delayed peak load and relaxation response (**Figure 3.4A**). Similar to the effective pressure and compressive stress radial stress has a direct relationship with decreases in radial mesh size.

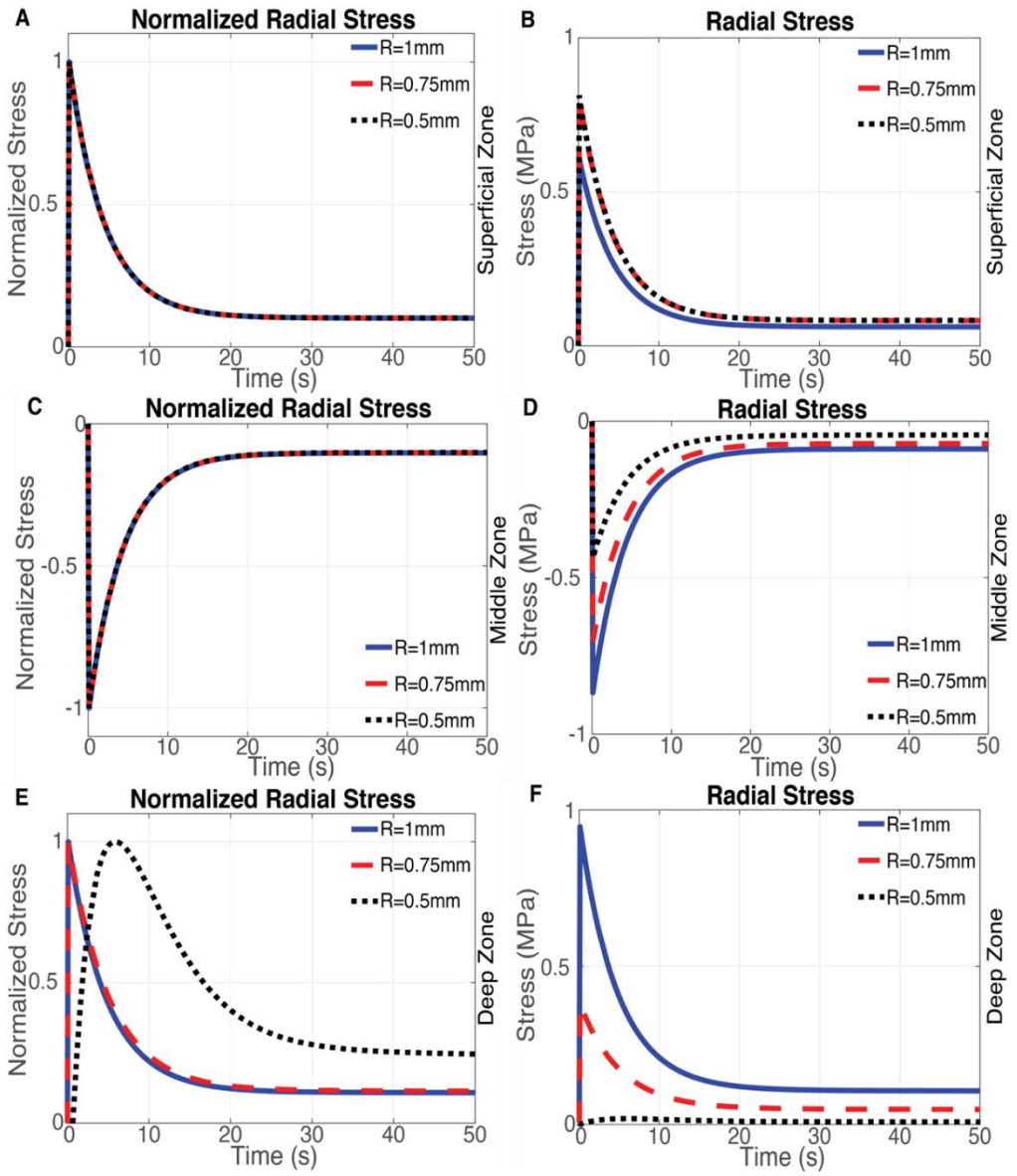

Figure 3.4 Radial stress as a function of time for three radii. Stress normalized to the peak radial stress at location of interest (left column) and absolute radial stress (right column) at the mid-depth of the superficial-zone(A-B), middle-zone (C-D), and deep-zone (E-F).

3.4.5 Effective Fluid Pressure Relaxation

Effective fluid pressure relaxation was observed throughout cartilage and bone following the initial loading of cartilage. Analysis of the radial edge revealed fluid pressure relaxation for each layer of cartilage (**Figure 3.5A-F**) and radial mesh size. In addition, analysis of the midline

and center of cartilage revealed similar patterns of fluid pressure relaxation. Likewise, analysis of bone at the radial edge and along the midline revealed fluid pressure relaxation throughout the bone. Additional analysis showed that pressure relaxation along the center of bone transitioned from negative to positive with depth from the cartilage-bone interface.

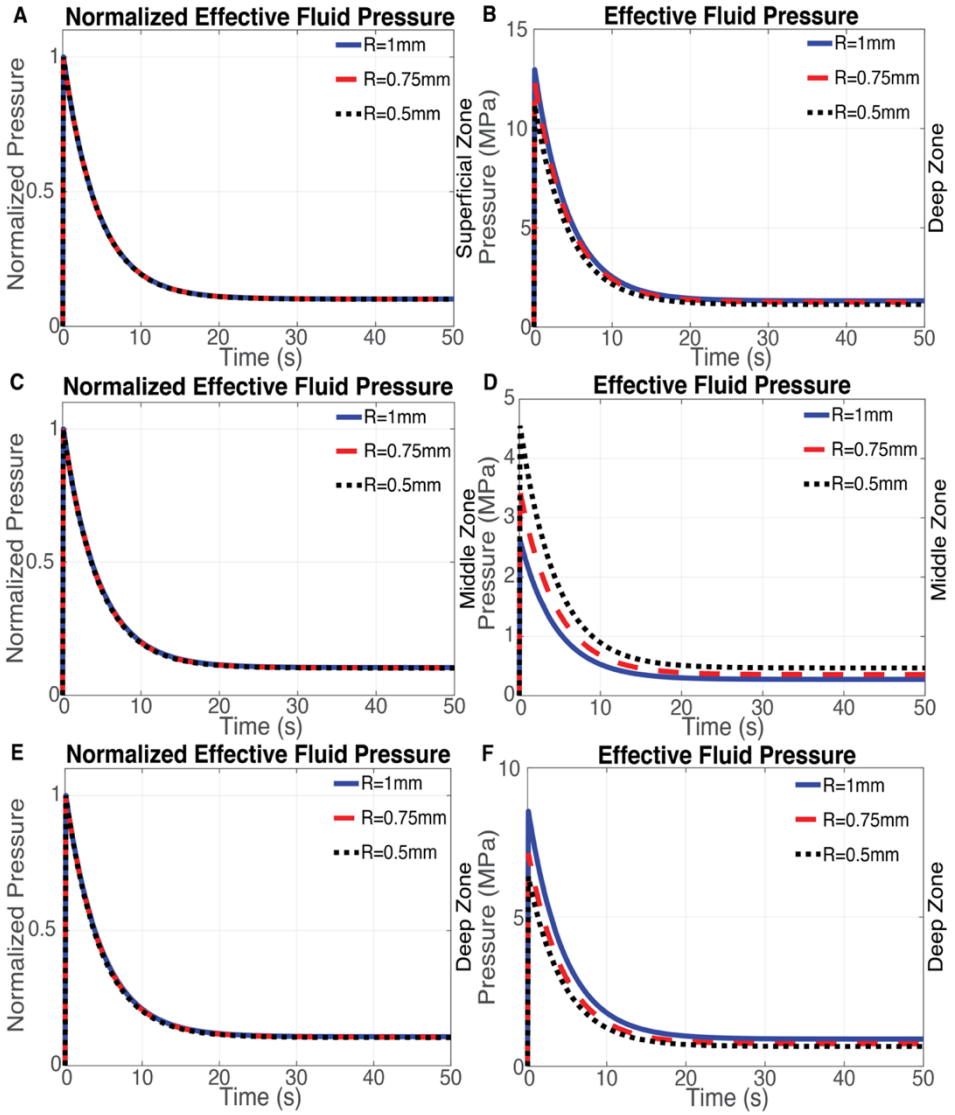

Figure 3.5 Effective fluid pressure in cartilage as a function of time for three radii. Fluid pressure normalized to peak effective fluid pressure (left column) and absolute effective fluid pressure (right column) at locations of interest at mid-depth of the superficial-zone (A-B), middle-zone (C-D), and deep-zone (E-F).

Fluid pressure relaxation profiles were found to be similar for each of the radial mesh sizes (1, 0.75, 0.5mm) studied, with R = 0.5 mm having the highest relative relaxation after 400s (Figure 5A). Additionally, consistent with the results seen for compressive stress, the effective fluid pressure has a direct relationship with decreases in radial mesh size.

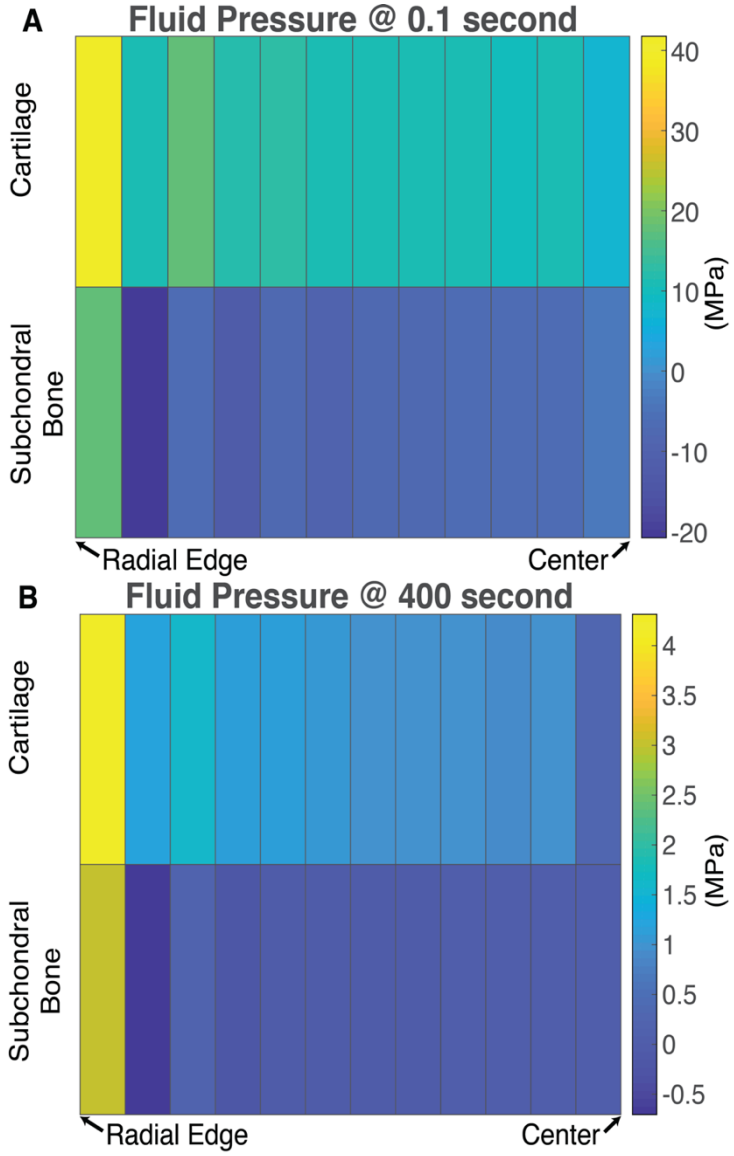

Figure 3.6 Mesh elements at the cartilage-bone interface A): Fluid pressures at cartilage-bone interface after initial load; B) Fluid pressure at cartilage-bone interface after 400 seconds of relaxation.

3.4.6 Fluid Pressure Gradients

Cartilage fluid pressures at the cartilage-bone interface were consistently higher than bone immediately following the initial loading period (t=0.1 second) (**Figure 3.6A**). We also found that fluid pressure gradients decreased after the 400 second relaxation period (t = 400 seconds) (**Figure 3.6B**).

3.5 Discussion

The purpose of this study was to investigate fluid pressure gradients and radial size effects in fluid transport across the cartilage-bone interface during unconfined compression experiments. Our model is capable of modeling the stress-relaxation response of cartilage in unconfined compressive stress relaxation. Further, the results from our model are consistent with analytical results for biphasic materials[88], including axial and radial stress relaxation, and effective fluid pressure relaxation. Results for the radial stresses in the superficial and middle zones of cartilage can be explained by the collagen fiber orientation in each region. Greater volume fraction of collagen fibers parallel to the cartilage surface (including many in the radial direction) in the superficial zone led to lower radial stresses (**Figure 3.4D**) as the sample radius increases. By contrast, the random distribution of fibers in the middle zone and increased modulus (3.5 MPa v. 2.5 MPa) leads to lower stress magnitudes and overall negative radial stresses.

Optimization of our model against experimental results showed its ability to simulate the stress relaxation of cartilage in unconfined compression. Our model captured both the peak and equilibrium loads. However, this model was not able to fully capture the dynamics of the relaxation response. It is unclear if this shortcoming results from limitations of the model,

limitations of the available optimization techniques within FEBio, or limitations of stress-relaxation from only the middle zone of cartilage. FEBio offers the Levenberg-Marquardt method with options for parameter constraints and linear temporal spacing. However, we were unable to weight the residuals in the objective function, and with linear temporal sampling this resulted in excellent fits to the equilibrium regions and lower quality fits to the dynamic relaxation portion [98]. Furthermore, we optimized our stress-relaxation response against middle zone cartilage, which may have impacted our ability to capture the full thickness response to stress-relaxation. Thus, in future studies, we will incorporate weighted optimization studies to better capture the relaxation dynamics, and we will consider experimental stress-relaxation responses for full thickness articular cartilage.

Modeling results at the cartilage-bone interface demonstrate that unconfined compression results in higher fluid pressures in the cartilage than bone. These results suggest that a fluid pressure gradient develops from cartilage to bone during loading (**Figure 3.6A**). Our results agree with Stender *et al*[64] in that fluid is transported between cartilage and bone and this transport is driven by the development of fluid pressure gradients at the cartilage-bone interface. Stender *et al*[64] presented models of both unconfined compression and spherical indentation in effort to understand the influence of permeability on cartilage-bone fluid transport. Our model is also in agreement with these previous results on the direction of the fluid transport during loading, although our model predicts much lower levels of transport (~500 fold decreased flux) from cartilage to bone. This discrepancy may result from our use of an ellipsoidal fiber distribution and the previous use of an anisotropic distribution of collagen fibers. Additionally, our use of a viscoelastic model versus the previous use of a poroelastic model may also be

important. Our model assumes that the matrix and fibers react in a time-dependent manner (viscoelastic) that is independent of the fluid movement, whereas the previous model assumes that the solid matrix and collagen fibers relax due to the movement of fluid inside the matrix (poroelastic). A limitation of both viscoelastic and poroelastic models is that neither fully describes cartilage time-dependent material properties. However, since our viscoelastic model and previous poroelastic models both produce the result of higher fluid pressure in cartilage than bone in loading, this fluid transport behavior appears robust to a range of assumptions about cartilage mechanics.

Our results challenge the conventional understanding that fluid transport predominantly occurs between cartilage and synovial fluid. Fluid transport from subchondral bone to cartilage (*i.e.*, during unloading) and within cartilage may impact the health and viability of chondrocytes. The transfer of nutrients and cytokines from subchondral bone could provide biochemical energy and chemical signals to chondrocytes. In this way, physiological loading could support chondrocyte health and viability by supplementing the nutrient transfer from synovial fluid. An additional interpretation of our results is that bone may act as an 'overflow reservoir' for fluid in cartilage. Previous studies indicate that chondrocyte metabolism is altered by fluid induced shear-stresses [99] and that certain levels of fluid induced shear stress is healthy for chondrocytes [12, 100]. Thus, fluid movement from cartilage to bone could also serve to mitigate possible cartilage tissue overload.

Fluid transfer between subchondral bone and cartilage could also participate in the cartilage degradation that follows joint injury. Recent studies demonstrate that the cartilage pericellular and extracellular matrices undergo significant alterations within three days after

injury [33, 101]. These changes may be caused, or exacerbated by, transport of cytokines and proteases from bone to cartilage. Changes to subchondral bone tissue after injury could affect fluid transport across the joint. Subchondral bone experiences a transient phase after joint injury of thinning and loss of bone mineral before becoming sclerotic [41, 102]. These changes to bone geometry and density would be expected to impact how fluid is transported between the two tissues. Increased or decreased transport could each affect cartilage loading and nutrition. The impacts of fluid transport from physiological loading between cartilage and bone on the health of these tissues, and the role of altered fluid transport on deleterious cartilage changes following joint injury necessitates new directions of investigation.

Our model advances several aspects of the understanding of fluid transport between bone and cartilage. Using an ellipsoidal fiber distribution, we improved the modeling of collagen fibers within the cartilage tissue. This improvement is critical to osteochondral fluid transport models as it provides a more accurate structural representation of the mechanics in cartilage that are directly tied to this transport. Our model also improves the understanding of the fluid velocity vectors and fluid flux at the cartilage-bone interface during physiological loading by incorporating a biphasic viscoelastic ellipsoidal fiber distribution model for cartilage. This new approach improves cartilage mechanics modeling and thus fluid transport modeling for osteochondral studies. Lastly, validation of our model to established biphasic solutions improves our confidence about the material stress states underpinning the fluid transport between these tissues. The implications of fluid transport between cartilage and bone on the health of these tissues, as well as in degenerative joint diseases, are not yet understood. Several critical questions remain about how fluid transport between subchondral bone and cartilage affects

chondrocyte health and viability, how transport between subchondral bone and cartilage following traumatic injury leads to increased inflammatory stimuli (*e.g.* TNFα) and how transport between subchondral bone and cartilage in healthy joints affect chondrocyte viability. These questions motivate new directions in investigating the role of fluid transport as a relevant factor in multi-tissue whole-joint health.

3.6 Acknowledgements

We thank Dr. David Pierce for key insight and critical discussion in developing the model. Funding support provided by NSF (CMMI 1554708) and NIH (R01AR073964). This chapter's contents contain the contents of a previously published paper [63].

CHAPTER FOUR

SUBCHONDRAL BONE STRUCTURE AND SYNOVIAL FLUID METABOLISM ARE ALTERED IN INJURED AND CONTRALATERAL LIMBS 7 DAYS AFTER NON-INVASIVE JOINT INJURY IN SKELETALLY-MATURE C57BL/6 MICE

Contribution of Authors and Co-Authors

Manuscript(s) in Chapter(s) 1

Contributions: Experimental design, data collection, data analysis and interpretation, manuscript drafting, revision of manuscript.

Co-Author: Connor Devine

Contributions: Experimental design, data collection, data analysis and interpretation.

Co-Author: Ronald K. June

Contributions: Revision of manuscript.

Co-Author: Chelsea M. Heveran

Contributions: Experimental design, data analysis and interpretation, manuscript drafting, revision of manuscript.

Manuscript Information

Brady David Hislop, Connor Devine, Ronald K. June, Chelsea M. Heveran

Osteoarthritis and Cartilage

Status of Manuscript:
☐ Prepared for submission to a peer-reviewed journal
☐ Officially submitted to a peer-reviewed journal
☐ Accepted by a peer-reviewed journal
☒ Published in a peer-reviewed journal

Elsevier
Volume 30, issue 12
https://doi.org/10.1016/j.joca.2022.09.002

Abstract

Post-traumatic osteoarthritis (PTOA) commonly develops after ACL injury, but early changes to the joint soon after injury are insufficiently understood. The objectives of this study were (1) evaluate the response of subchondral bone tissue modulus to joint injury and (2) identify which bone structural, material, and metabolic outcomes are local (i.e., injured joint only) or systemic (i.e., injured and contralateral-to-injured). Female C57Bl\6N mice (19 weeks at injury) underwent tibial compression overload to simulate ACL injury (n = 8) or a small pre-load (n = 8). Synovial fluid was harvested at euthanasia 7 days later for metabolomic profiling. Bone outcomes included epiphyseal and SCB microarchitecture, SCB nanoindentation modulus, SCB formation rate, and osteoclast number density. Injury decreased epiphyseal bone volume fraction ([-5.29, −1.38%], P = 0.0016) and decreased SCB thickness for injured vs sham-injured limbs ([2.2, 31.4 μm], P = 0.017)). Epiphyseal bone loss commonly occurred for contralateral-to-injured limbs. There was not sufficient evidence to conclude that SCB modulus changes with injury. Metabolomic analyses revealed dysregulated synovial fluid metabolism with joint injury but that many metabolic pathways are shared between injured and contralateral-to-injured limbs. This study demonstrates rapid changes to bone structure and synovial fluid metabolism after injury with the potential for influencing the progression to PTOA. These changes are often evidenced in the contralateral-to-injured limb, indicating that systemic musculoskeletal responses to joint injury should not be overlooked.

4.2 Introduction

Post-traumatic osteoarthritis (PTOA) affects 5.6 million people in the US each year [58]. Patients who suffer ACL tears develop PTOA at an alarming rate. Regardless of ACL reconstruction status, 50% of patients will develop PTOA within 20 years of joint injury[103]. Early interventions that mitigate the first deleterious changes to joint tissues may relieve some of the immense physical and financial burdens of PTOA[40, 104, 105]. However, to design and implement early interventions, additional data are needed to improve the understanding of how the loading and biological environments of the injured knee change early after joint injury.

It is well-established that subchondral and epiphyseal bone undergo transient thinning after joint injury that later reverses and progresses towards sclerosis [34, 44, 66, 106] (**Table 4.1**). The rapid decline of subchondral bone and epiphyseal microarchitecture may directly impact the bone mechanical environment. If subchondral and epiphyseal bone microarchitecture decreases, μstrain will increase in subchondral bone with potential impacts to bone mechanotransduction[107, 108]. The changes would be expected to be further exacerbated by changes to tissue-scale subchondral bone modulus, since the stiffness of bone tissue influences the strain experienced by osteocytes, a bone cell type recently implicated in the development of PTOA[109, 110]. Subchondral bone modulus decreases for rodents when osteoarthritis is established and the subchondral bone plate is sclerotic[35, 111]. However, it is unknown whether subchondral bone modulus changes coincide with subchondral bone plate thinning. Thus, it is critical to quantify subchondral bone modulus changes after joint injury to better understand the effects of early bone changes on the bone tissue mechanics and mechanotransduction.

Table 4.1 Literature review of early bone responses to ACL injury in rodent models

Study	Animal sex, strain, and species	Animal age (weeks)	Injury model	Evaluation timepoints (days after injury)	Regions of interest	Early acute epiphysial bone response to injury (7-10d)
Christiansen et al., Osteoarthritis and Cartilage, (2012), 773-782, 20(7)[8]	Male C57BL/6N mice	10	Non-invasive ACL rupture via tibial compression overload	1, 3, 7, 14, 28, 56	Distal femoral epiphysis, proximal tibial epiphysis	*Distal femoral epiphysis* 7d (injured vs contralateral limb): 44% ↓BV/TV 25% ↓Apparent BMD 24% ↓ Tb.Th *Proximal tibial epiphysis* 7d (injured vs contralateral limb): 40% ↓ BV/TV 20% ↓ Apparent BMD 15% ↓ Tb.Th
Anderson et al., Journal of Orthopaedic Research, (2016)[6]	Female C57BL/6N mice	10	Non-invasive ACL rupture via tibial compression overload	7, 14	Distal femoral epiphysis	7d (injured vs sham-injured limb): 25% ↓BV/TV 20% ↓ Tb.Th
Khorasani et al., Arthritis Research and Therapy, (2015), 17(1)[9]	Female C57BL/6N mice	10	Non-invasive ACL rupture via tibial compression overload	7, 14, 56	Distal femoral epiphysis	7d (injured vs sham-injured limb): 27% ↓ BV/TV 18% ↓Tb.Th

Table 4.1 Continued

Study	Animal sex, strain, and species	Animal age (weeks)	Injury model	Evaluation timepoints (days after injury)	Regions of interest	Early acute epiphysial bone response to injury (7-10d)
Lockwood et al., Journal of Orthopaedic Research, (2014), 79-88, 32(1)[7]	Male C57BL/6N mice	11	Non-invasive ACL rupture via tibial compression overload	10, 84, 112	Distal femoral epiphysis	*High strain rate (500mm/s)* 10d (injured vs sham-injured limb): 20% ↓ BV/TV *Low strain rate (1mm/s)* 10d (injured vs sham-injured limb): 31% ↓ BV/TV
Wegner et al., *Journal of Orthopaedic Research, (2019), 2429-2436, 37(11)*[10]	Female C57BL/6N mice	10	Non-invasive ACL rupture via tibial compression overload	7	Distal femoral epiphysis	7d (injured vs. contralateral limb): ~18% ↓ BV/TV
Hahn et al., Osteoarthritis and Cartilage, (2021), 882-893, 29(6)[25]	Male, Female C57BL/6 mice	20	Non-invasive ACL rupture via tibial compression overload	7	Distal femoral epiphysis	7d (injured vs. contralateral limb): 5.9 % ↓ Tb.Th 7% ↑ BS/BV

Table 4.1 Continued

Study	Animal sex, strain, and species	Animal age (weeks)	Injury model	Evaluation timepoints (days after injury)	Regions of interest	Early acute epiphysial bone response to injury (7-10d)
Maerz et al., *Journal of Orthopaedic Research, (2021), 1965-1976, 39(9)*[27]	Female Lewis rat	14	Non-invasive ACL rupture via tibial compression overload	3, 7, 10, 14	Distal femoral epiphysis	*Medial condyle* 7d (injured vs. ipsilateral sham-injured limb) ~3% ↓ BV/TV 7d (injured vs contralateral limb) ~3% ↓ SCB.Th *Lateral condyle* 3d (injured vs contralateral limb) ~2% ↑ BV/TV ~2% ↑ SCB TMB 7d (injured vs contralateral limb) ~2% ↑ BV/TV
White, Brancati, and Lepley, Journal of Orthopaedic Research, (2022), 74-86, 40(1)[17]	Male, Female Long-Evans Rat	16	Destabilized medial meniscectomy	7, 14, 28, 56	Distal femoral epiphysis	*Medial condyle* 7d (injured vs. uninjured control rats): *Male*: ~ 167% ↑ SCB.Pl.Po *Female*: ~ 90% ↑ Sb.Pl.Po *Lateral condyle* 7d (injured vs. uninjured control rats): *Male*: ~ 263% ↑ Sb.Pl.Po *Female*: ~154% ↑ Sb.Pl.Po

Table 4.1 Continued

Study	Animal sex, strain, and species	Animal age (weeks)	Injury model	Evaluation timepoints (days after injury)	Regions of interest	Early acute epiphysial bone response to injury (7-10d)
McCulloch et al., Osteoarthritis and Cartilage, (2019), 1800-1810, 27(12)[23]	Male C57BL/6 mice	10	Destabilized medial meniscectomy	7, 14, 28	Proximal tibial epiphysis	7d (injured vs contralateral limb): ~48% ↑ BV/TV
Das Neves Borges, Vincent, and Marenzana, PLoS ONE, (2017), 12(3)[22]	Male C57BL/6 mice	10	Destabilized medial meniscectomy	7, 14, 28, 56, 84, 140	Proximal tibial epiphysis	*Medial condyle* 7d (injured vs contralateral limb): ~3% ↑ BV/TV

The impacts of joint injury may extend to the contralateral-to-injured limb. Patients who undergo an initial knee replacement have a 37.2% chance of needing a contralateral limb replacement within 10 years [111]. Christiansen and coauthors found decreased trabecular bone volume fraction in the contralateral epiphysis 7d after non-invasive joint injury in mice[34]. In another study, the same authors found decreased trabecular microarchitecture in the L5 vertebra 10 days after joint injury[35]. Contralateral bone loss may be the consequence of altered loading[112], a systemic inflammatory response[67, 113], or altered remodeling bone cell populations [110, 114, 115]. However, rodent models of PTOA commonly only compare early outcomes after joint injury between injured and contralateral-to-injured limbs and not to a sham-injured control [34, 45, 46, 66]. Comparisons between injured and sham-injured limbs are usually limited to later time points when bone is sclerotic and PTOA is established [34, 45, 46]. Important gaps remain in our understanding of early bone changes in the injured and contralateral-to-injured limbs.

Synovial fluid interacts with multiple joint tissues including bone and cartilage. Therefore, shifts in synovial fluid metabolism marked by changes in metabolites (i.e., small molecules chemically changed in metabolism) could point to specific biological changes that rapidly occur after ACL injury These potential biomarkers would likely be useful for designing early interventions to mitigate the progression to PTOA. Furthermore, synovial fluid, unlike other joint tissues, can potentially be assessed through needle biopsy in a clinical setting[116]. Recent studies find distinct metabolic profiles between injured and sham-injured synovial fluid 7d after joint injury in mouse models[37, 117]. However, what shifts in synovial fluid metabolism occur locally (i.e., injured joint) or also systemically (i.e., also present in

contralateral joint) soon after injury remain unknown. Furthermore, since synovial fluid interfaces with bone, which is much more metabolically active than cartilage [23], it is of key interest to understand whether shifts in synovial fluid metabolism occur at the same time as early changes to bone structure and material properties.

In this study, we fill several significant critical gaps about the early biological and structural response of the joint 7 days after ACL injury. First, we test whether subchondral bone tissue material properties change in the same time frame as bone thinning. Next, we evaluate shifts in synovial fluid metabolism as an indication of changes to cellular bioenergetics of the joint. All structural, material, and biological outcomes are compared between injured, contralateral-to-injured, and sham-injured joints, allowing estimation of local (i.e., injured joint only) and systemic (i.e., injured and contralateral-to-injured) effects.

4.3 Materials and Methods

4.3.1 Mouse Model of Joint Injury

All animal procedures were approved by the Montana State University Institutional Animal Care and Use Committee. C57Bl\6N mice were acquired from Charles River laboratories. Mice were allowed to acclimate for two weeks prior to injury (19-weeks old at injury). Each mouse was assigned to either the injury (overload-induced ACL tear) or control (sham-injury) groups. The injured or sham-injured joint was randomly assigned to a side using the sample function in R.

On the day of injury, mice were anesthetized in an inhalation chamber (2-4% isoflurane, ~30 seconds) and then nose cone (2% isoflurane) while one limb was loaded into a custom-built loading machine (**Figure 4.1A-B**). Sham-injured and injured limbs were subjected to a pre-load

(1-2N, 0.5mm/s). Injured limbs were loaded to 12-15N at 130 mm/s, consistent with prior studies (**Figure 4.1C**)[7,8,28].

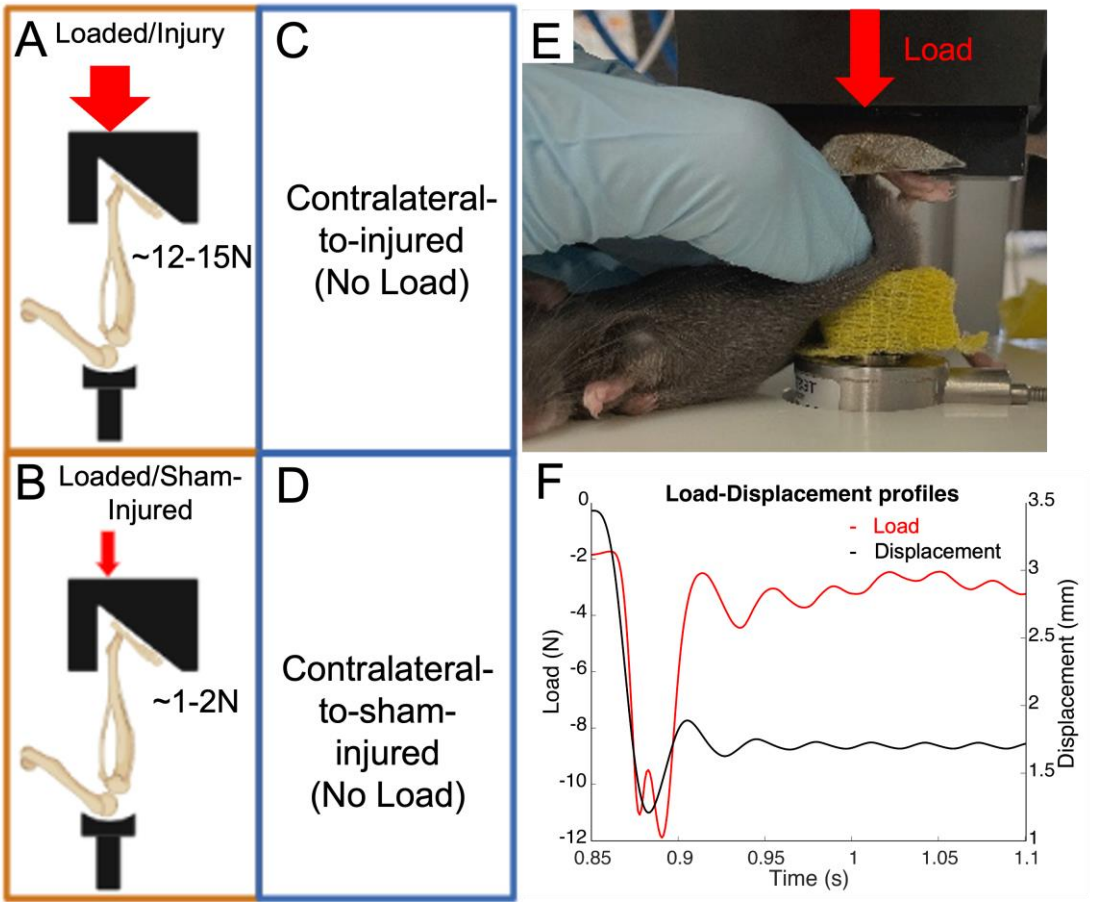

Figure 4.1. Mouse PTOA model. A, B) Schematic of mouse hind limb in loading machine with load applied parallel to tibia. C, D) The contralateral limbs of both injured and control mice were not loaded. E) Mouse loaded into loading machine during study. F) Load-displacement curves showing a change in displacement coinciding with a sinusoidal load response between 0.875- and 0.9-seconds characteristic of an anterior translation of the tibia leading to ACL rupture[23, 34]. Figures 1A and B created with Biorender.com.

ACL tears were confirmed *in vivo* by a characteristic release in compressive load and by performing pre- and post-injury joint laxity tests of anterior stability[34, 118, 119]. Five mice were excluded for failed ACL tears and two for tibial fractures. After exclusion of these 7 mice, 8 mice were studied per treatment group (injured, sham-injured). Sixteen mice (n=8 injured, n=8

sham-injured) were studied for subchondral bone response and synovial fluid responses to joint injury.

Mice were group housed (≤5 mice per cage) and provided rodent diet (Purina LabDiet 5053) and water *ad libitum*. Calcein (20 mg/kg) and alizarin (30 mg/kg) fluorochrome labels were administered intraperitoneally 2-3 days before injury and 6 days post-injury, respectively. Mice were euthanized 7 days post-injury *via* cervical dislocation.

4.3.2 Microarchitecture of the Proximal Tibia Epiphysis and Subchondral Bone

Tibiae were cleaned of non-osseous tissue, submerged in 70% ethanol, and refrigerated (4°C). Proximal tibiae were evaluated for microarchitecture of the epiphysis and subchondral bone thickness and tissue mineral density in the medial and lateral compartments (μCT40, Scanco Medical AG, 10 μm isotropic voxel size, 70 kVP, 114 μA, 200 ms integration time). The scanned volume was a 1 mm (100 coronal slices) thick region at the center of the proximal tibial epiphysis. The first region of interest included the epiphysis (Figure 2C). Analyses included bone volume (BV, mm^3), total volume (TV, mm^3), bone volume fraction (BV/TV, %), bone mineral density (BMD, $mgHA/cm^3$), trabecular number (Tb.N, 1/mm), trabecular spacing (Tb.Sp, mm), and trabecular thickness (Tb.Th, mm)[120]. Subchondral bone plate thickness and TMD were analyzed for consistent locations in the medial and lateral compartments (Scb.Th, mm; Scb.TMD, $mgHA/cm^3$) (**Figure 4.2C**).

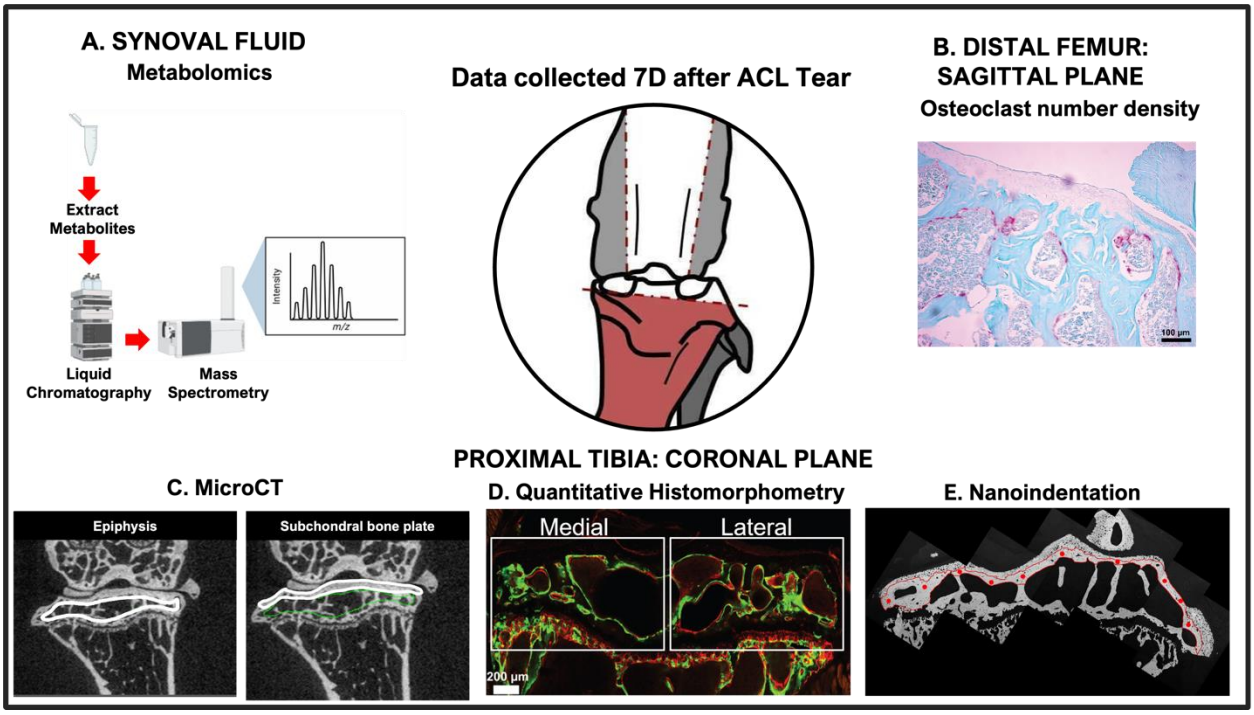

Figure 4.2. Schematic of experimental methods to characterize bone and synovial fluid responses to joint injury. A) Schematic of synovial fluid metabolomic extraction and analysis procedure from extraction to mass spectra. B) Osteoclast activity at the distal femur was evaluated from TRAP-stained sections. C) Microarchitecture of the epiphysis and subchondral bone were evaluated using microCT. D) Dynamic bone remodeling for the epiphysis was measured from confocal laser scanning microscopy images from polished coronal sections. Medial and lateral regions of interest are delineated by the white boxes. E) Subchondral bone modulus was measured using nanoindentation on polished coronal sections. Indents were placed within the outlined region spanning the medial to lateral aspects of the subchondral bone plate. Figure 2A Created with Biorender.com

4.3.3 Osteoclastic Bone Resorption at the Femoral Epiphysis

Femurs were placed in 10% neutral buffered formalin for 18 hours, decalcified in Ethylene Diamine Tetraacetic Acid (EDTA), dehydrated in a graded series of ethanol concentrations (70-100%), embedded in paraffin, and microtomed to 6µm-thick sagittal sections. Sections were stained via standard protocols for tartrate resistant acid phosphatase (TRAP) and imaged using a brightfield microscope (Nikon, Eclipse E-800) (**Figure 4.2B**). Using ImageJ[121], an evaluator blinded to joint injury status traced the epiphysial trabecular bone

surfaces enclosing the marrow cavities (4X images) and counted the multinucleated, TRAP-positive cells (*i.e.,* dark pink) (10X images). We report the osteoclast number density normalized per marrow area and bone surface.

4.3.4 Dynamic Bone Remodeling of the Proximal Tibia Epiphysis

Following microCT, tibiae were embedded in poly(methyl)methacrylate, sectioned along the coronal plane of the tibial plateau, and polished to a mirror finish as previously described (**Figure 4.2**) [122]. Calcein and alizarin labels were imaged at the proximal tibia using confocal laser scanning microscopy (CLSM, inverted Leica SP5). Samples were excited at 488 nm and 561 nm. Emission windows were 500 nm-550 nm (calcein) and 650 nm-750 nm (alizarin). The voxel size was 1.52µm x 1.52µm x 4.74µm. Z-stacks were collected for each sample in medial and lateral regions and one in-focus slice from each image stack was analyzed (Imaris 9.3.0, Bitplane).

Bone perimeter and calcein and alizarin labels were traced on iPads by two independent evaluators blinded to injury status. If inter-evaluator agreement was less than 95%, sections were re-analyzed by both evaluators. Bone perimeter and labels were measured in epiphyseal regions of interest (**Figure 4.2D**). For each region of interest, bone surface, alizarin surface / bone surface, and calcein surface / bone surface were calculated. These measures were calculated using a custom written MATLAB script (available at: https://github.com/hisl6802/Quantitative-Histomorphometry-Automated-Tracing-).

4.3.5 Tissue-Scale Subchondral Bone Plate Modulus of the Proximal Tibia

Nanoindentation was performed on subchondral bone from polished proximal tibia sections

using a KLA Tencor iMicro (5 mN max load, 30s load and unload, 60s hold) and diamond Berkovich tip (ν_t=0.07, E_t=1140 GPa). Indents were placed between the tidemark and the epiphysis spanning the medial to lateral subchondral bone plate (n=8 per sample) (**Figure 4.2E**). Indentation curves were analyzed for reduced modulus (E_r) consistent with description by Vahidi et al[122] (**Figure B1**). We report the indentation modulus E_i, which is corrected for the diamond tip properties, but avoids assuming a Poisson's ratio for the tissue sample ($\boldsymbol{\nu}_s$) (**Equations 1-2**)[123].

$$\frac{(\mathbf{1}-\boldsymbol{\nu}_s^2)}{\boldsymbol{E_s}} = \left(\frac{\mathbf{1}}{\boldsymbol{E_r}} - \frac{(\mathbf{1}-\boldsymbol{\nu}_t^2)}{\boldsymbol{E_t}}\right) \quad (1)$$

$$E_i = \frac{E_s}{(1-\nu_s^2)} \quad (2)$$

Indents were excluded for poor surface contact, a non-smooth loading or unloading curve, or moduli indistinguishable from PMMA (≤5 GPa).

4.3.6 Profiling the Metabolic Response of Joints to Traumatic Injury

Synovial fluid was extracted from the stifle joint immediately following euthanization consistent with our previous publication[117]. Briefly, an incision was made anteriorly into the synovium and synovial fluid was collected by adsorption using Melgisorb alginate dressing (Tendra). Metabolites were extracted as previously described[31, 65] and analyzed using Liquid Chromatography-Mass Spectrometry (LC-MS, Agilent 1290 UPLC, Agilent 6538 Q-TOF mass spectrometer) (**Figure 4.2A**). Spectra were submitted to XCMS[124] for peak identification.

4.3.7 Data Analysis

4.3.7.1 Bone Outcomes. Bone measures were analyzed using mixed model ANOVA. Fixed effects included injury (injury vs. sham-injury) and load side (loaded and sham-loaded vs. contralateral). The individual mouse was a random effect. Each model included an interaction term between load side and injury. For nanoindentation modulus, which included multiple indents per sample, the relative distance from the medial edge was included as a covariate. For fluorochrome labels and subchondral bone, location (i.e., medial or lateral) was a fixed effect and limb was a random effect nested within the individual mouse.

Dependent variable transformations were performed, if necessary, to satisfy ANOVA assumptions of residual normality and homoscedasticity. Critical alpha was set *a priori* at 0.05. Significant interactions were followed by post-hoc tests for simple effects while maintaining family-wise error at 0.05 using a Bonferroni correction. Spearman rank correlation analysis was performed to evaluate relationships between bone outcomes and peak load.

4.3.7.2 Metabolomic Analysis ANOVA (analysis of variance), t-tests, principal component analysis (PCA), partial least squares-discriminant analysis (PLS-DA), and hierarchical clustering were used to compare metabolic profiles for synovial fluid from the injured, sham-injured, and contralateral-to-injured limbs. The metabolic data were then subjected to cluster validation and ensemble clustering to determine the metabolites which consistently clustered together (**Appendix B**) (**Figure 4.3**). The 10 largest clusters identified through ensemble clustering were submitted to mummichog to identify the associated metabolic pathways [71].

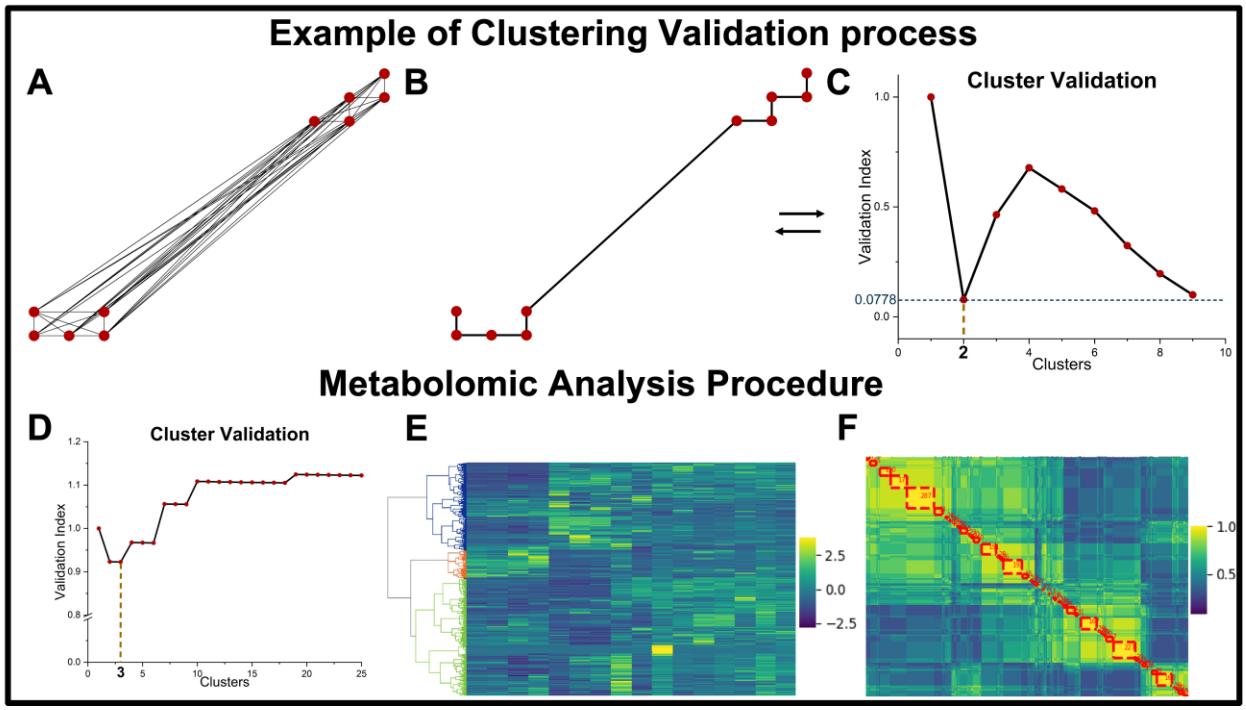

Figure 4.3. Example of minimum spanning tree (MST) based cluster validation. Metabolomic clustering analysis procedure. A) Ten 2D points (randomly generated using MATLAB) connected in a full dissimilarity tree. B) MST for these ten points. C) Cluster validation for B showing that 2 clusters (0.0778 validation index) is the optimum choice. D) Cluster validation output for analysis of sham-injured & injured limb metabolic profiles showing a local minimum at 3 clusters. E) Graphical representation of one of thirteen hierarchical clustering outputs of the sham-injured & injured metabolomic data, with the three clusters of interest colored (blue, orange, and green). F) Ensemble clustering output showing the clusters with greater than 40 metabolites in red dashed squares (yellow represents metabolites which clustered together in each of the thirteen clustering solutions).

4.4 Results

4.4.1 Epiphyseal and Subchondral Bone Plate Microarchitecture of the Proximal Tibia Declines

MicroCT of the tibial epiphysis revealed significant effects of injury (i.e., injury vs. sham-injury) and loaded side (i.e., the injured and sham-injured limb vs. the contralateral limbs) on several measures of bone microarchitecture. Epiphyseal BV/TV decreased with injury (relative change -10.8%, p=0.002, 95% CI [-4.66, -1.21%]). BV/TV was also lower for loaded

vs. unloaded sides (-7.5%, p=0.023, [-3.74, -0.29%]) (**Figure 4.4A**). Epiphyseal BMD also decreased with injury (-7.1%, p=0.012, [-42.83, -5.67 mgHA/cm^3]) and for loaded sides (-5.8%, p=0.040, [-38.08, -0.92 mgHA/cm^3]). Similarly, epiphyseal Tb.Th decreased with injury (-5.5%, p=0.028, [-7.4e-3, -4.5e-4 mm]) and for loaded sides (-6.0%, p=0.017, [-7.8e-3, -8.3e-4 mm)). For each of these measures, there were no significant interactions between injury and loaded side. Tb.N and Tb.Sp were not affected by injury, loaded side, or their interaction. Because the peak load to cause the joint injury varied between mice, we tested whether peak load influenced measures of bone microarchitecture. Spearman's rank correlation analysis of peak load vs. BV/TV, BMD or Tb.Th found no significant relationships ($p>0.05$ for all) (95% CI for ρ: [-0.83,0.537], [-0.894,0.386], [-0.84,0.519], respectively).

Subchondral bone plate thickness (Scb.Th) showed an interactive effect of injury and loaded side (p = 0.039) (**Figure 4.4B**). Post-hoc testing revealed significantly decreased Scb.Th for injured compared with sham-injured limbs (-12.3%, p = 0.017, [-31.4, -2.2 μm]). There may be a reduction in Scb.Th for injured compared with contralateral-to-injured limbs, but we were underpowered to detect this difference (p=0.054). The Scb.Th was not different for sham-injured and contralateral-to-sham injured limbs. The subchondral bone plate thickness was on average 18 μm thicker for the medial compartment (14.5%, $p<0.01$, [11.9, 24.2 μm]). Subchondral bone tissue mineral density (SCB.TMD) also showed an interactive effect of injury and loaded side ($p<0.01$). From post-hoc tests, injured limbs had lower SCB.TMD than sham-injured (-2.3%, p = 0.021, [-66.8, -3.90 mgHA/cm^3]) and contralateral-to-injured limbs (-4.1%, p = 0.015, [-74.7, -6.68 mgHA/cm^3]). The SCB.TMD was not different for sham-injured and contralateral-to-sham

injured limbs or between medial and lateral compartments. SCB.Th and SCB.TMD were not related to peak load ($p>0.05$, ρ: [-0.91,0.22]; $p > 0.05$, ρ: [-0.88,0.34]; respectively) (**Table 4.2**).

Table 4.2 Subchondral Bone Microarchitecture. Data represent the marginal mean ± standard deviation of each measure.

Measure	**Control**		**Injured**	
	Contralateral-to-sham n = 8	**Sham-Loaded** n = 8	**Contralateral-to-injured** n = 8	**Loaded to injury** n = 8
Proximal tibia epiphysis				
Bone Volume Fraction (%) **Injury**: p = 0.002 **Loaded side**: p = 0.023 Injury x loaded side: NS	27.57±2.16	26.51±2.28	25.60±2.91	22.63±2.09
Bone Mineral Density (mgHA/cm^3) **Injury**: p = 0.012 **Loaded side**: p = 0.040 Injury x loaded side: NS	345.50±21.26	337.25±24.76	332.50±29.57	301.75±26.31
Trabecular Number (1/mm) Injury: NS Loaded side: NS Injury x loaded side: NS	4.05±0.28	3.97±0.33	3.99±0.26	3.97±0.13
Trabecular Thickness (mm) **Injury**: p=0.028 **Loaded side**: p = 0.017 Injury x loaded side: NS	0.073±3.9e-3	0.071±5.1e-3	0.071±4.6e-3	0.065±5.5e-3
Trabecular Spacing (mm) Injury: NS Loaded side: NS Injury x loaded side: NS	0.261±0.016	0.263±0.032	0.264±0.023	0.261±0.01

Table 4.2 Continued

Measure	**Control**		**Injured**	
	Contralateral-to-sham n = 8	**Sham-Loaded** n = 8	**Contralateral-to-injured** n = 8	**Loaded to injury** n = 8
Proximal tibia epiphysis and subchondral bone				
Total Volume (mm^3) **Mouse**: p = 0.024 Injury: NS Loaded side: NS Injury x loaded side: NS	1.62±0.07	1.61±0.05	1.65±0.05	1.65±0.04
Bone Volume (mm^3) Injury: NS Loaded side: NS Injury x loaded side: NS	0.93±0.05	0.91±0.03	0.91±0.07	0.86±0.06
Bone Volume Fraction (%) **Injury**: p = 0.0016 **Loaded side**: p = 0.0296 Injury x loaded side: NS	57.67±2.76	56.44±1.75	55.29±2.76	52.15±3.28
Tissue Mineral Density ($mgHA/cm^3$) **Loading x Injury**: p = 0.0415	965.75±20.17	970.63±10.99	979.88±18.49	957.88±19.90
Bone Mineral Density ($mgHA/cm^3$) **Injury**: p = 0.012 **Loaded side**: p = 0.037 Injury x loaded side: NS	587.50±27.88	579.63±15.76	574.63±30.00	538.63±36.00

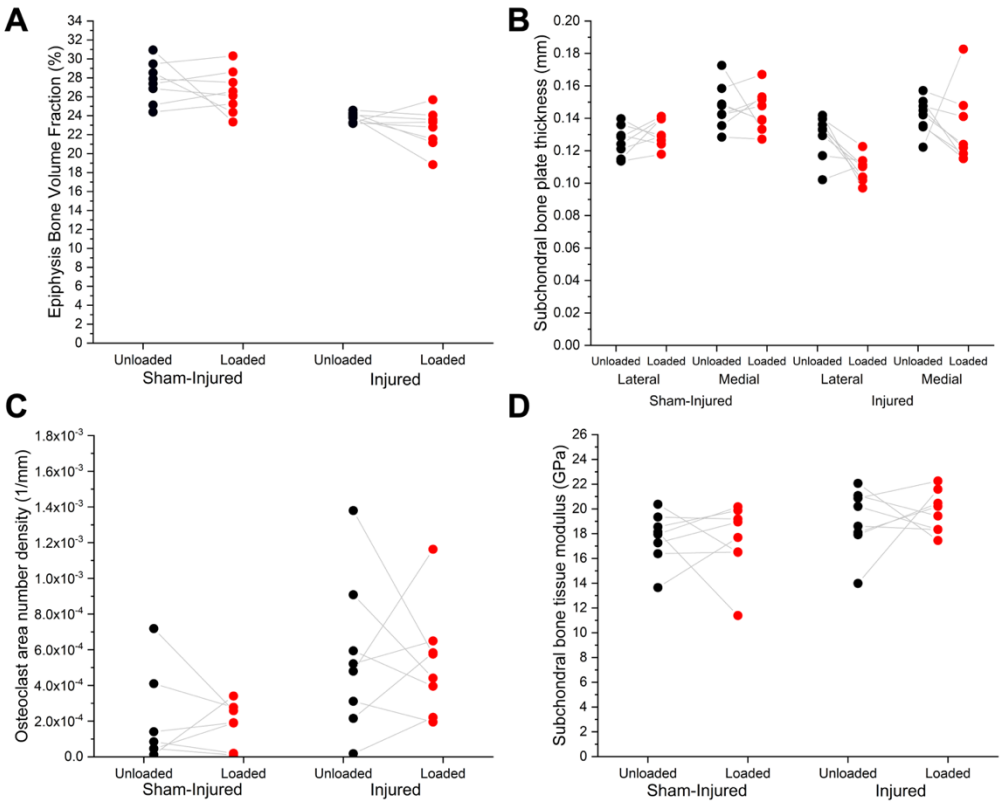

Figure 4.4. Key subchondral bone outcomes for loaded versus contralateral limbs for injured and sham-injured mice, including A) epiphyseal bone volume fraction, B) mean subchondral bone thickness, C) osteoclast number density per area, and D) subchondral bone tissue modulus.

4.4.2 Osteoclastic Resorption at the Distal Femoral Epiphysis Increases but Proximal Epiphysis Bone Formation is Unchanged

Injury increased osteoclast area number density on average by 3.87 times, and osteoclast number per bone surface at the distal femur epiphysis on average by 3.68 times (+287.2%, p=0.017, [2.7e-4, 2.33e-3 1/mm^2]; +267.4%, p=0.016, [7.6e-3, 5.8e-2 1/mm], respectively) (**Figure 4.4C**, **Table 3**). These measures were not impacted by loaded side nor the interaction between loaded side and injury. Thus, there was a similar increase in osteoclast abundance for both injured and contralateral-to-injured limbs. TRAP data were natural-log transformed for ANOVA analyses and back transformed for interpretation.

Table 4.3 Subchondral bone modulus, bone formation, and osteoclast number density. Data represent the marginal mean ± standard deviation of each measure. Mouse numbers per group vary per measure: indentation modulus (injured n = 8, control n = 8); calcein-to-bone-surface and alizarin-to-bone-surface (injured n = 7, control n = 8); osteoclast measurements (injured n = 8, control n = 7).

Measure	**Control**		**Injured**	
	Contralateral-to-sham	**Sham-Loaded**	**Contralateral-to-injured**	**Loaded to injury**
Proximal tibia epiphysis				
Indentation Modulus (GPa) Injury: p = 0.052 Loaded side: NS Injury x loaded side: NS	18.33±1.36	16.90±3.05	19.47±1.41	19.39±2.76
Calcein to Bone Surface (%) **Mouse**: p = 0.013 Injury: NS **Loaded side**: p = 0.005 Injury x loaded side: NS Injury x location: NS Location x loaded side: NS	46.10±16.35	34.54±17.01	40.85±13.00	36.50±9.08
Alizarin to Bone Surface (%) **Limb (Mouse)**: p = 0.001 Injury: NS Loaded side: NS Injury x loaded side: NS Injury x location: NS Location x loaded side: NS	42.28±18.84	33.44±19.82	37.63±12.66	46.30±23.26

Table 4.3 Continued

Measure	**Control**		**Injured**	
	Contralateral-to-sham	**Sham-Loaded**	**Contralateral-to-injured**	**Loaded to injury**
Distal femur				
Osteoclast number per bone marrow area (1/mm^2) **Injury**: p = 0.017 Loaded side: NS Injury x loaded side: NS	2.08e-4±2.62e-4	1.84e-4±1.27e-4	5.53e-4±4.27e-4	5.28e-4±3.05e-4
Osteoclast number per bone surface (1/mm) **Injury**: p = 0.016 Loaded side: NS Injury x loaded side: NS	5.32e-3±5.64e-3	4.26e-3±2.75e-3	1.37e-2±1.06e-2	1.45e-2±7.77e-3

Loaded side affected the proximal tibia epiphysis calcein-to-bone-surface (-18.3%, p=0.005, [-13.07, -2.84%]). Since calcein was administered 2-3 before injury, results indicate that bone resorption was increased for loaded (injured and sham-injured) limbs. Calcein labeling was not affected by injury, location (medial vs. lateral), or the interaction of these factors. Alizarin-to-bone-surface was not affected by injury, loaded side, region of interest, or the interaction of these factors. Bone formation surface was not impacted by the joint injury, since alizarin was administered 6 days after the joint injury and 1 day before euthanasia.

4.4.3 Tissue-scale Subchondral Bone Plate Modulus is not Changed

Nanoindentation tested whether subchondral bone plate modulus changes soon after joint injury. We first evaluated whether indent position (i.e., relative distance from the medial edge) influenced the indentation modulus (E_i). Since a covariate describing location within the subchondral bone plate was not significant (p=0.057), we used mixed model ANOVA without the covariate to test whether injury and loaded side effect E_i. Neither injury (p=0.052, [-0.02, 3.64 GPa]), loaded side (p=0.338, [-1.45, 1.94 GPa]), nor their interaction affected Ei (**Figure 4.4D**, **Table 4.3**).

4.4.4 Distinct Metabolic Changes are Evident in Synovial Fluid from Injured Limbs

We compared synovial fluid metabolic profiles from injured, sham-injured, and contralateral-to-injured limbs. 3402 metabolites were detected across all synovial fluid samples. Five metabolites were considered undetected and removed (zero median intensities).

4.4.4.1 Comparison of Injured, Sham-Injured and Contralateral-to-Injured reveals Dysregulated Metabolites. One-way ANOVA detected significantly dysregulated metabolites. PCA, PLS-DA and hierarchical clustering detected only minimal group differences. However, due to the subjectivity of hierarchical clustering[37] and the need to understand which metabolic pathways are shared between limbs (i.e., injured & sham-injured, injured & contralateral-to-injured, injured & contralateral-to-injured & sham-injured), further analysis was needed. Therefore, we employed *ensemble clustering*[72] to remove the subjectivity from metabolite clustering. Before cluster analyses, the median intensity of each metabolite in each group was determined. Clustering validation on 3397 metabolites found that 9 clusters were optimum. Ensemble clustering combined with the mummichog algorithm found primary bile acid biosynthesis, purine metabolism, porphyrin metabolism, arachidonic acid metabolism, steroid hormone biosynthesis, fatty acid elongation and degradation, glycosphingolipid biosynthesis, glycosaminoglycan degradation, alanine, aspartate and glutamate metabolism, and N-glycan biosynthesis (**Figure 4.5A**). Heatmap analyses showed distinct differences in median intensities between the sham-injured and both injured and contralateral-to-injured groups (**Figure 4.5B**).

Figure 4.5. Ensemble clustering pathway analysis results and heatmap showing the identification of potential dysregulated metabolites A) Venn diagram of key synovial fluid metabolic pathways between injured, sham-injured, and contralateral-to-injured limbs. Bolded pathways indicated pathways specific to a systemic response. B) Heatmap analysis of metabolite clusters identified by ensemble clustering of injured, contralateral-to-injured, and sham-injured synovial fluid.

4.4.4.2 Injured and Sham-Injured Synovial Fluid have Distinct Metabolic Profiles.

Because significant features were detected from ensemble clustering analyses and heatmap analysis confirmed differences in median metabolite intensities between injured, sham-injured,

and contralateral-to-injured groups, we compared specific metabolites within these groups. Univariate analysis of injured vs. sham-injured synovial fluid revealed 148 significant metabolites. Injured limbs had 98 upregulated and 50 downregulated metabolites compared with sham-injured limbs, after correction for false discovery rate [116]. Porphyrin metabolism was upregulated while steroid hormone biosynthesis and purine metabolism were down-regulated. PCA revealed distinct grouping of injured and sham-injured metabolic profiles apart from one outlier and was associated with 57.9% of the variability. The outlier was an injured limb which clustered with sham-injured limbs in PCA. PLS-DA revealed distinct groupings of injured and sham-injured metabolic profiles and was associated with 31.9% of the variability. Similarly, hierarchical clustering revealed clear grouping of injured vs. sham-injured limbs, except for the same outlier detected by PCA.

Clustering validation indicated that 3 clusters was appropriate (**Figure 4.3D**). The top ten ensemble clustering outputs combined with the mummichog algorithm found porphyrin metabolism, arachidonic acid metabolism, and purine metabolism (**Figure 4.5A**).

4.4.4.3 Injured and Contralateral-to-Injured Limbs have Minor Differences in Synovial Fluid Metabolic Profiles. Univariate analysis of injured vs. contralateral-to-injured groups found no significant metabolic features. PCA also indicated similar metabolic profiles for the first 5 components. However, PLS-DA revealed distinct clustering of injured and contralateral-to-injured limbs, with all but one metabolic profile grouping appropriately. Hierarchical clustering revealed no distinct groupings.

Two clusters were deemed optimal from clustering validation. Ensemble clustering found that injured and contralateral-to-injured limbs show altered purine metabolism, N-glycan

biosynthesis, porphyrin metabolism, primary bile acid biosynthesis, glycerophospholipid metabolism, pantothenate and CoA biosynthesis, metabolism of xenobiotics by cytochrome p450, Inositol phosphate metabolism, glycosphingolipid biosynthesis, phosphatidylinositol signaling system, pyrimidine metabolism, TCA cycle, alanine, aspartate and glutamate metabolism, and arachidonic acid metabolism.

4.5 Discussion

Early therapeutic interventions are needed to prevent or slow the progression of PTOA. In this study, we address several critical gaps in the early response (i.e., 7 days) of the injured joint, including (1) the response of subchondral bone tissue modulus to joint injury and (2) which bone structural, material, and metabolic outcomes are local (i.e., injured joint only) or systemic (i.e., injured and contralateral-to-injured).

Epiphyseal and subchondral bone microarchitecture both undergo bone loss 7 days after joint injury. Previous studies with this murine injury model also show reduced epiphyseal bone microarchitecture 7-10 days after injury [34, 66, 93, 106, 119] (**Table 4.1**). However, our study found a 10.8% decrease in BV/TV and a 5.5% decrease in Tb.Th compared to 18-40%, and 18-24% decreases in these measures, respectively, from other studies [34, 66, 93, 106]. Previous work reports 3-7% decrease in SCB.Th 7 days after joint injury [34, 42], but we detected a larger (~12%) decrease. A potential explanation for these differences is that we studied skeletally mature mice (19-weeks old), whereas the previous studies utilized skeletally immature mice (10-11 weeks old)[34, 66, 93, 106]. These results demonstrate that early changes to the epiphysis and subchondral bone plate after injury are likely sensitive to skeletal maturity.

Bone undergoes transient thinning after joint injury which then reverses[34, 66, 93, 106, 119]. The sclerotic bone of later-stage OA is less stiff[34, 66, 93, 106, 119]. However, the initial changes to subchondral bone tissue material properties after joint injury have not been reported[125, 126]. We found that injury did not significantly impact subchondral bone modulus ($p=0.052$). However, our study may be underpowered to detect these changes. The possibility that subchondral bone modulus increases soon after joint injury is important for considering the impacts of the injury on joint loading and cellular mechanotransduction[127, 128].

Changes to bone structure and material properties can result from altered bone deposition, resorption, or both. Therefore, we assessed osteoclast number density and quantified the epiphyseal mineralizing surface. Our results showed an increase in osteoclast number density but not bone formation surface following joint injury. These results demonstrate that the early bone loss in our mouse model is primarily attributable to increased bone resorption.

Our experimental design allowed us to ask whether early bone changes following traumatic injuries affected the contralateral limb. We found that bone microarchitecture decreased and osteoclast number increased for both injured and contralateral-to-injured limbs. Injury and loaded side had additive effects of similar scale on early bone loss for epiphyseal BV/TV, BMD, and Tb.Th. These results improve our understanding of mouse models of PTOA because there are clear impacts to the biological and mechanical environments of both knees soon after the joint injury. Future studies should utilize sham-injured mice as controls for each time point to avoid confounding effects from systemic responses to injury. Importantly, it is not understood if changes to the contralateral-to-injured limb are transient or if they later progress towards PTOA as in the injured limb. It is also not known whether other rodent models of PTOA (e.g., DMM,

ACLT) produce similar contralateral limb effects at early timepoints, since the surgical incision confounds the early response.

Synovial fluid is integral to joint health, serving as a lubricant for joint articulation and a nutrient source for joint tissues [129]. This study contributes to a growing body of work that demonstrates that distinct shifts occur in synovial fluid metabolism in the first week post joint injury[37] and are consistent with shifts in whole joint metabolism[38]. Our synovial fluid metabolic univariate analysis revealed that 148 metabolites were dysregulated between injured and sham-injured knees. Ensemble analysis, an analytic tool introduced to synovial fluid metabolomics in this report, found that injured and contralateral-to-injured limbs shared many common pathways. These findings do not contradict the univariate analysis, because while ensemble clustering identifies metabolites that are common between groups, it does not identify the direction (i.e., upregulated or downregulated) of any differences between the groups.

We also wanted to understand which pathways were common to injured and contralateral-to-injured limbs, since these data would inform which, metabolic shifts are systemic. Several pathways were common to injured and contralateral-to-injured limbs but not injured, contralateral-to-injured, and sham-injured limbs, indicating that there were systemic shifts in metabolism after injury. Taken together, univariate and ensemble data suggest that there are pathways specific to the injured limb at 7d after injury, but also that many metabolic shifts extend to the other joint. These data suggest that the metabolic response to joint injury is very rapid and by 7 days after injury is systemic. To elucidate metabolic shifts specific to injury, future studies are needed that evaluate time points even earlier than 7 days.

Our study had several limitations. The non-invasive mouse injury model does not allow differentiation between the effects of injurious-level loading and ACL rupture on subchondral bone changes. However, there was not a significant correlation between peak load and any bone measures. We were unable to directly confirm ACL rupture for the injured limbs because of the synovial fluid extraction procedure which can inadvertently transect the ACL. However, we verified ACL rupture by the characteristic release in compressive load (**Figure 4.1F**)[34, 119] and laxity changes compared to the contralateral joint. Previous studies show that the release in compressive load indicates ACL rupture, as verified by later dissection[34, 119]. Another limitation is that embedding bone in PMMA significantly stiffens bone tissue compared with the hydrated condition[123]. However, preparing the subchondral bone plate for microscale modulus measurement required stabilizing this small structure with an infiltrating embedding material. This study was focused on the early response to joint injury. Additional timepoints would provide useful information about the trajectory of changes to subchondral bone and synovial fluid metabolism. Another important limitation was the small sample size (n=8 / group; N=16). Changes in subchondral bone modulus may have required additional mice for detection.

In summary, this study finds that acute bone loss 7 days after joint injury occurs in the injured and contralateral-to-injured limbs, and that these changes are accompanied by dysregulated synovial fluid metabolism. Our results implicate rapidly changing structural and biological environments within both injured and contralateral-to-injured joints that has the potential for influencing the progression to PTOA.

4.5 Acknowledgements

This research was made possible by the Department of Mechanical & Industrial Engineering and the College of Engineering at the Montana State University. We appreciate assistance with microCT analyses from the Center for Advanced Orthopedic Studies μCT Core at Beth Israel Deaconess Medical Center as well as assistance with histological sample preparation from Maria Jerome. Contents in this chapter were previously published [39].

CHAPTER FIVE

OSTEOCHONDRAL FLUID TRANSPORT IN AN EX VIVO SYSTEM

Contribution of Authors and Co-Authors

Manuscript(s) in Chapter(s) 1

Author: Brady David Hislop

Contributions: Experimental design, data collection, data analysis and interpretation, manuscript drafting, revision of manuscript.

Co-Author: Ara K. Mercer

Contributions: Data collection, revision of manuscript.

Co-Author: Alexandria G. Whitley

Contributions: Data collection, revision of manuscript

Co-Author: Erik P. Myers

Contributions: Experimental design, data collection, revision of manuscript

Co-Author: Chelsea M. Heveran

Contributions: Revision of manuscript

Co-Author: Ronald K. June

Contributions: Experimental design, revision of manuscript

Manuscript Information

Brady David Hislop, Ara K. Mercer, Alexandria G. Whitley, Erik P. Myers, Chelsea M. Heveran,

Ronald K. June

Osteoarthritis and Cartilage

Status of Manuscript:
☐ Prepared for submission to a peer-reviewed journal
☒ Officially submitted to a peer-reviewed journal
☐Accepted by a peer-reviewed journal
☐Published in a peer-reviewed journal

Elsevier
10/16/23
https://doi.org/10.1101/2023.10.13.562188

Abstract

Alterations to fluid transport from bone-to-cartilage may contribute to the development of osteoarthritis. However, many questions remain about fluid transport between these tissues. The objectives of this study were to (1) test for diffusion of 3kDa molecular tracers from bone-to-cartilage and (2) assess potential differences in bone-to-cartilage fluid transport between different loading conditions. Osteochondral cores extracted from bovine femurs (N=8 femurs, 10 cores/femur) were subjected to either no-load (*i.e.*, pure diffusion), pre-load only, or cyclic compression (5±2% or 10±2% strain) in a two-chamber transport system with the bone compartment filled with a 3kDa tracer. Tracer concentrations in the cartilage compartment were measured every 5 minutes for 120 minutes. Tracer concentrations were analyzed for differences in beginning, peak and equilibrium concentrations, loading effects, and time-to-peak tracer concentration. Peak tracer concentration in the cartilage compartment was significantly higher compared to beginning and equilibrium tracer concentrations indicating fluid transport from bone to cartilage. Cartilage-compartment tracer concentration was influenced by strain magnitude, but no time-to-peak relationship was found when comparing strain magnitudes. This study shows that osteochondral fluid transport occurs from bone-to-cartilage with 3kDa dextran molecules. These are much larger molecules to move between bone and cartilage than previously reported. Further these results demonstrate the potential for cyclic compression to impact osteochondral fluid transport. Determining the baseline osteochondral fluid transport in healthy tissues is crucial to elucidating the potential mechanisms of progression and onset of osteoarthritis.

5.2 Introduction

Osteoarthritis (OA) affects >500 million people each year [49]. The current standard of care for OA typically includes treatments such as pain management and exercise until an invasive total joint replacement is required. Mechanical and biological interventions that affect the trajectory of OA progression may help mitigate the physical and financial burdens of the disease. However, to design potential therapeutic interventions, a greater understanding of how fluid is transported between the tissues of the synovial joint is needed.

In the progression of osteoarthritis, structural and material changes to bone and cartilage may influence fluid transport, with repercussions to the health of the synovial joint [31]. In OA, the osteochondral interface (cement line to tidemark)[29] develops microcracks and is invaded by vasculature, leading to greater fluid transport between bone and uncalcified cartilage[29]. Increased fluid transport exposes cartilage to cytokines and proteases produced by bone[28, 29]. These changes occur alongside dysregulation of chondrocyte metabolism, which may contribute to other OA changes (*e.g.,* hypertrophic chondrocytes)[43, 68]. The sclerosis of subchondral bone and changes in cartilage permeability may further contribute to differences in how fluid moves within the diseased joint[55].

While altered fluid transport has been implicated in osteoarthritis for years[55], gaps in understanding persist about how fluid moves between healthy bone and cartilage, and how this transport depends on tissue strain. Fluid transport contributes to mechanosensation and tissue homeostasis in cartilage and bone [12, 130]. In addition, recent data show that small molecules (376Da, 575Da, and 1.55kDa) [20, 22, 131] diffuse from bone-to-cartilage. This is significant because a permeable osteochondral interface suggests new mechanisms for chondrocyte nutrition

and cartilage-bone crosstalk (*e.g.,* loading-induced pressure gradients that drive convection). Whether larger molecules can travel from bone-to-cartilage is not yet tested but is important to understand because biological molecules that would be found within bone, such as insulin (5kDa), are at least 3kDa in size. Furthermore, if the permeability changes with the progression of OA[55], the disrupted crosstalk may influence OA progression[29]. Deformation-induced interstitial fluid flow may also play an important role in molecular transport from bone-to-cartilage. However, the effects of compression on fluid transport from bone-to-cartilage in healthy tissues are undetermined. Defining the relationship between fluid transport and strain is necessary for improving our understanding of bone-cartilage fluid transport in synovial joints.

In this study, we look to address several critical gaps in our understanding of fluid transport across the osteochondral interface. First, we test for diffusion of 3kDa fluorescent dextran from bone-to-cartilage. Next, we look to quantify the effect of strain magnitude on bone-to-cartilage fluid transport. Finally, we analyze the effect of strain magnitude on time-peak concentration. Measured concentrations for each experimental group were compared to determine potential effects of strain magnitude and time on bone-to-cartilage fluid transport. The results provide evidence that that bone-to-cartilage fluid transport of uncharged molecules at least 3kDa in size most likely occurs in healthy joints and potentially mediates crosstalk between bone and cartilage through deformation.

5.3 Methods

5.3.1 Bovine Osteochondral Core Extraction

Bovine femurs were obtained from a local butcher (N=8). During sample processing the distal ends of the femurs were hydrated consistently with phosphate buffered saline (PBS). First,

the femur was trimmed to create two flat surfaces directly posterior to the condyles using a band saw (Supplemental Figure 1). Next using an 8mm bone coring reamer attached to a drill press (Supplemental Figure 1), ten cores were drilled to a depth of ~20mm (n=5 per condyle) and extracted by trimming bone with band saw. The bone coring tool was continuously hydrated with ice water to minimize temperature increase during coring. After extraction cores were immediately placed in PBS and stored at -80˚C.

5.3.2 Osteochondral Core Experimental Preparation

Experiments were randomized each experimental day (Supplemental File 1), assigning the cores to an experimental group. Four experimental groups included pure-diffusion (*i.e.,* no-loading), pre-load only, 5±2% cyclical compression (1.1Hz), or 10±2% cyclic compression (1.1Hz). On the day of the experiment, cores were removed from the -80˚C freezer and placed in a 37˚C water bath for 5 minutes. The PBS was then replaced, and the core was allowed to equilibrate for 33 minutes. After equilibration, cores were trimmed to ~12mm in height, and the bone face was ground to create a perpendicular angle between the loading platen and the articular surface. A 1/32” thick rubber sheet (McMaster-Carr) with 3mm diameter centered hole was pulled over the core until snug around the osteochondral interface (**Figure 5.1A-B**), the core was then placed into the bioreactor with the bone side into the bottom chamber (bone fluid chamber).

5.3.3 Experimental Procedures

After securing the core in the bioreactor (**Figure 5.1A-B**) with the rubber sheet snug around the osteochondral interface, the cartilage chamber was secured to create two separate fluid chambers. 2mL of 13μM 3kDa dextran (Invitrogen)[132] was added to the bone chamber

through an injection port. The port was then sealed (Gorilla Tough & Clear Double Sided Adhesive Mounting Tape). A peristaltic pump (15mL/min) was then connected to the fluid ports, and the cartilage chamber was filled with 2mL of PBS. For all studies duplicate 100µL aliquots ($t=0^-$) were immediately sampled from the cartilage chamber and placed in a 96-well plate (Fisherbrand^{TM}). For pure-diffusion studies the sampled fluid was immediately replaced with 200µL of PBS and the pump was started, after which two more 100µL aliquots ($t=0^+$) were sampled and again replaced with 200µL of PBS. Subsequently aliquots were sampled with PBS replacement from the cartilage chamber every 5 minutes for two hours. For pre-load only and cyclical compressive studies, a 3.5N compressive preload was applied (~70kPa), and the position of loading platen was recorded to define the 0% strain level. Immediately after pre-load two 100µL aliquots ($t=0^+$) were sampled, and replaced with 200µL of PBS as the cyclical compression experiments were started. Aliquots were then sampled from the cartilage chamber every 5 minutes for two hours and replaced with 200µL of PBS each time. For pre-load only studies the $t=0^+$ aliquots were taken ~15s after pre-load. Between sampling, the 96-well plate was covered with aluminum foil to minimize light exposure.

5.3.4 Fluorescent Intensity Studies

Each day calibration curves were generated to calculate dextran concentration (1.3nM-2.8µM) from fluorescence intensity. At the end of each experiment the respective plates were analyzed with a fluorescent plate reader (595/615nm excitation/emission, BioTek, Synergy H1 Microplate reader). All concentrations were fit using a 2nd-order polynomial with a zero intercept.

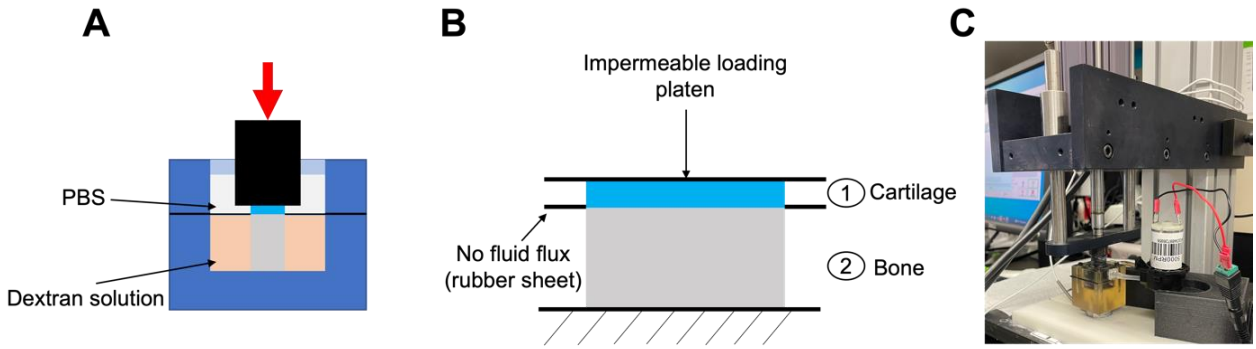

Figure 5.1 Schematics and visualization of experimental conditions for osteochondral fluid transport studies A) Cross-section of the bioreactor and loading platen, showing the cartilage fluid chamber with PBS separated from the bone fluid chamber with dextran solution by a rubber sheet B) Free body diagram showing the forces and boundary conditions acting on the osteochondral cores C) Experimental set-up for loading studies showing the peristaltic pump attached to the bioreactor circulating the fluid in the cartilage chamber.

5.3.5 Statistical Analysis

5.3.5.1 Analysis of Dependence of Peak Intensity on Experimental Group. Cartilage fluid chamber concentrations at beginning ($t=0^-$), peak, and equilibrium were analyzed using mixed model analysis of variance (ANOVA). The peak tracer concentration was evaluated at 15-minutes for consistency, as the time to peak concentration was not consistent. Fixed effects included strain magnitude (*i.e.* no-loading, pre-load only, 5% strain, 10% strain), and time-point (*i.e.* beginning, peak, equilibrium). The random effects in the model included the location on the femur where tissue was harvested and the specimen ID. The model included the interaction term between the fixed effects. To meet ANOVA assumptions of residual normality and equal variance measured concentrations were natural log-transformed. *Post hoc* analysis was performed for significant main effects or for interactions while maintaining a family-wise error rate of 0.05 using Tukey's multiple comparisons correction.

5.3.5.2 Analysis of Dependence of Peak Intensity on Time The effect of strain magnitude on time-to-peak concentration was analyzed using one-way ANOVA. All ANOVA assumptions were verified prior to data interpretation.

5.4 Results

5.4.1 Validation of Two-Fluid Chamber Bioreactor

Before performing fluorescent tracer concentration studies for the experimental conditions, we validated the baseline change in tracer concentration between the two fluid chambers using an impermeable aluminum cylinder. For all tests (n=3) we placed 13μM dextran solution in the bone fluid chamber. We tested system leakage by placing a rubber sheet with no center hole and found minimal change in tracer concentration in the cartilage chamber. Using the aluminum cylinder (8mm diameter) we determined the baseline tracer concentration increase in the system to be ~5nM (**Figure 5.2A**).

5.4.2 Dextran Tracer Concentration Changes with Time and Depends on Strain

Tracer concentrations in the cartilage fluid chamber were significantly different between time-points ($p<0.001$) and strain magnitudes ($p<0.001$) (**Figure 5.2,** Table C1). *Post hoc* comparisons of time points showed significantly higher tracer concentrations at peak compared to both beginning ($p<0.001$) and equilibrium ($p<0.001$) times, demonstrating osteochondral fluid transport from bone-to-cartilage. Furthermore, *post hoc* comparisons of strain magnitudes revealed significantly higher tracer concentrations for the 5% mean strain magnitude compared to the pure-diffusion group ($p<0.001$). All other *post hoc* comparisons were not significant.

These results suggest that 5% mean strain impacts the transport of 3kDa dextran molecules from bone-to-cartilage.

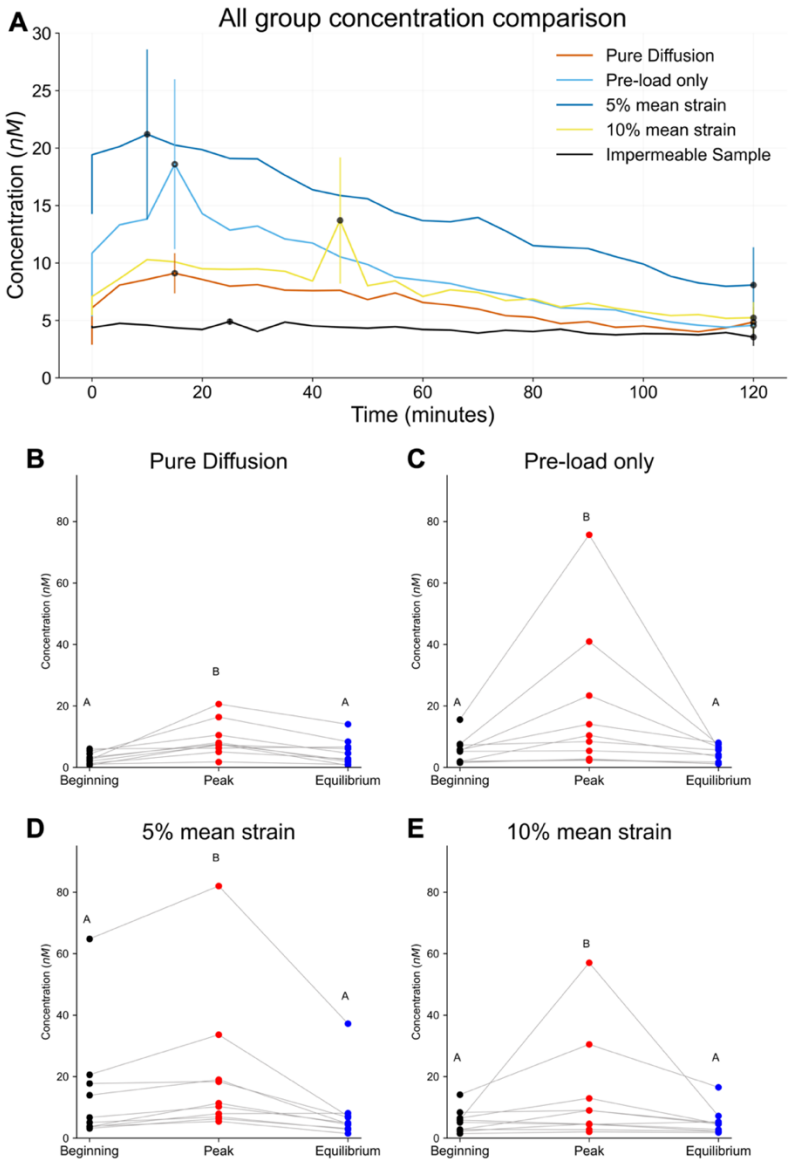

Figure 5.2 Comparison of time dynamics of mean tracer concentrations, and line series plots showing changes in between beginning (0^-), peak, and equilibrium (120 minutes). A) Dynamics of tracer concentration changes over two hours compared to the steady state impermeable tracer concentration B) Pure-diffusion studies C) Pre-load only studies D) 5% mean strain studies E) 10% mean strain studies. Mean represented by the black crossbar, median represented by the orange crossbar in each violin plot. For each subplot the letters A and B represent group differences.

5.4.3 Comparison of Time to Peak Equilibrium Reveals no Effect of Experimental Condition

The time-to-peak tracer concentration was not significantly impacted by experimental conditions ($p=0.450$).

5.5 Discussion

Osteochondral fluid transport has long been neglected in the literature until the onset of OA where vascular invasion into articular cartilage is observed [29]. The osteochondral interface is often considered an impermeable boundary that prevents molecular crosstalk between bone and cartilage[29]. Thus, synovial fluid is often considered the sole source of articular cartilage nutrition. However, recent studies with small tracer molecules and the data presented here show the limitations of this prior understanding [19, 20].

This study provides novel data on the transport of 3kDa molecules from bone-to-cartilage (*i.e.,* osteochondral fluid transport) in an *ex vivo* osteochondral core system. We found that tracer concentrations changed with time, reaching a peak within a few minutes. These results, together with prior studies of smaller molecules (*e.g.,* 376Da), provide evidence that uncharged molecules can move from bone-to-cartilage[20]. Bone is highly metabolically active and small molecules produced by this tissue could have roles in crosstalk with cartilage that are currently underappreciated. Future studies should consider molecule size, charge, and shape[133] on diffusion from bone-to-cartilage.

We also investigated whether fluid transport between bone and cartilage depends on the magnitude of cyclic compressive strain. Our results demonstrate that the 5%±2% strain increases the peak tracer concentration compared with the pure-diffusion condition. Interestingly, the other

strain groups did not differ from pure diffusion. A potential explanation for this lack of influence by the larger strain could be that the cartilage was not fully unloaded (*i.e.,* tissues were unloaded to 8% strain). It is possible that pore networks of cartilage cannot fully open without greater unloading, limiting the ability of fluid to convectively and/or diffusively move from bone to cartilage. The range of 3%-7% strain in the lower strain magnitude group may better allow opening and closing of pore networks in cartilage. However, whether pore network opening in cartilage is an important regulator of convective fluid transport from bone-to-cartilage requires further investigation. Studies should consider a greater range of peak and unloading strains as well as strain rates.

Finally, we investigated the impacts of strain magnitude on time-to-peak concentration. Time-to-peak concentration was not significantly impacted by strain magnitude. These results support our findings of convective fluid transport from bone-to-cartilage, as time-to-peak is not affected by strain magnitude suggesting strain isn't significantly impacting bone-to-cartilage diffusion.

There are several limitations to this study. Manual sampling volume replacement limited our temporal resolution and likely diluted cartilage fluid chamber concentration. Future studies should consider building a continuous fluorescent measurement system. Our studies lacked spatial resolution of tracer movement into cartilage. Studies should couple tracer concentration and imaging to see movement of tracer into cartilage. Finally, our study does not consider how tissue mechanical properties may impact on bone-to-cartilage fluid transport. Future studies should incorporate finite element modeling to study relationships between bone-to-cartilage molecular flux and tissue mechanical properties.

In conclusion, we found bone-to-cartilage fluid transport in an *ex vivo* system, suggesting that the current paradigm of an impermeable osteochondral interface should be reconsidered. The implications of increased bone-to-cartilage fluid transport in health are not well understood and need further study. By establishing the baseline molecular flux from bone-to-cartilage we will improve our understanding of joint physiology which may lead us one step closer to new treatments for OA.

5.6 Acknowledgements

We would like to thank Dr. Priyanka Brahmachary for procuring the bovine femurs, and Alexander Springer for helping with the initial experimentation.

CHAPTER SIX

CARTILAGE AND BONE MATERIAL PARAMETERS CHANGES ASSOCIATED WITH OA PROGRESSION INCREASE OSTEOCHONDRAL FLUID FLUX

Contribution of Authors and Co-Authors

Manuscript(s) in Chapter(s) 1

Author: Brady David Hislop

Contributions: Model development and analysis, manuscript development, revision of manuscript.

Co-Author: Kosar Safari

Contributions: Model development.

Co-Author: Chelsea M. Heveran

Contributions: Revision of manuscript.

Co-Author: David Pierce

Contributions: Model development, manuscript development, revision of manuscript.

Co-Author: Ronald K. June

Contributions: Manuscript development, revision of manuscript.

Manuscript Information

Brady David Hislop, Kosar Safari, Chelsea M. Heveran, David Pierce, Ronald K. June

In Prep

Status of Manuscript:
☒ Prepared for submission to a peer-reviewed journal
☐Officially submitted to a peer-reviewed journal
☐Accepted by a peer-reviewed journal
☐Published in a peer-reviewed journal

Abstract

Changes to osteochondral fluid transport could pay a major role in the development and progression of osteoarthritis. However, many question persist about the amount of fluid transport that occurs between bone and cartilage in health and disease. The objectives of this modelling study were to (1) predict the baseline fluid flux between bone and cartilage during cyclic compression (2) investigate how cartilage and bone deterioration impact osteochondral fluid transport (3) understand the change in osteochondral fluid transport with early OA. A biphasic viscoelastic model incorporating collagen fiber orientations and the proteoglycan matrix was modeled with 23 layers, with an underlying layer of subchondral bone. For cyclic compression experiments the face shared by cartilage and bone elements was evaluated for net fluid flux for a 15-minute simulation. Our model predicted a net fluid flux from cartilage into bone during cyclic compression at both 5 % and 10 % mean strain. Further, our model predicted that proteoglycan loss and subchondral bone modulus decreases would impact osteochondral fluid flux. These results show that with the progression of OA osteochondral fluid transport increases. Overall, these results suggest that osteochondral fluid flux could be a player in the development of OA. By providing quantitative predictions of osteochondral fluid flux, we can begin to understand how changes in net osteochondral fluid flux could impact the mechanical and biological responses of both bone and cartilage in health and disease.

6.2 Introduction

Osteoarthritis (OA) is a degenerative joint disease that impacts millions of people each year [49]. Currently no disease modifying treatments exist for OA forcing people to manage pain

and loss of function until a total joint replacement. Interventions that alter the progression of OA, may help mitigate pain and improve quality of life, without the need for an invasive total joint replacement. However, to design these interventions a greater understanding of the OA as a whole joint disease is needed.

The progression of OA leads to structural, mechanical and biological changes to cartilage and bone that may impact fluid transport. It is well established, that with OA the osteochondral interface becomes more permeable [41, 54], exposing cartilage to cytokines and proteases produced by bone [28, 29]. Chondrocyte metabolism is impacted by these changes [43, 68] and may lead to further joint degradation. The loss of proteoglycans increases in bone permeability, and changes in bone modulus may contribute increased osteochondral fluid transport in OA.

Osteochondral fluid transport is altered during the progression OA [41, 54], however, gaps in our understanding persist about the fluid mechanics of this transport in health and disease. Fluid transport plays import mechanical and biological roles in the joint. Mechanically fluid transport leads to interstitial fluid pressurization of cartilage, protecting chondrocytes from excessive mechanical loads [134]. Fluid movement also provides nutrients, and biological signals to bone and cartilage cells impacting their expression [10-13, 15, 99, 127, 132]. Recent studies have implicated osteochondral fluid transport as another component of joint fluid transport [19, 20, 22, 135]. This is significant because osteochondral fluid transport may provide additional nutrients to cartilage, especially in the deep zone, and impact joint fluid mechanics. Whether osteochondral fluid transport impacts overall joint fluid mechanics is unknown, but it could influence cartilage pressurization. Furthermore, changes in the material properties of cartilage and bone associated with OA may lead to increase osteochondral fluid transport.

However, the fluid mechanics that drive osteochondral fluid transport in health and disease are not well understood. Defining the material properties that influence osteochondral fluid transport in health and disease is crucial to understanding OA as a whole joint disease.

In this study we look to address several critical gaps in our understanding of the fluid mechanics driving osteochondral fluid transport in health and disease. First, we look to simulate the net fluid flux across the osteochondral interface during 15-minutes of cyclic compression at 5% and 10% mean strain. Next, we perform a parameter sweep of cartilage and bone material property changes associated with OA to elucidate potential mechanisms of altered fluid transport. Finally, simulated osteochondral fluid transport in an approximated model of early OA to understand the effect on joint fluid transport. Net fluid fluxes for each simulation were compared to determine the effect of material property changes. The results provide evidence of a net fluid flux from cartilage to bone during cyclic loading and altered osteochondral fluid transport with the progression of OA.

6.3 Methods

6.3.1 Model Geometry

Osteochondral cores (2mm height, 4mm radii, 5˚ slice), were modeled in FEBio Studio [90] (**Figure 6.1A**). The boundary conditions simulated our experimental work on osteochondral fluid transport in an ex-vivo system [135]. The bottom surface of bone was fixed in all displacement degrees of freedom (x, y, z), the lateral cut surfaces were set to no displacement normal to their faces (**Figure 6.1A**), the radial edge of the core was set to zero fluid pressure (i.e., free draining surface), and the top surface (i.e., articular surface) was prescribed a displacement (e.g., 5%±2% strain). The two-millimeter height of the model was split evenly

between subchondral bone and articular cartilage. To lessen computational complexity, we only modeled the first millimeter of subchondral bone. The bone mesh comprised of 20 z-stacks (0.9 bias towards osteochondral interface), 2 theta slices, and 32 radial segments (.9 bias towards the radial edge). To model cartilage we created 23 individual z-stacks each meshed with 1 z-stack, 2 theta slices, and 32 radial segments (.9 bias towards the radial edge). Each cartilage stack was given its own material model, and bone comprised of one material model. After meshing and defining material models, each separate geometry was merged, where any coincident nodes were welded into a single node.

6.3.2 Cartilage Constitutive Model

A biphasic viscoelastic continuum model with statistical fiber orientations incorporated into the permeability was chosen to model cartilage [2]. The solid fraction of this model incorporates the proteoglycan matrix, and collagen fiber network. A neo-Hookean strain energy function is used to capture the largely proteoglycan solid matrix [3]. The contribution of the collagen fiber fabric is captured in an Exponential-Power law formulation that incorporates the statistical fiber orientations [2]. The statistical fiber orientations are considered for three distinct regions including the superficial, middle, and deep zones with diffusion tensors of [1, 1e-1, 1e-1, 1e-6, 1e-6, 1e-6], [1, 1, 1, 1e-6, 1e-6, 1e-6] and [1e-1, 1e-1, 1, 1e-6, 1e-6, 1e-6], respectively. The permeability is modeled as a strain dependent anisotropic intrinsic permeability (see Eq 17, of [2]), which incorporates the initial Darcy permeability, statistical fiber orientations, and solid volume fraction. For model specification we defined depth dependent relationships for solid

volume fraction, collagen fiber fraction, initial Darcy permeability, and deformation dependence of the permeability.

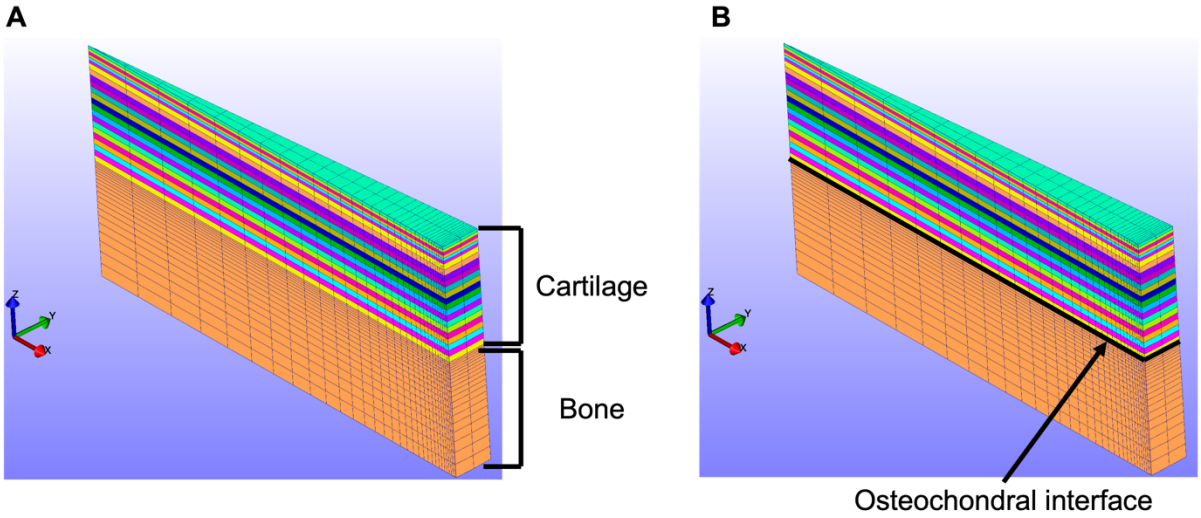

Figure 6.1 Finite element model of osteochondral plug. A) Mesh showing the 23 z-stacks of cartilage, and 1 bone geometry with (20-mesh stacks). B) Mesh showing the osteochondral interface where the faces shared between bone and cartilage elements were analyzed for net fluid flux.

6.3.3 Bone Constitutive Model

A biphasic orthotropic elastic model [136] was chosen to model subchondral bone. The solid fraction was assumed to be 0.945 throughout the subchondral bone layer as in our previous work [63]. The subchondral bone modulus was assumed to be density dependent with the largest modulus along the x-axis in our model coordinate system. The density of the subchondral cortical bone was assumed to be 1.92e-10 (ton/mm^3), which we used to approximate the modulus along the x-axis as 17.7 GPa [63, 136]. The young's modulus of y, and z, and shear modulus were as proportions of x-axis moduli [136]. The Poisson ratios were ν_{12}=0.405, ν_{13}=0.234, ν_{23}=0.427. The bone permeability was considered constant, at 90 mm^4/N*s [55].

6.3.4 Comparison of Imaging-Based Fluid Flux Studies to Predicted Fluid Flux

A 15-minute cyclic compression experiment was simulated at two strain magnitudes of 5%±2% and 10%±2%. For each mean strain level, we evaluated the z-fluid flux at the osteochondral interface by selecting the element faces shared between the cartilage and the bone elements (**Figure 6.1B**). The net z-fluid flux (i.e., osteochondral fluid flux) was calculated over the 15-minute interval by calculating the area under the time – z fluid flux curve for each face and summing. Finally, the summed area under the curve was multiplied by 144 to approximate the total osteochondral fluid flux over the 15-minute interval.

6.3.5 Parametric Study of Osteochondral Fluid Transport Changes w/ Progression of OA

To study the effects of mechanical and structural changes associated with early OA we performed a parametric study. Each adjusted model was compared to it's "normal/healthy" model with 90 $mm^4/N*s$ subchondral bone permeability, 17.7 GPa subchondral bone modulus, and no changes to proteoglycan content and permeability of superficial zone cartilage from original model [2]. Proteoglycan content impacts cartilage permeability thus these parameters were changes in tandem. Finally, to understand the potential interactive effect of each of the changes we ran an early OA model (**Table 6.1**). 15 minutes of cyclic compression were simulated, and the net osteochondral fluid transport was determined.

Table 6.1 Parameter sweep model values, cartilage permeability and proteoglycan loss in the superficial zone (SFZ) were coupled.

Model Parameters	Values	Early OA Parameters
Permeability SCB ($\frac{mm^4}{N*s}$)	100 - 140	140
Stiffness SCB (GPa, E_x)	10 - 20	20
Cartilage permeability increase ($\frac{mm^4}{N*s}$)	10% - 40%	40%
Proteoglycan loss SFZ (%)	20% - 80%	80%

6.4 Results

6.4.1: Net Osteochondral Fluid Flux from Cartilage-to-Bone during Cyclic Compression

The net osteochondral fluid transport occurred from cartilage-to-bone during 15 minutes of cyclic compression for both strain magnitudes. For the 5% mean strain condition, the predicted osteochondral fluid flux was -0.4921 mm/s, suggesting a net fluid flux from cartilage-to-bone during cyclic compression. For 10% mean strain, the predicted net osteochondral fluid flux was -5.5648 mm/s, suggesting net fluid flux from cartilage-to-bone.

6.4.2: Increased Bone Permeability does not Affect Convective Osteochondral Fluid Transport

The net osteochondral fluid transport across 15 minutes of cyclic compression was not impacted by increased bone permeability (<1% difference) when compared to “healthy” simulations.

6.4.3: Lower Subchondral Bone Modulus Impacts Convective Osteochondral Fluid Transport for 10% Mean Strain

The 5% mean strain models exhibited no difference in net osteochondral fluid flux across 15 minutes. Reducing the modulus along the x-axis (i.e., density dependent relationship with

moduli of other axes) to 12 GPa and 14 GPa led to an increase net osteochondral fluid flux into the subchondral bone from cartilage (22%, and 13.8%, respectively).

6.4.4: Proteoglycan Loss in the Superficial Zone of Cartilage Affects Osteochondral Fluid Flux at Both Strain Magnitudes.

At 5% mean strain 60% and 80% loss of proteoglycans increases osteochondral fluid flux (13.79%, and 34.14%, respectively) when compared to "normal" osteochondral model. Similarly, we an increase in osteochondral fluid flux for 10% mean strain at 60% and 80% proteoglycan loss (12.4%, and 25.4%, respectively). By contrast, at 40% proteoglycan loss we found a 13% decrease in osteochondral fluid transport.

6.4.5: Early OA Affects Net Osteochondral Fluid Flux in 5% Mean Strain but not 10% Mean Strain

To simulate the early OA changes in bone and cartilage material parameters we ran a model with 80% proteoglycan loss, an increased in subchondral bone plate modulus and permeability. At 5% mean strain we saw a nearly 10-fold increase in net osteochondral fluid flux. Whereas, at 10% mean strain we saw just a 10% increase in net osteochondral fluid flux.

6.5 Discussion

Fluid transport across the osteochondral interface occurs in both health and disease [19, 20, 22, 54, 135]. Recently studies have shown that physiologically relevant molecules (376 Da) [19, 20, 22] diffuse and are convectively transported (3kDa) from bone-to-cartilage [135]. Thus, cytokines and proteases produced by bone cells (e.g., osteoblasts) could impact chondrocyte

metabolism. However, the material properties that influence osteochondral fluid transport are poorly understood.

This study provides novel modelling data on mechanical properties that influence osteochondral fluid transport. We found that osteochondral fluid transport is strain dependent. Interestingly, we found that the net fluid flux across a 15-minute compression cycle occurred from cartilage-to-bone. Whereas our experimental results found the 3kDa dextran fluid surrogate, transported from bone-to-cartilage and was found throughout cartilage. A potential explanation for these conflicting results is mixing of the bone and cartilage fluid during cyclic loading. Our model showed that during cyclic compression the fluid flux across the osteochondral interface oscillated between cartilage-to-bone flux, and bone-to-cartilage flux. This would suggest that as fluid flux occurs from cartilage-to-bone during loading, the cartilage fluid would mix with the bone fluid. Thus, when unloading brings the fluid back into cartilage the fluid likely contains the molecular marker in bone. This mixing may occur throughout cartilage as well during cyclic compression eventually reaching the state observed in our experimental work. Future studies should consider larger strain magnitudes, analysis of fluid flux through all material layers, and account for osmotic swelling of cartilage.

We also investigated the effect of cartilage and bone material property changes associated with the early stages of OA on osteochondral fluid transport. Our results indicated that the loss of proteoglycans in the superficial zone and the alteration of subchondral bone modulus impacted osteochondral fluid transport. The loss of proteoglycans in the superficial zone of cartilage in the early stages of OA progression is well established [52]. These data suggested that for 5% and 10% mean strain that 60-80% losses in proteoglycans leads to increased osteochondral fluid

transport. Interestingly, for 10% mean 40% loss of proteoglycans in the superficial zone led to a decrease in osteochondral fluid transport. Given the lack of changes to cartilage material property changes in the middle and deep zones of this model the increase in osteochondral fluid transport is likely driven by altered bulk cartilage mechanics. Further changes could be expected with the loss of collagen fiber network integrity, which was not considered in this model. Decreased subchondral bone modulus led to increased osteochondral fluid transport for 10% mean strain simulations. These results suggest that during loading the subchondral bone plate modulus directly impacts the osteochondral fluid transport. Therefore, if other factors such as age, and injury also influence subchondral bone plate stiffness osteochondral fluid transport will change and could lead to the progression of OA.

Finally, we studied the impacts of the cartilage and bone material property changes, in a single model (**Table 6.1**). Our early OA model under 5 % mean strain predicted a 33.8 % increase in osteochondral fluid transport when compared to the “normal/healthy” model at 5 % mean strain. Whereas we only found a 10 % increase in osteochondral fluid transport when comparing the early OA model and “normal/healthy” model at 10 % mean strain. These results predict that in early OA osteochondral fluid transport increases. Interestingly, the 5 % mean strain group saw a greater relative increase than the 10 % mean strain group, suggesting lower strain magnitudes may be influenced by the early stages of joint degradation. Changes in osteochondral fluid transport may lead to chondrocytes and bone cells being exposed to cytokines, metabolites, inflammatory markers, etc. not seen in health. Thus, changes in osteochondral fluid transport could lead to aberrant cell responses that lead to the progression of OA. Therefore, to further our understanding of the impact of strain magnitude on osteochondral

fluid transport during the progression of OA, future studies need to explore larger strain magnitudes and a broader range of material property changes associated with the progression of OA.

There are several limitations to this study. We did not account for osmotic swelling which likely caused us to underestimate the effects of proteoglycan losses. Future studies should incorporate osmotic swelling as presented by Wang et al. [3]. Our studies focused on a small parameter sweep that did not consider the coupled changes of bone and cartilage from healthy to early OA. Future studies should perform a broader parameter sweep and model healthy to full OA changes. Finally, our study did not incorporate full joint unloading during cyclic compression. Studies could consider full joint unloading to understand if it influences osteochondral fluid transport. By furthering our understanding of the mechanical properties that drive osteochondral fluid transport we will improve the understanding of OA as a whole joint disease.

In conclusion we found osteochondral fluid transport at both strain magnitudes considered, providing additional evidence for connectively driven osteochondral fluid transport. Furthermore, we found that in early OA osteochondral fluid transport increases. The implications of increased fluid transport with progression of OA is that it could be a driving force behind disease progression. However, the impacts of cartilage and bone material property changes still need further investigation to understand the impacts on joint health. By establishing the material properties that influence osteochondral fluid transport we will improve our understanding of the progression of OA leading us one step closer to novel treatments.

6.6 Acknowledgements

We would like to thank Dr. Priyanka Brahmachary for procuring the bovine femurs.

CHAPTER SEVEN

ECCO: A PYTHON UI FOR PERFORMING ENSEMBLE CLUSTERING COMBINED WITH CLUSTERING OPTIMIZATION ON OMICS DATA

Contribution of Authors and Co-Authors

Manuscript(s) in Chapter(s) 1

Author: Brady David Hislop

Contributions: Model, code, and manuscript development, revision of manuscript.

Co-Author: Mark Greenwood

Contributions: Model development and revision of manuscript.

Co-Author: Chelsea M. Heveran

Contributions: Revision of manuscript.

Co-Author: Ronald K. June

Contributions: Revision of manuscript.

Manuscript Information

Brady David Hislop, Mark C. Greenwood, Chelsea M. Heveran, Ronald K. June

In Prep

Status of Manuscript:
☒Prepared for submission to a peer-reviewed journal
☐Officially submitted to a peer-reviewed journal
☐Accepted by a peer-reviewed journal
☐Published in a peer-reviewed journal

Abstract

Metabolomic studies have improved the understanding of a broad range of biological tissues, fluids, and systems. Typically, metabolomic analyses employ a workflow that starts with detecting peaks from mass spectrometry data and is followed by a series of statistical analysis aimed at identifying dysregulated metabolites, group differences, and group similarities in dysregulated metabolites and pathways. Generating these group similarities relies on clustering analyses. However, current clustering methods are highly subjective and can be prone to errors, indicating the need for an updated workflow that improves upon these issues. Here we present a novel metabolomics workflow that can produce unbiased, reproducible clustering results: ensemble clustering combined with cluster optimization (ECCO). The first step, clustering optimization, is used to identify an optimal number of clusters without bias. The second step, ensemble clustering, is then performed by finding the consensus clustering solution across thirteen distance algorithms. This step improves the repeatability of analyses and eliminates bias through eliminating the need to choose one distance algorithm in clustering solutions. We employ ECCO to analyze synovial fluid metabolites from patients with early and late osteoarthritis (OA). This method improves upon the detection of distinct metabolomic endotypes compared with conventional analyses. Furthermore, novel pathways were identified corresponding with different stages of OA. These results demonstrate the utility of ECCO in metabolomics workflows that involve clustering data. ECCO, which we provide as an open-source tool, can improve the repeatability, reliability, and ease-of-use of metabolomics analyses, and is therefore expected to increase the confidence of biological interpretation from these data.

7.2 Introduction

Clustering is a powerful data analyses technique that allows for the identification of groups in high-dimensional data. In biological research this is critical as clustering can help identify potential biomarkers of disease. The identified clusters of biomarkers are often enriched to determine the biological significance of these groups. However, many clustering methods exist and identifying the "correct" clustering solution remains non-trivial. Thus, continued efforts are needed to improve clustering methodologies to ensure the derived insights are repeatable and ultimately useful.

The selection of one clustering workflow over another will cause the resulting clusters to differ. Clustering workflows typically consist of data pre-processing, clustering, and optimization. Pre-processing aims to "adjust" the data to ensure that all variables are on the same scale. Clustering then takes the pre-processed data and combines variables into groups (i.e., clusters), before an optimization is performed to determine how many clusters should be selected (i.e., tightly grouped clusters that are spread apart). However, despite many advances in clustering algorithms there does not exist a one-size fits all clustering workflow. A simple example is the linkage function of agglomerative hierarchical clustering. Linkage functions are the criteria agglomerative hierarchical clustering uses to update the distance/dissimilarity between newly formed clusters and existing clusters. Thus, the selection of one over another will lead to different clusters being identified. Therefore, without considering any other steps of a clustering workflow multiple different clustering solutions are possible.

Identifying the optimal number of clusters in a dataset is critical step in an omics workflow. For example, in untargeted metabolomics studies, the identified clusters are then

analyzed to determine pathways associated with the metabolites in each cluster [11, 13, 32]. However, clustering algorithms only account for intra-cluster separation (*i.e.*, within-cluster spread), failing to account for potential overlap between clusters. In fact, clustering algorithms will identify clusters in any data set, even if the data do not appear to contain clusters (**Figure 7.1**). To address this issue, researchers have developed clustering optimization metrics that compare the compactness and separation of the resulting clusters [73-76]. However, the lack of consensus on the clustering optimization approach leads to their underutilization in data analyses.

Ensemble clustering has been proposed to mitigate the challenges of both clustering selection and the repeatability of clustering solutions [72]. To combine clustering solutions ensemble clustering measures the proportion of clustering solutions in which variables share a cluster. By performing ensemble clustering researchers are able to get a measure of the variables that consistently co-cluster avoiding the potential pitfalls of selecting a single mono-clustering solution[72]. However, despite a vase range of literature on clustering ensembles [72, 137-143], they remain underutilized in the omics field. The lack of easy-to-use ensemble clustering tools, and one-size fits all ensemble clustering impacts the usage of these improved clustering methodologies.

Here we outline the structure and usage of the ensemble clustering combined with clustering optimization user interface (ECCO UI). We describe the implementation of ECCO, where we utilize two correlation-based dissimilarity measures. Further, we provide two case studies showing how mono-clustering solutions can drastically differ and provide specific examples of how to interpret ensemble clustering results.

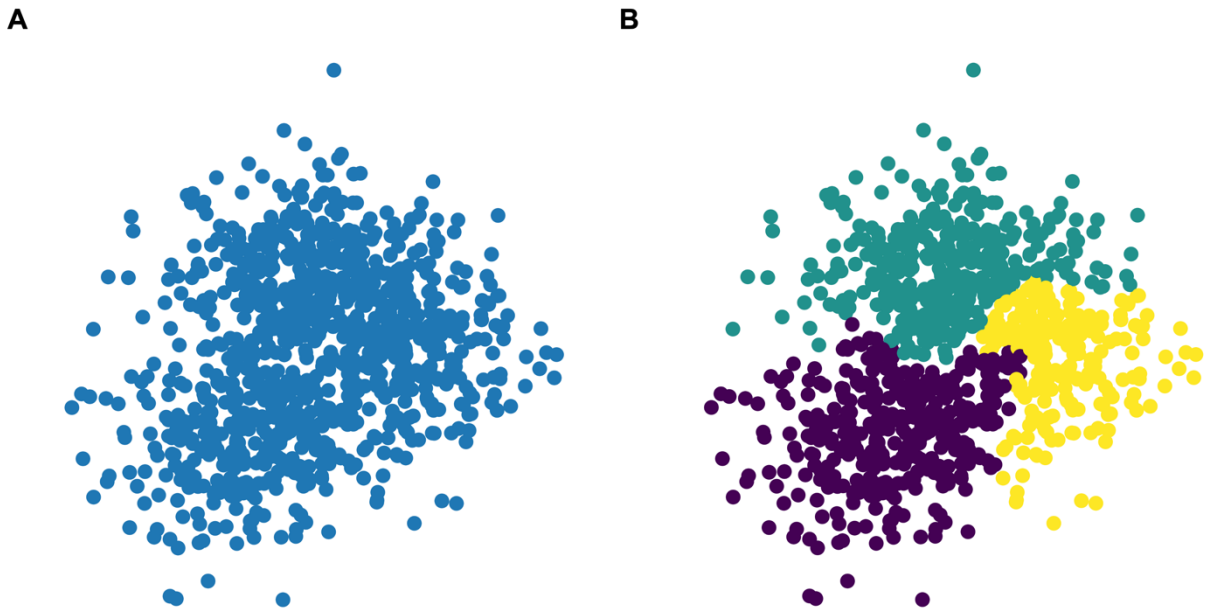

Figure 7.1 Clustering of 2D data with no clusters present. A) Randomly generated 2D data. B) Clusters identified using Ward-Euclidean agglomerative hierarchical clustering

7.3 Methods

7.3.1: Agglomerative Hierarchical Clustering

Agglomerative hierarchical clustering (AHC) is a type of hierarchical clustering that starts by considering each data object as its own cluster before combining data objects into clusters until a single cluster containing all data objects is reached. To achieve a hierarchy of clusters, the algorithms of AHC rely on two parameters: a dissimilarity measure and a linkage function. The dissimilarity measure describes how each data object relates to another in the data set. Often these dissimilarities are calculated in a pair-wise manner. In this paper we use two correlation-based dissimilarity measures [144] (**Figure 7.2**):

$$1 - |r(Y, Y')| \tag{1}$$

$$\sqrt{2(1 - |r(Y, Y')|)} \tag{2}$$

where r is a correlation measure (*e.g.*, Pearson's correlation coefficient) and Y and Y' are data objects.

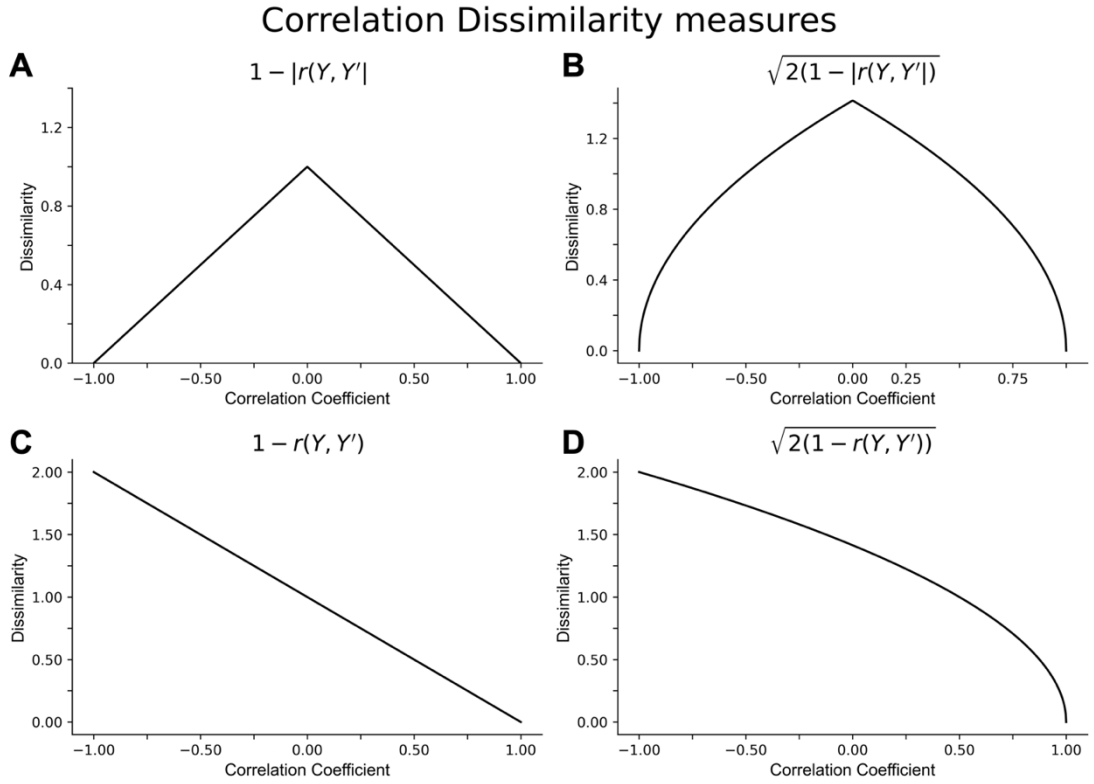

Figure 7.2 Absolute value correlation metrics compared to correlation-based metrics. A) Correlation dissimilarity (1 - |r(Y, Y')|) plotted for correlations -1 to 1. B) Square root based dissimilarity plotted for correlations -1 to 1. C) Comparison of correlation-based metric without absolute value to A). D) Comparison of square-root of correlation-based dissimilarity without absolute value B).

After determining the dissimilarity between each data object, AHC utilizes a linkage function to determine the hierarchy of clusters. There are many linkage functions. However, the four most commonly used in omics are Ward, single, complete, and average linkage functions. Each linkage function first determines the data objects or set of data objects closest (*i.e.*, smallest dissimilarity) to a data object or another set of data objects. Then the linkage function updates the dissimilarities between all other data objects or sets (*i.e.*, clusters). AHC is the result of repeating

each of these steps until the single all-encompassing cluster is obtained. After obtaining the single cluster a "flat cut" is made at a user-chosen level of hierarchy in the dendrogram (*i.e.*, tree-structure of AHC) to select the clusters (**Figure 7.3**).

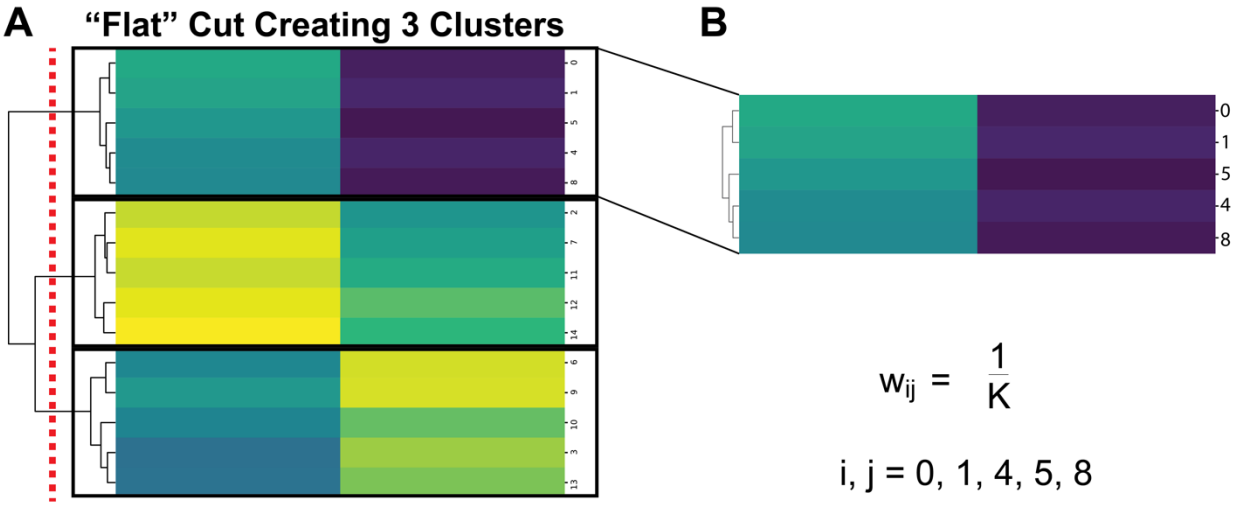

Figure 7.3 Selection and evaluation of single clustering solutions. A) "Flat" cut (red dotted line) through dendrogram to identify 3 clusters of interest. B) Example of evaluation of an identified cluster where w_{ij} is weight given to data objects, and K is the number of clustering solutions in the ensemble

Here, we implement an ensemble of agglomerative hierarchical clustering solutions. We note that there are many other clustering algorithms (*e.g.*, k-means) that cannot be performed in the dissimilarity/distance framework. However, our rationale for using AHC solutions is (1) that we can utilize a dissimilarity/distance framework and (2) the hierarchical structure allows for straightforward interpretation.

7.3.2: Clustering Optimization

Clustering optimization metrics or internal quality measures [143] address the question of how many clusters are optimal for a given set of clustering solutions. A broad range of clustering optimization metrics exist with the overall goal of determining the relationship between inter

cluster dissimilarity/distances (*i.e.*, distance between cluster centers), and intra-cluster distances/dissimilarities (*i.e.*, closeness of data within clusters). In this paper we focus on three optimization metrics that resemble the form of AHC linkage functions considered. To determine the "optimal" number of clusters using a clustering optimization metric, a set of 2 – C (where C is the largest number of clusters considered) clustering solutions are generated, and the optimization metric is calculated for each solution.

The average silhouette width [75], often referred to as the Silhouette metric, determines the optimal number of clusters by averaging the intra- and inter-cluster distance/dissimilarities:

$$\boldsymbol{Average\ Silhouette\ Width} = \frac{\sum_{k=1}^{K} \boldsymbol{SIL}(\boldsymbol{C_k})}{\boldsymbol{K}} \tag{3}$$

where K is the number clusters in the solution and $SIL(C_k)$ is defined as:

$$\boldsymbol{SIL}(\boldsymbol{C_k}) = \frac{\boldsymbol{b}(\boldsymbol{x}) - \boldsymbol{a}(\boldsymbol{x})}{\boldsymbol{max}\big(\boldsymbol{a}(\boldsymbol{x}), \boldsymbol{b}(\boldsymbol{x})\big)} \tag{4}$$

where x is the data objects in cluster k and b(x) is the separation between data objects x and all data objects not in k, and a(x) is the closeness between data objects in k. The largest Silhouette score between 1 and -1 represents the optimal clustering solution. The average linkage function of AHC and the Silhouette metric both use the average distance/dissimilarity and thus we use the Silhouette metric to optimize AHC solutions generated by the average linkage function.

The Calinski-Harabasz metric [73], also referred to the as the Pseudo F-statistic uses a sum-of-squares based metric to determine the optimal clustering solution:

$$CH = \frac{\frac{\sum_1^K |C_i| d(v_i, v)^2}{K - 1}}{\frac{\sum_1^K \sum_{x \in C_i} d(x, v_i)^2}{n - K}} \tag{5}$$

where K is the number of clusters, $|C_i|$ is number of data objects in cluster i, v_i is the center of cluster i, v is the center of all data objects, and n is the number of data objects in the data set. The maximum Calinski-Harabasz score represents the optimal clustering solution. Given the sum-of-squares-based measure of optimal clusters in this optimization metric, we use this with the Ward linkage function because of its sum-of-squares dependence.

The Davies-Bouldin index [74], calculates the optimal clustering solution by summing the maximum ratios of intra-cluster spread to cluster separation:

$$DBI = \frac{\sum_1^K F_{C_H}}{K} \tag{6}$$

Where K is the number of clusters in the clustering solution and F_{C_H} is:

$$F_{C_H} = \max_{C_H \neq C_j} F_{C_H} F_{C_j}$$

$$F_{c_H C_j} = \frac{f_1(C_H) + f_1(C_j)}{f_2(C_H, C_j)} \tag{7}$$

Where f_1 is the average distance/dissimilarity between data objects and their cluster centroids, and f_2 is the distance/dissimilarity between centroids. In contrast to the previously discussed metrics, the optimal solution for the Davies-Bouldin index occurs at the minimum value. Given that the Davies-Bouldin function sums that maximum ratios of intra-cluster spread to cluster separation, we match it with the complete linkage function because of its maximization step.

7.3.3: Ensemble Clustering

Ensemble clustering combines multiple clustering solutions together into an ensemble to determine the data objects that consistently co-cluster [142]. To generate an ensemble, multiple clustering solutions are generated by adjusting the hyperparameters (*e.g.*, number of clusters or linkage function) of clustering algorithms. Each of the clusters identified in these clustering solutions are then evaluated to determine the data objects that share a given cluster. Each time a data object shares a cluster with another data object it is given a weight of 1/N where N is the total number of clustering solutions in the ensemble. After evaluating the clusters of interest for each of the clustering solutions, the resulting weights are summed to generate a co-occurrence matrix, representing the frequency in which data objects share clusters:

$$a_{ij} = \frac{1}{K} \sum_{i,j,i \neq j}^{N} \partial_{ij} \tag{8}$$

where,

$$\partial_{ij} = \begin{cases} 1, & when\ points\ i\ and\ j\ share\ a\ cluster \\ 0, & otherwise \end{cases}, \tag{9}$$

K is the number of clustering solutions considered in the ensemble and N is the number of data objects being clustered.

The co-occurrence matrix gives a direct representation of how often each pair of data objects cluster together. To understand the data objects that consistently co-cluster a final clustering is performed on the co-occurrence matrix. This final clustering is performed by converting the co-occurrence to a dissimilarity (*i.e.,* 1- co-occurrence) and using a hierarchical linkage function.

Table 7.1 Agglomerative hierarchical clustering linkage functions, dissimilarity measures and optimization metrics used in the ensemble examples presented. Where Y and Y' represent the comparison of two data objects

Linkage	Dissimilarity measure	Optimization Metric
Ward	$1 - \|r(Y, Y')\|$	Pseudo F-stat. (Calinski-Harabasz)
Ward	$\sqrt{2(1 - \|r(Y, Y')\|)}$	Pseudo F-stat. (Calinski-Harabasz)
Complete	$1 - \|r(Y, Y')\|$	Davies-Bouldin Index
Complete	$\sqrt{2(1 - \|r(Y, Y')\|)}$	Davies-Bouldin Index
Average	$1 - \|r(Y, Y')\|$	Average Silhouette
Average	$\sqrt{2(1 - \|r(Y, Y')\|)}$	Average Silhouette

7.3.4: ECCO: Ensemble Clustering Combined with Clustering Optimization

Here we present an implementation of ensemble clustering, ensemble clustering combined with clustering optimization – ECCO. ECCO combines multiple clustering solutions together by optimizing each clustering within the ensemble using an optimization metric (**Table 7.1, Figures 7.3-4**). In this implementation of ECCO we provide the usage of two correlation-based dissimilarity metrics (**Table 7.1, Dissimilarity measures**, three linkage functions (**Table 7.1, Linkage**), and three optimization metrics (**Table 7.1, Optimization metric**). Euclidean distance between data objects is equivalent to a correlation-based dissimilarity where negative correlations are treated as further apart than 0 or positive correlations. By modifying the dissimilarity using absolute correlation, ECCO allows variable that are strongly negatively correlated the opportunity to cluster together. Further, we match the linkage functions to an optimization metrics that emulates the linkage functions. For example, the Pseudo F-statistic (also known as Calinski-Harabasz [73], Eq. (5)) matches well with the sum-of-squares based Ward linkage function. ECCO improves upon single clustering solutions by combining multiple

clustering solutions and ensuring that each clustering solution included is “optimal”. Finally, by validating the co-occurrence matrix generated through ensemble clustering we obtain data objects which co-cluster consistently.

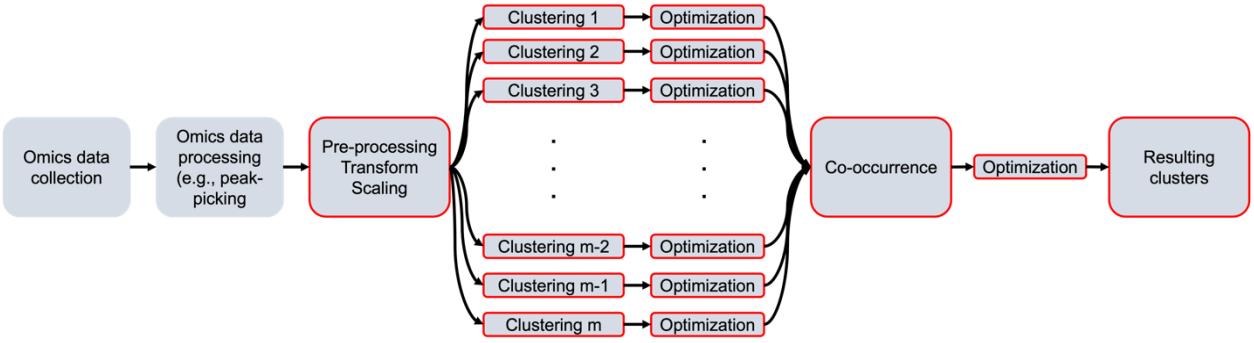

Figure 7.4 Flowchart from omics data collection to identification of clusters. From left to right, omics data is collected (e.g., liquid chromatography mass-spectrometry), processed (e.g., peak picking mass-spectrometry results (XCMS [124]), then input to ECCO for analysis. ECCO starts by pre-processing that data (i.e., transforming and/or scaling the data), clustering the data using m sets of hyperparameters and 2-K clusters, the solutions are then fed into optimization algorithms to determine the optimal clustering solutions for each m clustering, the best m clustering solutions are then combined into a co-occurrence matrix, after which a final optimization is performed to determine the “optimal” cluster identified by the ensemble from which we get resulting clusters of the -omic data of interest. All boxes outlined in red are available in the ECCO UI.

7.3.5: Implementation

ECCO is fully implemented into a graphical user interface (UI) written in Python 3 that is compatible with all major operating systems. All code is publicly available on Github (https://github.com/hisl6802/ECCO). The UI and its dependencies can be installed by following the instructions in the README file. Full documentation of ECCO and additional functionalities can be found on the wiki pages (https://github.com/hisl6802/ECCO/wiki).

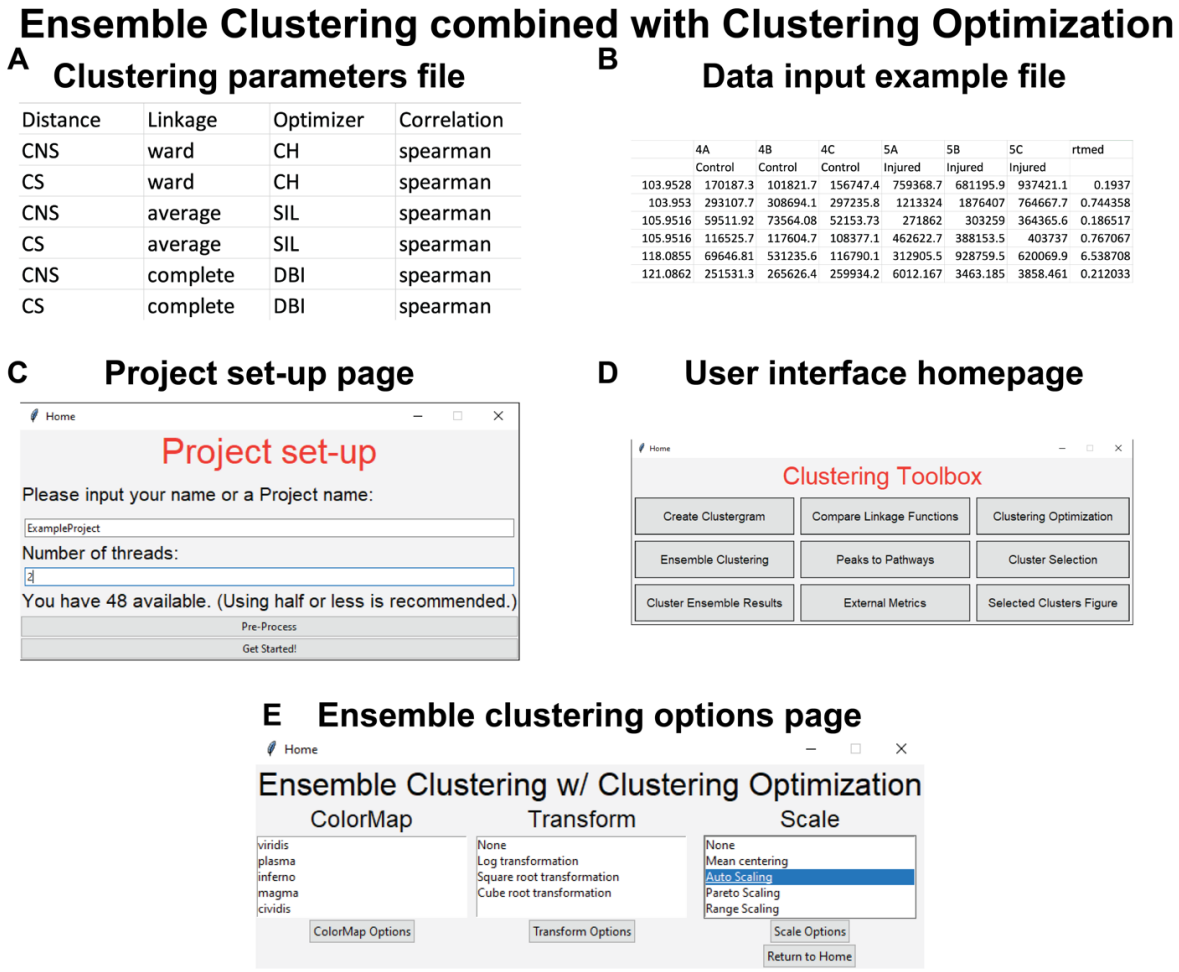

Figure 7.5 Performing ensemble clustering combined with clustering optimization using the user interface. A) Example clustering parameters input file; B) top 6 rows of an example for submission to be clustered; C) Project set-up page allowing users to name log files and utilize multi-threading; D) Homepage of the UI containing all of the available features in UI; E) Options for color-map, and pre-processing of data prior to clustering.

To perform an ensemble clustering combined with clustering optimization analysis users simply need to input the clustering parameters, and the data they want to cluster (**Figure 7.5**). The user can specify the dissimilarity/distance class (*i.e.*, correlation-based, or distance based), linkage function, optimization function, and the distance/dissimilarity measure (*e.g.*, Spearman correlation coefficient or Euclidean distance) (**Figure 7.5A**). The user can also specify a group for each data column and provide additional identifying information in the first and last columns

of the datasheet (**Figure 7.5B**). After preparing the clustering parameters file, and the input data file the user can start the UI. Upon starting the UI, the user is prompted to select the directory where all output files will be saved, immediately followed by an interface to specify the project name and the number of threads to use (**Figure 7.5C**). Finally, the user will be taken to the homepage (**Figure 7.5D**) where they can select the "Ensemble Clustering" button and select the color-map, and pre-processing steps of interest (**Figure 7.5E**).

The ECCO functionality generates multiple outputs for evaluating, visualizing and post-processing the resulting clusters. To evaluate the performance of clustering solutions, we provide three images comparing clustering solutions using the Rand-index and the adjusted Rand-index (see case studies 1 and 2). The Rand-index [145] is the proportion two clustering solutions agree on the clusters data objects belong in, whereas the adjusted Rand-index [146] accounts for random chance. Further, we provide two visuals of the clusters determined by ECCO: a clustergram of the co-occurrence matrix and a second clustergram of the co-occurrence clustering on the original data. Furthermore, we provide the co-occurrence matrix, and automatically generate excel files of the resulting clusters identified through ECCO. By utilizing the ECCO UI the user can determine the need for an ensemble clustering on their data, visualize the ensemble results, and post-process the resulting clusters rapidly and repeatability.

The ECCO UI also offers a wide variety of functionalities to pre-process, post-process, and perform other clustering analyses of interest. Furthermore, the UI enables rapid development of novel ensembles through codeless integration, and scalability. In the sections below we briefly discuss the selection of pre-processing steps, clustering parameters, and how the co-occurrence matrix is analyzed. After which we provide two case studies that describe how to use

ECCO. Additional information on the functionalities can be found on the UI wiki pages (https://github.com/hisl6802/ECCO/wiki).

7.3.5.1: Preprocessing Data. Preprocessing data is a critical step in the workflow for clustering analysis and should be given significant consideration before using any of the tools presented here. Transformation and scaling of data directly impact the clustering solution; thus, users should consider testing multiple combinations. For simplicity, we focus on the log-base 10 transformation combined with auto-scaling (z-scores) as these are standard to metabolomics analysis[11, 13, 31, 32, 37, 39, 117].

7.3.5.2: Ensemble Clustering Options. The ECCO UI provides users with an easy-to-use interface for generating clustering ensembles. Users can specify any distance/dissimilarity measure in the scipy library (pdist) [147], as well as the two correlation-based dissimilarity measures proposed in this work (See Eq(s) 1 and 2). Furthermore, the user can specify the linkage function, and optimization function allowing for solution-by-solution optimization. In this current implementation, we offer four linkage functions (complete, average, and Ward), and three optimization metrics (Silhouette, Davies-Bouldin index, and Pseudo F-statistic).

7.5.3.3: Analyzing the Co-Occurrence Matrix. Ensemble clustering generates a co-occurrence matrix that is clustered to determine the data objects that consistently co-cluster. To determine the co-clustering data objects a broad range of clustering approaches have been used, including agglomerative hierarchical clustering with Euclidean distance [72], hypergraph partitioning [148], and fuzzy c-means (a Euclidean based clustering) [72, 149]. However, hypergraph partitioning is complicated and difficult to interpret, and the centroids of fuzzy c-means clusters tend to converge to the data center with high-dimensionality[149]. Thus, the

ECCO UI focuses on the agglomerative hierarchical clustering with Euclidean distance, and agglomerative hierarchical clustering using 1 – co-occurrence matrix. Furthermore, the ECCO UI optimizes the clustering of the co-occurrence clustering for 2-10 clusters using the Silhouette score. Finally, users can post-process the identified clusters to determine the meaning of the identified group. For example, in untargeted metabolomics studies the identified clusters can be submitted to Peaks-to-Pathways to generate files for submission to mummichog for pathways identification [71].

7.4 Results

ECCO improves cluster identification by combining the optimal clustering solutions for each clustering solution into an ensemble. In the examples below we demonstrate how to perform ECCO while also motivating the utility of this approach as opposed to a single clustering solution. Furthermore, we provide users with Jupyter Notebooks [150] of each of the case studies outlined below allowing for direct reproduction of these analyses. The ensemble of size 6 is applied in both case studies to allow for the usage of three linkage functions in combined with two dissimilarity measures.

7.4.1: Case Studies

To demonstrate the application of ECCO we perform a 6-cluster solution ensemble (**Table 7.1**). Within this ensemble we utilize two correlation-based dissimilarity measures that allow variables with negative correlations to cluster with those having positive correlations rather than being penalized more than uncorrelated variables (**Figure 7.2**). We analyze two separate datasets from previous studies [32, 39], comparing the individual AHC solutions against each

other. We then show how the AHC solutions compare to the resulting ensemble clustering solution. Finally, we show the resulting clusters identified by ECCO. Using the resulting clusters researchers can derive insights. For example, in untargeted metabolomics we submit the identified clusters to mummichog for identification of biological pathways.

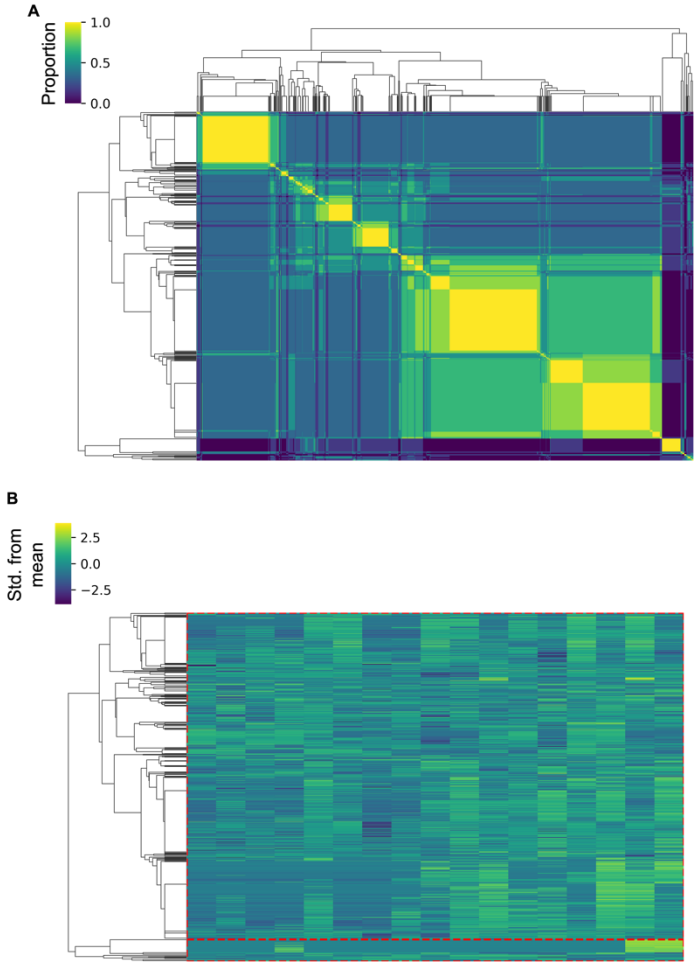

Figure 7.6 Ensemble clustering results A) Clustering of the co-occurrence matrix B) Red dashed boxes indicating the optimal clusters identified through ensemble clustering.

7.4.1.1 Case Study 1: Analysis of Late OA Metabolomic Profiles: Synovial fluid was collected post-mortem from n=75 patients, with concurrent radiographic scoring of osteoarthritis [32] (OA) (Outerbridge scoring system) [151, 152]. Metabolites were extracted using an

established protocol [32, 153], analyzed using liquid chromatography mass spectrometry (LC-MS) and the results were processed using XCMS [124]. 9962 metabolite features were detected, and a total of 1362 were analyzed after removing metabolites with a median intensity of zero in each group [32]. For analysis, samples were split into no OA, early OA, and late OA groups. In this case study we focus on the late OA metabolic profiles.

To demonstrate that different combinations of clustering algorithms and dissimilarity measures lead to different clustering solutions we used the Rand-index [145], and the adjusted Rand-index [146]. The rand-index gives a proportional measure between 0 and 1 for how similar two clustering solutions are, with 1 being a perfect match. Whereas the adjusted rand gives a score between -1 and 1, with values less than zero being worse than random chance (*i.e.*, if labels were randomly assigned to data objects), and 1 is perfect matching between clustering solutions. When comparing optimal clustering solutions, we found Rand-index values from 0.28 – 0.93, suggesting anywhere from 28-93% match between the different clustering solutions. Next, comparing the solutions using the adjusted Rand-index suggests that the Complete and Ward linkage agreed as much as randomly assigning data objects to clusters. By contrast, the Average linkage produced similar clusters for both dissimilarity measures. Finally, we compared the optimal clustering solutions for each mono-clustering to the clusters identified through ECCO. Interestingly, the clusters identified using the Complete linkage function closely resembled those identified by the ensemble clustering algorithm. Thus, mono-clustering solutions cluster members could vary by 4 – 75%, demonstrating the need for an ensemble to improve repeatability in cluster selection.

To interpret the ensemble clustering solution, we provide two clustergrams, one of the co-occurrence matrices, and the other displaying the optimally identified clusters on the original data (**Figure 7.6A-B**). In Figure 6D we show the clustering of the co-occurrence matrix (Figure 6D) shows the groups of metabolites that clustered together in 100% of the mono-clustering solutions with yellow "squares". Using the clustering from the co-occurrence and the optimal number of clusters identified, ECCO provides red-dashed rectangles identify the optimal clusters for the ensemble solution (**Figure 7.6B**). The two red-dashed clusters in this case study are automatically extracted for post-processing.

7.4.1.2 Case Study 2: Analysis of the Similarities in Synovial Fluid Metabolic Responses Following Traumatic Injuries. One knee of C57BL/6 mice was subjected to non-invasive overload injury, and the synovial fluid from the knee joints was gathered 7 days post-injury [39]. Metabolites were extracted using an established protocol, and were analyzed using LC-MS. The results were analyzed using XCMS. 3397 metabolites were considered detected, and comparisons were made between all groups, sham-injured v. injured v. contralateral-to-injured, sham-injured v. injured, and contralateral-to-injured v. injured [39]. For simplicity in this case study, we focus on the comparison of sham-injured to injured synovial fluid metabolic profiles. Previously these data were analyzed using an ensemble of size 13, we will apply an ensemble of size 6 here.

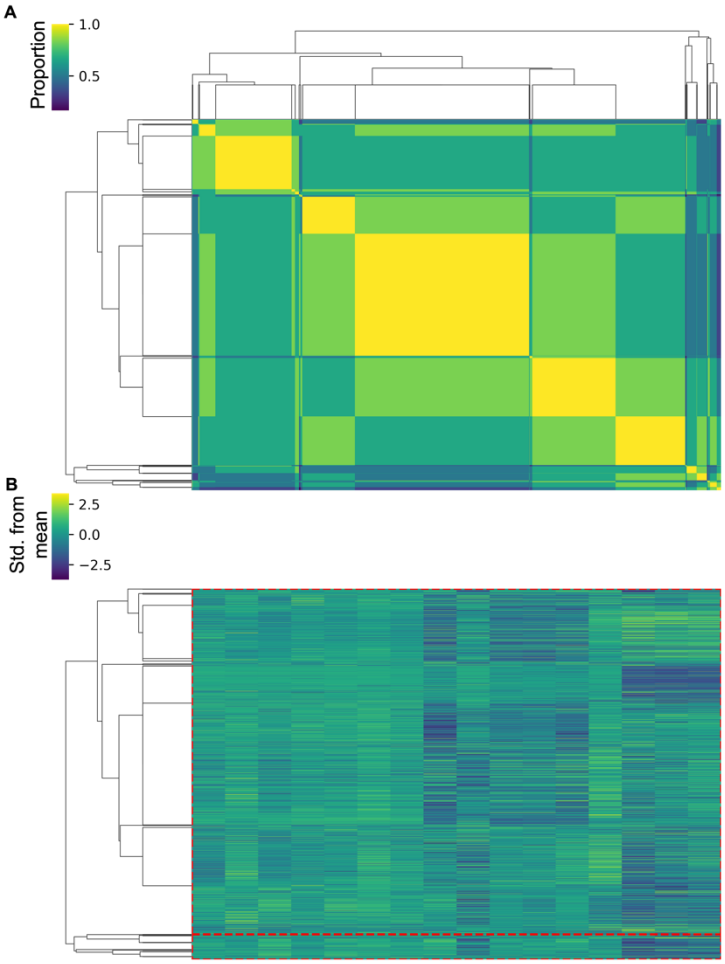

Figure 7.7 Ensemble Clustering D) Clustergram of co-occurrence. E) Clusters from co-occurrence clustering applied to original data, red rectangles represent the two identified clusters.

Like case study 1, clustering solutions showed a broad range of similarities. The Rand-index comparison varied from 0.37 to 0.97, whereas the adjusted Rand-index showed between -0.02 and 0.16, suggesting that the clustering solutions did not agree well. Finally, we found that the complete linkage function captures similar clusters as the ensemble with >.85 agreement. However, upon closer inspection we can see that four of the six also perform worse than random chance, suggesting that even when the match-up is large the performance can still be poor. Finally, when considering the clusters identified using ECCO we again found that 2 clusters was

optimal for our given data. Visualization of these data show, the identified clusters using ECCO (**Figure 7.7A-B**).

7.5 Discussion

The ECCO UI was designed to provide easy-to-use clustering optimization, and clustering ensembles toward improve group detection in high dimensional omics data. Currently in untargeted metabolomics studies researchers tend to rely on MetaboAnalyst [154] to cluster their data. By using MetaboAnalyst researchers are limited to mono-clustering solutions that are not optimized, which reduces repeatability of analyses. The ECCO UI was constructed to improve repeatability and the ease of optimizing and generating clustering ensembles as a novel workflow for omics researchers.

An ideal usage of ECCO is in the identification of metabolic and patient endotypes from high-throughput biological data. As seen in both cases studies, when comparing mono-clustering solutions the identified clusters can vary greatly with <.3 agreement. In an untargeted metabolomics study this would imply that the selection of one mono-clustering solution over another could lead to drastically different biological insights. By contrast, the AHC with complete linkage function against the resulting ensemble clustering solution showed >.9 agreement in both case studies. These results suggest that the AHC with complete linkage identifies similar clusters as the ensemble clustering solution in these studies. Thus, this by comparing the mono-clustering solutions to the resulting ensemble researchers can determine if the more complex clustering is necessary. However, without running these quantitative comparisons, and ECCO researchers would be unable to ensure a repeatable clustering analysis.

Therefore, to ensure repeatable clustering in omics, researchers should be performing a workflow as demonstrated in these case studies.

Although the ECCO UI is designed for ensemble clustering combined with clustering optimization, the UI provides other tools for evaluation of clustering results. The ECCO UI contains 8 distinct functionalities aimed at streamlining clustering of untargeted metabolomics data. Users can generate mono-agglomerative hierarchical clustering solutions and evaluate different mono-clustering solutions. Further, the users can optimize mono-clustering solutions. The optimization of mono-clustering solutions is considered a minimum step toward improving endotype identification [72]. The ECCO UI also provides tools for the users to select clusters and generate a figure of the selected clusters. The users can also generate input files for pathway analysis on the identified clusters. Each of the functionalities above provide ECCO UI users tools that ease the burden of high-throughput biological data analysis.

The ECCO UI is specifically designed for agglomerative hierarchical clustering and does not incorporate other clustering methods. We acknowledge that other clustering methods can be incorporated into ensembles but chose to focus on agglomerative methods given their prevalence in untargeted metabolomics studies and simple interpretation. Further, the ECCO UI includes both the scipy and sklearn packages [147, 155], allowing users to easy expand the UI to incorporate other clustering methods. Pre-processing is a crucial step in clustering analysis, and the ECCO UI includes methods common to omics analysis [154]. However, these pre-processing tools do not encompass all possible pre-processing steps. Clustering ensembles can vary in size, clustering methods, and combination of parameters. Here we have described an ensemble

clustering combined with clustering optimization that tries to match the linkage method to the optimizer, however, many other combinations are possible and can be explored.

The main motivation for developing the ECCO UI was to implement improved clustering methods towards identifying metabolic endotypes. Clustering ensembles should be utilized to ensure repeatable clustering results and mitigate the pitfalls of clustering high-throughput biological data. By providing a framework for performing ensemble clustering we hope to encourage the usage of these clustering methodologies toward improving analysis of high dimensional omics data.

7.6 Acknowledgements

This study was funded in part by grants from the NSF (CMMI 2140127) and NIH (NIAMS R01AR073964 and R01AR081489). We would like to thank Hope Welhaven, Erik P. Myers, Avery Welfley, and Kenna Brown for helping identify bugs in ECCO during development.

CHAPTER EIGHT

CONCLUSION AND FUTURE DIRECTIONS

Conclusions

In these studies, we provided novel data on the impact of cyclic compression on fluid movement from subchondral bone into articular cartilage (**Figure 8.1**). More specifically we found that fluid movement within the osteochondral unit (**Figure 8.1**) is driven by fluid pressure gradients across the tidemark (**Figure 8.1**), and that increased fluid movement occurs with cyclic compression. Furthermore, in modeling early OA we predicted an increase in osteochondral fluid transport. The implications of osteochondral fluid transport in health include potential transfer of key nutrients and signals from bone-to-cartilage or vice versa. By contrast, changes to cartilage and bone material properties that lead to increased osteochondral fluid transport, will likely lead to the exposure of chondrocytes to cytokines and proteases from bone [28, 29]. Thus, changes in osteochondral fluid transport could lead to the onset, and progression of OA. By establishing the impact of cyclic compression on osteochondral fluid transport in health and disease we have provided critical towards understanding OA as a whole joint disease.

Future Directions

In these studies, we provide critical data on the overarching gap in knowledge surrounding osteochondral fluid transport in health and disease and its impacts on joint health. However, many critical gaps remain in our understanding of osteochondral fluid transport's role in the progression, and onset of OA. To continue our efforts to understand OA, and discover novel treatments, and cures we suggest the following expansions of each study presented here.

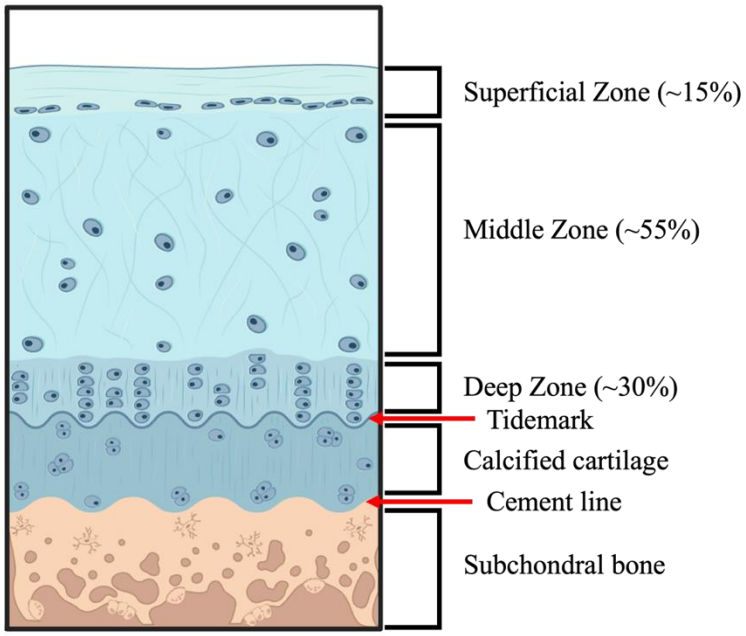

Figure 8.1. Osteochondral unit showing the zones of articular cartilage, tidemark, calcified cartilage, cement line and subchondral bone.

In chapter 3, we established that fluid pressure gradients develop at the osteochondral interface and diminished during stress relaxation. To expand the understanding of the mechanics driving fluid transport between cartilage and bone several remaining critical gaps need to be addressed including 1) does unloading cartilage lead to fluid pressure gradients from bone-to-cartilage? 2) does loading magnitude impact fluid pressure gradients at the osteochondral interface? 3) how do fluid pressure gradients under creep experiments differ from stress-relaxation experiments? Initially, future models should look to update the material models of Pierce et al. [2] that accounts for the collagen fibers and their orientation, the proteoglycan matrix, and incorporates the collagen fiber orientation into the permeability providing significant improvements in model performance. Upon improvement of the material models future work should aim to understand the fluid pressure gradients at the osteochondral interface upon unloading, which would provide predictions of bone-to-cartilage fluid transport. Joint loads vary

in magnitude and time of application and will likely directly impact osteochondral fluid transport. Future studies should consider the impacts of load magnitude on fluid pressure gradients, and the impact of the time of application through creep experiments. Through these future studies and the study presented in chapter 3 we can established how fluid pressure gradients that drive osteochondral fluid transport vary in health and disease.

Subchondral bone loses volume, and increases in stiffness, and the synovial fluid metabolism shifts rapidly after joint injury in mice. In chapter 4, we expanded on previous studies of PTOA by establishing that synovial fluid metabolism shifts within 7 days of joint injuries and may impact the contralateral-to-injured limb. Further, we found a strong trend towards increased subchondral bone modulus. However, several critical gaps in our understanding of early joint changes following traumatic injuries remain including 1) does synovial fluid metabolism return to the baseline or continue to diverge with time after injury? 2) does joint mechanics restoration (i.e., ACL reconstruction) restore synovial fluid metabolism to baseline? 3) does age and sex impact subchondral bone changes and synovial fluid metabolic responses after traumatic injuries? and Synovial fluid metabolism is a strong indicator of joint health, thus, understanding how its metabolism responds as the joint progresses towards end-stage PTOA is crucial. Thus, future studies should consider more time points after injury to establish metabolic endotypes of disease progression. Furthermore, future studies should model the effects of ACL reconstruction on synovial fluid metabolism to understand whether restoration of joint mechanics returns metabolism to baseline. Many previous studies have considered a single sex and a single age group, limiting the interpretation of their results. Future studies should explore the effects of age, and sex on subchondral bone, and synovial fluid metabolism

after traumatic injuries. A broad range of studies beyond those in chapter 4 and the future studies outlined here are needed to understand why PTOA progresses rapidly.

In chapter 5, we provided novel evidence of bone-to-cartilage fluid transport during cyclic compression. These results suggest that 5 % mean strain enhanced fluid transport from bone-to-cartilage in healthy bovine osteochondral cores. Given the novelty of these findings many future studies are needed to address critical gaps including 1) do large physiologically relevant molecules transport from bone-to-cartilage? 2) do load magnitudes impact osteochondral fluid transport? 3) how does the time of loading impact osteochondral fluid transport? Recent studies including that of chapter 5 showed that small molecules diffuse, and cyclic compression enhances fluid transport from bone-to-cartilage. Future studies should investigate a broader range of physiologically relevant molecules (e.g., insulin) to understand the molecules that could be shared between bone and cartilage. In the studies of chapter 5, we utilized two stain conditions, future studies should consider how load magnitude and the time the loads are applied. By establishing the molecules that can move between bone and cartilage, and how load magnitude and time of application influences osteochondral fluid transport we can further our understanding of fluid transport in health.

In chapter 6, we developed a novel model to understand the differences between osteochondral fluid transport in health and disease. Through this model we predicted an increase in osteochondral fluid transport in early OA. To expand upon the understandings gained through this model future studies should look to address the following critical gaps 1) does osmotic swelling impact osteochondral fluid transport? 2) do specific injures or stages of OA impact osteochondral fluid transport? 3) does fully unloading the joint lead to bone-to-cartilage fluid

transport? Osmotic swelling caused by the charged proteoglycan matrix is a critical player in joint mechanics not accounted for in the model of chapter 6. Thus, future studies should incorporate osmotic swelling to understand its impact on osteochondral fluid transport, particularly with loss of proteoglycans in the progression towards OA. A broad range of factors can lead to the onset of OA; thus, future studies should also explore the different OA models and investigate the impacts of other model parameter changes on osteochondral fluid transport. The strain regime in these studies did not fully unload the sample each time, which could lead to underestimation of osteochondral fluid transport. Therefore, future studies should consider fully unloading the sample in each compression cycle to understand how that impacts osteochondral fluid transport. By addressing these critical gaps, we can better understand the mechanics of osteochondral fluid transport, potentially implicating this mechanism in OA progression.

The future studies suggested above aim to create a holistic view of osteochondral fluid transport towards understanding OA as a whole joint disease. Expansions of studies in chapters 3, 5, and 6 aim to understand the mechanics of osteochondral fluid transport and establish the molecules that can transport from bone-to-cartilage or vice versa. Whereas expansion of the studies in chapter 4 aim to understand how synovial fluid can be used to detect joint changes and how subchondral bone a key player osteochondral fluid mechanics is impact by traumatic injuries. Through these future studies and the studies in this work we can become one step closer to understanding OA as a whole joint disease and identifying treatments and cures for this degenerative disease.

CUMULATIVE REFERENCES CITED

1. Forster, H. and J. Fisher, *The influence of loading time and lubricant on the friction of articular cartilage.* Proc Inst Mech Eng H, 1996. **210**(2): p. 109-19.

2. Pierce, D.M., et al., *A microstructurally based continuum model of cartilage viscoelasticity and permeability incorporating measured statistical fiber orientations.* Biomech Model Mechanobiol, 2016. **15**(1): p. 229-44.

3. Wang, X., et al., *On incorporating osmotic prestretch/prestress in image-driven finite element simulations of cartilage.* J Mech Behav Biomed Mater, 2018. **86**: p. 409-422.

4. Mow, V.C., *Basic Orthopaedic Biomechanics & Mechano-biology*. 2005.

5. Setton, L.A., H. Tohyama, and V.C. Mow, *Swelling and curling behaviors of articular cartilage.* J Biomech Eng, 1998. **120**(3): p. 355-61.

6. Dudhia, J., *Aggrecan, aging and assembly in articular cartilage.* Cell Mol Life Sci, 2005. **62**(19-20): p. 2241-56.

7. Pierce, D.M., T. Ricken, and G.A. Holzapfel, *Modeling sample/patient-specific structural and diffusional responses of cartilage using DT-MRI.* Int J Numer Method Biomed Eng, 2013. **29**(8): p. 807-21.

8. Filidoro, L., et al., *High-resolution diffusion tensor imaging of human patellar cartilage: feasibility and preliminary findings.* Magn Reson Med, 2005. **53**(5): p. 993-8.

9. Korhonen, R.K., et al., *Importance of collagen orientation and depth-dependent fixed charge densities of cartilage on mechanical behavior of chondrocytes.* J Biomech Eng, 2008. **130**(2): p. 021003.

10. O'Hara, B.P., J.P. Urban, and A. Maroudas, *Influence of cyclic loading on the nutrition of articular cartilage.* Ann Rheum Dis, 1990. **49**(7): p. 536-9.

11. McCutchen, C.N., D.L. Zignego, and R.K. June, *Metabolic responses induced by compression of chondrocytes in variable-stiffness microenvironments.* J Biomech, 2017. **64**: p. 49-58.

12. Sah, R.L., et al., *Biosynthetic response of cartilage explants to dynamic compression.* J Orthop Res, 1989. **7**(5): p. 619-36.

13. Zignego, D.L., J.K. Hilmer, and R.K. June, *Mechanotransduction in primary human osteoarthritic chondrocytes is mediated by metabolism of energy, lipids, and amino acids.* J Biomech, 2015. **48**(16): p. 4253-61.

14. Guilak, F., et al., *The pericellular matrix as a transducer of biomechanical and biochemical signals in articular cartilage.* Ann N Y Acad Sci, 2006. **1068**: p. 498-512.

15. Oliveira Silva, M., et al., *Molecular Signaling Interactions and Transport at the Osteochondral Interface: A Review.* Front Cell Dev Biol, 2020. **8**: p. 750.

16. Arkill, K.P. and C.P. Winlove, *Solute transport in the deep and calcified zones of articular cartilage.* Osteoarthritis Cartilage, 2008. **16**(6): p. 708-14.

17. Campbell, S.E., V.L. Ferguson, and D.C. Hurley, *Nanomechanical mapping of the osteochondral interface with contact resonance force microscopy and nanoindentation.* Acta Biomaterialia, 2012. **8**: p. 8.

18. Di Luca, A., C. Van Blitterswijk, and L. Moroni, *The osteochondral interface as a gradient tissue: from development to the fabrication of gradient scaffolds for regenerative medicine.* Birth Defects Res C Embryo Today, 2015. **105**(1): p. 34-52.

19. Pan, J., et al., *Elevated cross-talk between subchondral bone and cartilage in osteoarthritic joints.* Bone, 2012. **51**(2): p. 212-7.

20. Pan, J., et al., *In situ measurement of transport between subchondral bone and articular cartilage.* J Orthop Res, 2009. **27**(10): p. 1347-52.

21. Lyons, T.J., et al., *The normal human chondro-osseous junctional region: evidence for contact of uncalcified cartilage with subchondral bone and marrow spaces.* BMC Musculoskelet Disord, 2006. **7**: p. 52.

22. Pouran, B., et al., *Solute transport at the interface of cartilage and subchondral bone plate: Effect of micro-architecture.* J Biomech, 2017. **52**: p. 148-154.

23. Olah, T. and H. Madry, *The Osteochondral Unit: The Importance of the Underlying Subchondral Bone.* Cartilage Restoration, 2018: p. 6.

24. Chen, H., T. Senda, and K.Y. Kubo, *The osteocyte plays multiple roles in bone remodeling and mineral homeostasis.* Med Mol Morphol, 2015. **48**(2): p. 61-8.

25. Lewis, K.J., et al., *Osteocyte calcium signals encode strain magnitude and loading frequency in vivo.* Proc Natl Acad Sci U S A, 2017. **114**(44): p. 11775-11780.

26. Vahidi, G., et al., *Lacunar-canalicular bone remodeling: Impacts on bone quality and tools for assessment.* Bone, 2021. **143**: p. 115663.

27. Filipowska, J., et al., *The role of vasculature in bone development, regeneration and proper systemic functioning.* Angiogenesis, 2017. **20**(3): p. 291-302.

28. Westacott, C.I., et al., *Alteration of cartilage metabolism by cells from osteoarthritic bone.* Arthritis Rheum, 1997. **40**(7): p. 1282-91.

29. Yuan, X.L., et al., *Bone-cartilage interface crosstalk in osteoarthritis: potential pathways and future therapeutic strategies.* Osteoarthritis Cartilage, 2014. **22**(8): p. 1077-89.

30. Alliston, T., *Biological regulation of bone quality.* Curr Osteoporos Rep, 2014. **12**(3): p. 366-75.

31. Carlson, A.K., et al., *Application of global metabolomic profiling of synovial fluid for osteoarthritis biomarkers.* Biochem Biophys Res Commun, 2018. **499**(2): p. 182-188.

32. Carlson, A.K., et al., *Characterization of synovial fluid metabolomic phenotypes of cartilage morphological changes associated with osteoarthritis.* Osteoarthritis Cartilage, 2019. **27**(8): p. 1174-1184.

33. Chery, D.R., et al., *Early changes in cartilage pericellular matrix micromechanobiology portend the onset of post-traumatic osteoarthritis.* Acta Biomater, 2020. **111**: p. 267-278.

34. Christiansen, B.A., et al., *Musculoskeletal changes following non-invasive knee injury using a novel mouse model of post-traumatic osteoarthritis.* Osteoarthritis Cartilage, 2012. **20**(7): p. 773-82.

35. Christiansen, B.A., et al., *Trabecular bone loss at a distant skeletal site following noninvasive knee injury in mice.* J Biomech Eng, 2015. **137**(1): p. 0110051-6.

36. Fang, H., et al., *Early Changes of Articular Cartilage and Subchondral Bone in The DMM Mouse Model of Osteoarthritis.* Sci Rep, 2018. **8**(1): p. 2855.

37. Hahn, A.K., et al., *The microbiome mediates epiphyseal bone loss and metabolomic changes after acute joint trauma in mice.* Osteoarthritis Cartilage, 2021. **29**(6): p. 882-893.

38. Haudenschild, D.R., et al., *Inhibition of early response genes prevents changes in global joint metabolomic profiles in mouse post-traumatic osteoarthritis.* Osteoarthritis and Cartilage, 2019. **27**(3): p. 504-512.

39. Hislop, B.D., et al., *Subchondral bone structure and synovial fluid metabolism are altered in injured and contralateral limbs 7 days after non-invasive joint injury in skeletally-mature C57BL/6 mice.* Osteoarthritis Cartilage, 2022. **30**(12): p. 1593-1605.

40. Hsia, A.W., et al., *Post-traumatic osteoarthritis progression is diminished by early mechanical unloading and anti-inflammatory treatment in mice.* Osteoarthritis Cartilage, 2021. **29**(12): p. 1709-1719.

41. Lories, R.J. and F.P. Luyten, *The bone-cartilage unit in osteoarthritis.* Nat Rev Rheumatol, 2011. **7**(1): p. 43-9.

42. Maerz, T., et al., *Traumatic joint injury induces acute catabolic bone turnover concurrent with articular cartilage damage in a rat model of posttraumatic osteoarthritis.* Journal of Orthopaedic Research, 2021. **39**(9): p. 1965-1976.

43. Martin, J.A. and J.A. Buckwalter, *Aging, articular cartilage chondrocyte senescence and osteoarthritis.* Biogerontology, 2002. **3**(5): p. 257-64.

44. Anderson, M.J., et al., *Contribution of mechanical unloading to trabecular bone loss following non-invasive knee injury in mice.* J Orthop Res, 2016. **34**(10): p. 1680-1687.

45. Das Neves Borges, P., T.L. Vincent, and M. Marenzana, *Automated assessment of bone changes in cross-sectional micro-CT studies of murine experimental osteoarthritis.* PLoS One, 2017. **12**(3): p. e0174294.

46. McCulloch, K., et al., *Accelerated post traumatic osteoarthritis in a dual injury murine model.* Osteoarthritis Cartilage, 2019. **27**(12): p. 1800-1810.

47. Burr, D.B. and M.A. Gallant, *Bone remodelling in osteoarthritis.* Nat Rev Rheumatol, 2012. **8**(11): p. 665-73.

48. Behets, C., et al., *Effects of calcitonin on subchondral trabecular bone changes and on osteoarthritic cartilage lesions after acute anterior cruciate ligament deficiency.* J Bone Miner Res, 2004. **19**(11): p. 1821-6.

49. Long, H., et al., *Prevalence Trends of Site-Specific Osteoarthritis From 1990 to 2019: Findings From the Global Burden of Disease Study 2019.* Arthritis Rheumatol, 2022. **74**(7): p. 1172-1183.

50. Leifer, V.P., J.N. Katz, and E. Losina, *The burden of OA-health services and economics.* Osteoarthritis Cartilage, 2022. **30**(1): p. 10-16.

51. Dantas, L.O., T.F. Salvini, and T.E. McAlindon, *Knee osteoarthritis: key treatments and implications for physical therapy.* Braz J Phys Ther, 2021. **25**(2): p. 135-146.

52. Goldring, S.R. and M.B. Goldring, *Changes in the osteochondral unit during osteoarthritis: structure, function and cartilage-bone crosstalk.* Nat Rev Rheumatol, 2016. **12**(11): p. 632-644.

53. Ding, C., et al., *Knee cartilage defects: association with early radiographic osteoarthritis, decreased cartilage volume, increased joint surface area and type II collagen breakdown.* Osteoarthritis Cartilage, 2005. **13**(3): p. 198-205.

54. Findlay, D.M. and J.S. Kuliwaba, *Bone-cartilage crosstalk: a conversation for understanding osteoarthritis.* Bone Res, 2016. **4**: p. 16028.

55. Hwang, J., et al., *Increased hydraulic conductance of human articular cartilage and subchondral bone plate with progression of osteoarthritis.* Arthritis Rheum, 2008. **58**(12): p. 3831-42.

56. Burr, D.B. and E.L. Radin, *Microfractures and microcracks in subchondral bone: are they relevant to osteoarthrosis?* Rheum Dis Clin North Am, 2003. **29**(4): p. 675-85.

57. Muir, P., et al., *Role of endochondral ossification of articular cartilage and functional adaptation of the subchondral plate in the development of fatigue microcracking of joints.* Bone, 2006. **38**(3): p. 342-9.

58. Thomas, A.C., et al., *Epidemiology of Posttraumatic Osteoarthritis.* J Athl Train, 2017. **52**(6): p. 491-496.

59. Messent, E.A., et al., *Osteophytes, juxta-articular radiolucencies and cancellous bone changes in the proximal tibia of patients with knee osteoarthritis.* Osteoarthritis Cartilage, 2007. **15**(2): p. 179-86.

60. Chubinskaya, S., et al., *Articular Cartilage Injury and Potential Remedies.* J Orthop Trauma, 2015. **29 Suppl 12**(Suppl 12): p. S47-52.

61. Ayala, S., et al., *Cartilage articulation exacerbates chondrocyte damage and death after impact injury.* J Orthop Res, 2021. **39**(10): p. 2130-2140.

62. Fish, J. and T. Belytschko, *A First Course in Finite Elements*. 2008.

63. Hislop, B.D., C.M. Heveran, and R.K. June, *Development and analytical validation of a finite element model of fluid transport through osteochondral tissue.* J Biomech, 2021. **123**: p. 110497.

64. Stender, M.E., R.A. Regueiro, and V.L. Ferguson, *A poroelastic finite element model of the bone-cartilage unit to determine the effects of changes in permeability with osteoarthritis.* Comput Methods Biomech Biomed Engin, 2017. **20**(3): p. 319-331.

65. Kim, S., et al., *Global metabolite profiling of synovial fluid for the specific diagnosis of rheumatoid arthritis from other inflammatory arthritis.* PLoS One, 2014. **9**(6): p. e97501.

66. Wegner, A.M., et al., *Acute Changes in NADPH Oxidase 4 in Early Post-Traumatic Osteoarthritis.* J Orthop Res, 2019. **37**(11): p. 2429-2436.

67. Yik, J.H., et al., *Early transient induction of IL-6 in a mouse joint injury model.* Osteoarthritis Cartilage, 2013. **21**: p. 2.

68. Zheng, L., et al., *The role of metabolism in chondrocyte dysfunction and the progression of osteoarthritis.* Ageing Res Rev, 2021. **66**: p. 101249.

69. Stagljar, I., *The power of OMICs.* Biochem Biophys Res Commun, 2016. **479**(4): p. 607-609.

70. Roux, M.A., *A Comparative study of Divisive and Agglomerative Hierarchical Clustering Algorithms.* Journal of Classification, 2018. **35**: p. 22.

71. Li, S., et al., *Predicting network activity from high throughput metabolomics.* PLoS Comput Biol, 2013. **9**(7): p. e1003123.

72. Ronan, T., Z.J. Qi, and K.M. Naegle, *Avoiding common pitfalls when clustering biological data.* Science Signaling, 2016. **9**(432).

73. Caliński, T. and J. Harabasz, *A dendrite method for cluster analysis.* Communications in Statistics - Theory and Methods, 1974. **3**: p. 27.

74. Davies, D.L. and D.W. Bouldin, *A cluster separation measure.* IEEE Trans. Pattern Analysis Machine Intelligence, 1979. **2**: p. 4.

75. Rousseeuw, P.J., *Silhouettes - a Graphical Aid to the Interpretation and Validation of Cluster-Analysis.* Journal of Computational and Applied Mathematics, 1987. **20**: p. 53-65.

76. Starczewski, A., *A new validity index for crisp clusters.* Pattern Analysis and Applications, 2017. **20**(3): p. 687-700.

77. Pakhira, M.K., S. Bandyopadhyay, and U. Maulik, *Validity index for crisp and fuzzy clusters.* Pattern Recognition, 2004. **32**: p. 15.

78. Mwangi, T.K., et al., *Intra-articular clearance of labeled dextrans from naive and arthritic rat knee joints.* J Control Release, 2018. **283**: p. 76-83.

79. Chegini, S. and S.J. Ferguson, *Time and depth dependent Poisson's ratio of cartilage explained by an inhomogeneous orthotropic fiber embedded biphasic model.* J Biomech, 2010. **43**(9): p. 1660-6.

80. Guo, H., S.A. Maher, and P.A. Torzilli, *A biphasic finite element study on the role of the articular cartilage superficial zone in confined compression.* J Biomech, 2015. **48**(1): p. 166-70.

81. Ateshian, G.A., *Anisotropy of fibrous tissues in relation to the distribution of tensed and buckled fibers.* J Biomech Eng, 2007. **129**(2): p. 240-9.

82. Ateshian, G.A., et al., *Modeling the matrix of articular cartilage using a continuous fiber angular distribution predicts many observed phenomena.* J Biomech Eng, 2009. **131**(6): p. 061003.

83. Benninghoff, A., *Form und Bau der Gelenkknorpel in ihren Beziehungen zur Funktion.* Zietschrift fur Anatomie und Entwicklungsgeschichte, 1925.

84. Pierce, D.M., et al., *A phenomenological approach toward patient-specific computational modeling of articular cartilage including collagen fiber tracking.* J Biomech Eng, 2009. **131**(9): p. 091006.

85. Gupta, S., et al., *A fiber reinforced poroelastic model of nanoindentation of porcine costal cartilage: a combined experimental and finite element approach.* J Mech Behav Biomed Mater, 2009. **2**(4): p. 326-37; discussion 337-8.

86. Griffin, D.J., et al., *Effects of enzymatic treatments on the depth-dependent viscoelastic shear properties of articular cartilage.* J Orthop Res, 2014. **32**(12): p. 1652-7.

87. Hayes, W.C. and A.J. Bodine, *Flow-independent viscoelastic properties of articular cartilage matrix.* J Biomech, 1978. **11**(8-9): p. 407-19.

88. Armstrong, C.G., W.M. Lai, and V.C. Mow, *An analysis of the unconfined compression of articular cartilage.* J Biomech Eng, 1984. **106**(2): p. 165-73.

89. Maas, S.A., G.A. Ateshian, and J.A. Weiss, *FEBio: History and Advances.* Annu Rev Biomed Eng, 2017. **19**: p. 279-299.

90. Maas, S.A., et al., *FEBio: finite elements for biomechanics.* J Biomech Eng, 2012. **134**(1): p. 011005.

91. Wahlquist, J.A., et al., *Indentation mapping revealed poroelastic, but not viscoelastic, properties spanning native zonal articular cartilage.* Acta Biomater, 2017. **64**: p. 41-49.

92. Holmes, M.H. and V.C. Mow, *The nonlinear characteristics of soft gels and hydrated connective tissues in ultrafiltration.* J Biomech, 1990. **23**(11): p. 1145-56.

93. Anderson, A.E., et al., *Validation of finite element predictions of cartilage contact pressure in the human hip joint.* J Biomech Eng, 2008. **130**(5): p. 051008.

94. Wen, D., et al., *Lipids and collagen matrix restrict the hydraulic permeability within the porous compartment of adult cortical bone.* Ann Biomed Eng, 2010. **38**(3): p. 558-69.

95. Harris, M.D., et al., *Finite element prediction of cartilage contact stresses in normal human hips.* J Orthop Res, 2012. **30**(7): p. 1133-9.

96. University, M.S., *Hyalite high performance computing system.* 2020.

97. June, R.K. and D.P. Fyhrie, *A comparison of cartilage stress-relaxation models in unconfined compression: QLV and stretched exponential in combination with fluid flow.* Comput Methods Biomech Biomed Engin, 2013. **16**(5): p. 565-76.

98. June, R.K., et al., *Cartilage stress-relaxation is affected by both the charge concentration and valence of solution cations.* Osteoarthritis Cartilage, 2009. **17**(5): p. 669-76.

99. Smith, R.L., et al., *Effects of fluid-induced shear on articular chondrocyte morphology and metabolism in vitro.* J Orthop Res, 1995. **13**(6): p. 824-31.

100. Healy, Z.R., et al., *Divergent responses of chondrocytes and endothelial cells to shear stress: cross-talk among COX-2, the phase 2 response, and apoptosis.* Proc Natl Acad Sci U S A, 2005. **102**(39): p. 14010-5.

101. Doyran, B., et al., *Nanoindentation modulus of murine cartilage: a sensitive indicator of the initiation and progression of post-traumatic osteoarthritis.* Osteoarthritis Cartilage, 2017. **25**(1): p. 108-117.

102. Mahjoub, M., F. Berenbaum, and X. Houard, *Why subchondral bone in osteoarthritis? The importance of the cartilage bone interface in osteoarthritis.* Osteoporos Int, 2012. **23 Suppl 8**: p. S841-6.

103. Cinque, M.E., et al., *High Rates of Osteoarthritis Develop After Anterior Cruciate Ligament Surgery: An Analysis of 4108 Patients.* Am J Sports Med, 2018. **46**(8): p. 2011-2019.

104. Anderson, D.D., et al., *Post-traumatic osteoarthritis: improved understanding and opportunities for early intervention.* J Orthop Res, 2011. **29**(6): p. 802-9.

105. Kramer, W.C., K.J. Hendricks, and J. Wang, *Pathogenetic mechanisms of posttraumatic osteoarthritis: opportunities for early intervention.* Int J Clin Exp Med, 2011. **4**(4): p. 285-98.

106. Khorasani, M.S., et al., *Effect of alendronate on post-traumatic osteoarthritis induced by anterior cruciate ligament rupture in mice.* Arthritis Res Ther, 2015. **17**(1): p. 30.

107. Maycas, M., P. Esbrit, and A.R. Gortazar, *Molecular mechanisms in bone mechanotransduction.* Histol Histopathol, 2017. **32**(8): p. 751-760.

108. Stock, J.T., *Wolff's law (bone functional adaptation).* The International Encylopedia of Biological Anthropology, 2018.

109. Alliston, T., et al., *Bone marrow lesions in osteoarthritis: What lies beneath.* J Orthop Res, 2018. **36**(7): p. 1818-1825.

110. Mazur, C.M., et al., *Osteocyte dysfunction promotes osteoarthritis through MMP13-dependent suppression of subchondral bone homeostasis.* Bone Res, 2019. **7**: p. 34.

111. McMahon, M. and J.A. Block, *The risk of contralateral total knee arthroplasty after knee replacement for osteoarthritis.* J Rheumatol, 2003. **30**(8): p. 1822-4.

112. White, M.S., R.J. Brancati, and L.K. Lepley, *Relationship between altered knee kinematics and subchondral bone remodeling in a clinically translational model of ACL injury.* J Orthop Res, 2022. **40**(1): p. 74-86.

113. Sward, P., et al., *Cartilage and bone markers and inflammatory cytokines are increased in synovial fluid in the acute phase of knee injury (hemarthrosis)--a cross-sectional analysis.* Osteoarthritis Cartilage, 2012. **20**(11): p. 1302-8.

114. Domazetovic, V., et al., *Oxidative stress in bone remodeling: role of antioxidants.* Clin Cases Miner Bone Metab, 2017. **14**(2): p. 209-216.

115. Vashishth, D., et al., *Influence of nonenzymatic glycation on biomechanical properties of cortical bone.* Bone, 2001. **28**(2): p. 195-201.

116. Patti, G.J., O. Yanes, and G. Siuzdak, *Innovation: Metabolomics: the apogee of the omics trilogy.* Nat Rev Mol Cell Biol, 2012. **13**(4): p. 263-9.

117. Wallace, C.W., et al., *Correlations between metabolites in the synovial fluid and serum: A mouse injury study.* J Orthop Res, 2022. **40**(12): p. 2792-2802.

118. De Souza, R.L., et al., *Non-invasive axial loading of mouse tibiae increases cortical bone formation and modifies trabecular organization: a new model to study cortical and cancellous compartments in a single loaded element.* Bone, 2005. **37**(6): p. 810-8.

119. Lockwood, K.A., et al., *Comparison of loading rate-dependent injury modes in a murine model of post-traumatic osteoarthritis.* J Orthop Res, 2014. **32**(1): p. 79-88.

120. Bouxsein, M.L., et al., *Guidelines for assessment of bone microstructure in rodents using micro-computed tomography.* J Bone Miner Res, 2010. **25**(7): p. 1468-86.

121. Schindelin, J., et al., *Fiji: an open-source platform for biological-image analysis.* Nature Methods, 2012. **9**(7): p. 676-682.

122. Vahidi, G., et al., *Bone biomechanical properties and tissue-scale bone quality in a genetic mouse model of familial dysautonomia.* Osteoporos Int, 2021. **32**(11): p. 2335-2346.

123. Bushby, A.J., V.L. Ferguson, and A. Boyde, *Nanoindentation of bone: Comparison of specimens tested in liquid and embedded in polymethylmethacrylate.* Journal of Materials Research, 2004. **19**(1): p. 249-259.

124. Domingo-Almenara, X., et al., *XCMS-MRM and METLIN-MRM: a cloud library and public resource for targeted analysis of small molecules.* Nat Methods, 2018. **15**(9): p. 681-684.

125. Ji, M. and Q. Yu, *Primary osteoporosis in postmenopausal women.* Chronic Diseases and Translational Medicine, 1015. **1**: p. 5.

126. Manitta, L., et al., *Nanoindentation of Subchondral Bone During Osteoarthritis Pathological Process Using Atomic Force Microscopy.* Computer Methods, Imaging and Visualization in Biomechanics and Biomedical Engineering, 2020. **36**: p. 505-517.

127. Fritton, S.P. and S. Weinbaum, *Fluid and Solute Transport in Bone: Flow-Induced Mechanotransduction.* Annual Review of Fluid Mechanics, 2009. **41**: p. 347-374.

128. Kleinnulend, J., et al., *Sensitivity of Osteocytes to Biomechanical Stress in-Vitro.* Faseb Journal, 1995. **9**(5): p. 441-445.

129. Jay, G.D., et al., *The role of lubricin in the mechanical behavior of synovial fluid.* Proceedings of the National Academy of Sciences of the United States of America, 2007. **104**(15): p. 6194-6199.

130. Fritton, S.P. and S. Weinbaum, *Fluid and Solute Transport in Bone: Flow-Induced Mechanotransduction.* Annu Rev Fluid Mech, 2009. **41**: p. 347-374.

131. Burstein, D., et al., *Protocol issues for delayed Gd(DTPA)(2-)-enhanced MRI (dGEMRIC) for clinical evaluation of articular cartilage.* Magn Reson Med, 2001. **45**(1): p. 36-41.

132. Leddy, H.A. and F. Guilak, *Site-specific molecular diffusion in articular cartilage measured using fluorescence recovery after photobleaching.* Ann Biomed Eng, 2003. **31**(7): p. 753-60.

133. Pluen, A., et al., *Diffusion of macromolecules in agarose gels: comparison of linear and globular configurations.* Biophys J, 1999. **77**(1): p. 542-52.

134. Soltz, M.A. and G.A. Ateshian, *Experimental verification and theoretical prediction of cartilage interstitial fluid pressurization at an impermeable contact interface in confined compression.* J Biomech, 1998. **31**(10): p. 927-34.

135. Hislop, B.D., et al., *Osteochondral fluid transport in an ex-vivo system.* BioRxiv, 2023.

136. Nazemi, S.M., et al., *Accounting for spatial variation of trabecular anisotropy with subject-specific finite element modeling moderately improves predictions of local subchondral bone stiffness at the proximal tibia.* J Biomech, 2017. **59**: p. 101-108.

137. Yu, Z., et al., *Hybrid clustering solution selection strategy.* Pattern Recognition, 2014. **47**: p. 14.

138. Ronan, T., et al., *OpenEnsembles: A Python Resource library for Ensemble Clustering.* Journal of Machine Learning Research, 2018. **18**: p. 6.

139. Naegle, K.M., et al., *MCAM: multiple clustering analysis methodology for deriving hypotheses and insights from high-throughput proteomic datasets.* PLoS Comput Biol, 2011. **7**(7): p. e1002119.

140. Huang, D., C.-D. Wang, and J.-H. Lai, *Locally Weighted Ensemble Clustering.* IEEE TRans. on Cybernetics, 2018. **48**: p. 14.

141. Huang, D., J.-H. Lai, and C.-D. Wang, *Combining multiple clusterings via crowd agreement estimation and multi-granularity link analysis.* Neurocomputing, 2015. **170**: p. 11.

142. Strehl, A. and J. Ghosh, *Cluster ensembles - A knowledge reuse framework for combining partitionings.* Eighteenth National Conference on Artificial Intelligence (Aaai-02)/Fourteenth Innovative Applications of Artificial Intelligence Conference (Iaai-02), Proceedings, 2002: p. 93-98.

143. Golalipour, K., et al., *From clustering to clustering ensemble selection: A review.* Engineering Applications of Artificial Intelligence, 2021. **104**.

144. James, G., et al., *Introduction to Statistical Learning: With Applications in R.* Introduction to Statistical Learning: With Applications in R, 2013. **103**: p. 1-426.

145. Rand, W.M., *Objective Criteria for the Evaluation of Clustering Methods.* Journal of the American Statistical Association, 1971. **66**: p. 4.

146. Hubert, L., *Comparing Partitions.* Journal of Classification, 1985. **2**: p. 15.

147. Virtanen, P., et al., *SciPy 1.0: fundamental algorithms for scientific computing in Python.* Nature Methods, 2020. **17**(3): p. 261-272.

148. Han, E.-H., et al., *Clustering in High-Dimensional Space Using Hypergraph Models*, in *Technical Report; 97-063*. 1997, University of Minnesota.

149. Bezdek, J.C., R. Ehrlich, and W. Full, *FCM: THE FUZZY c-MEANS CLUSTERING ALGORITHM.* Computers and Geosciences, 1984. **10**(2-3): p. 13.

150. Kluyver, T., et al., *Jupyter Notebooks -- a publishing format for reproducible computational workflows*, in *IOS Press*, F. Loizides and S. B., Editors. 2016. p. 4.

151. Outerbridge, R.E., *The etiology of chondromalacia patellae.* J Bone Joint Surg Br, 1961. **43-B**: p. 752-7.

152. Outerbridge, R.E., *Further Studies on the Etiology of Chondromalacia Patellae.* J Bone Joint Surg Br, 1964. **46**: p. 179-90.

153. Kim, S., et al., *Metabolite profiles of synovial fluid change with the radiographic severity of knee osteoarthritis.* Joint Bone Spine, 2017. **84**(5): p. 605-610.

154. Pang, Z., et al., *MetaboAnalystR 3.0: Toward an Optimized Workflow for Global Metabolomics.* Metabolites, 2020. **10**(5).

155. Pedregosa, F., et al., *Scikit-learn: Machine Learning in Python.* Journal of Machine Learning Research, 2011. **12**: p. 2825-2830.

APPENDICES

APPENDIX A

SUPPLEMENTARY FIGURES FOR CHAPTER 3

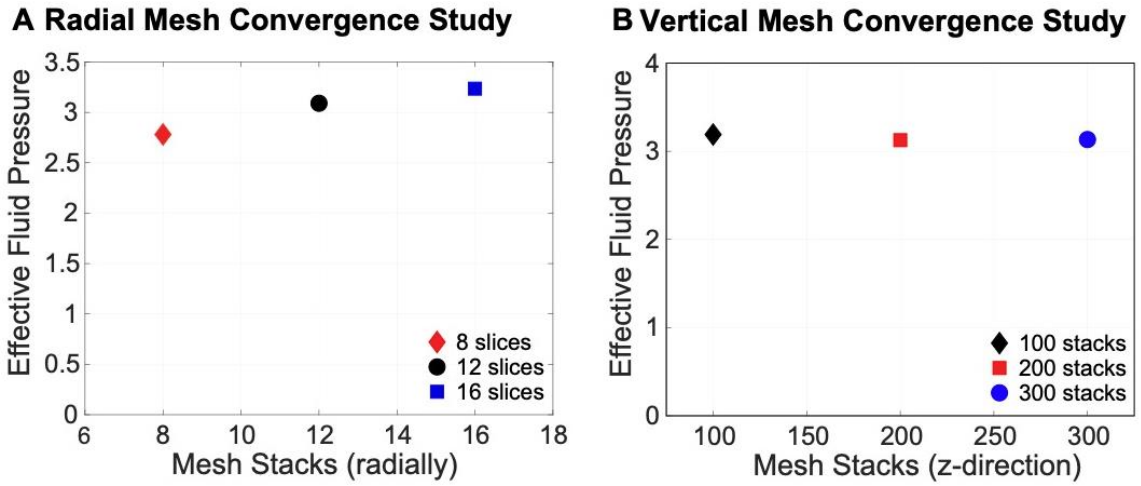

Figure A1. Mesh convergence studies. A) Radial mesh convergence studies B) Vertical mesh convergence studies.

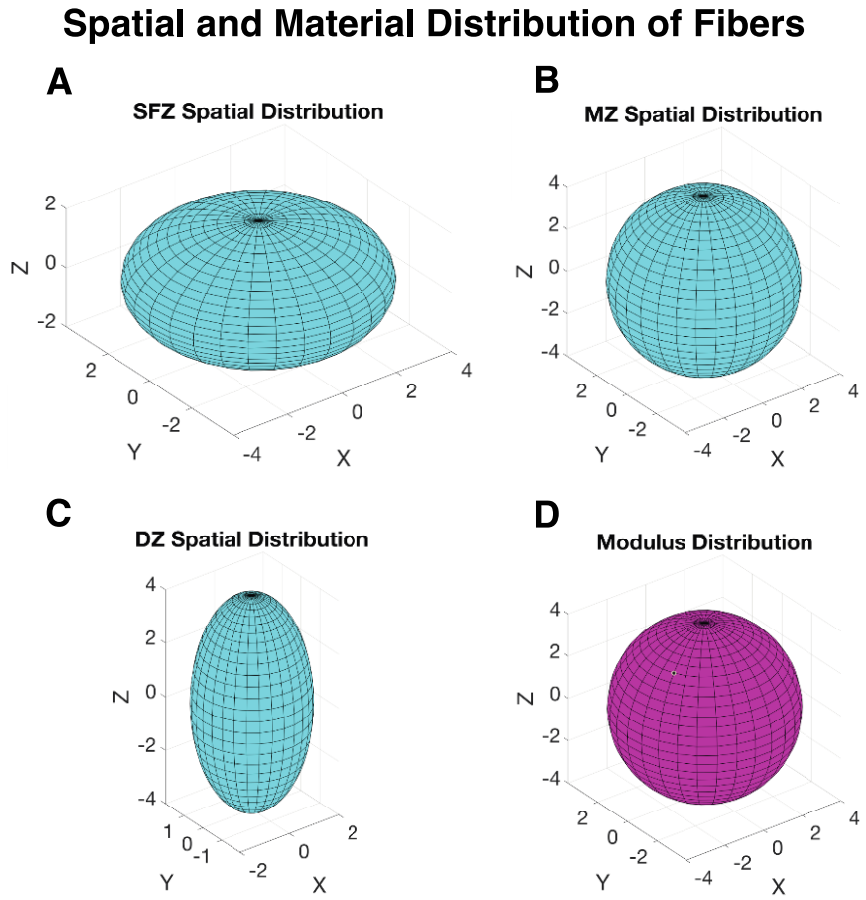

Figure A2. Spatial and material distribution of fibers A) Spatial distribution of superficial zone collagen fibers, B) Distribution of fibers in the middle zone, C) Distribution of collagen fibers in the deep zone, D) Distribution of the modulus of collagen fibers.

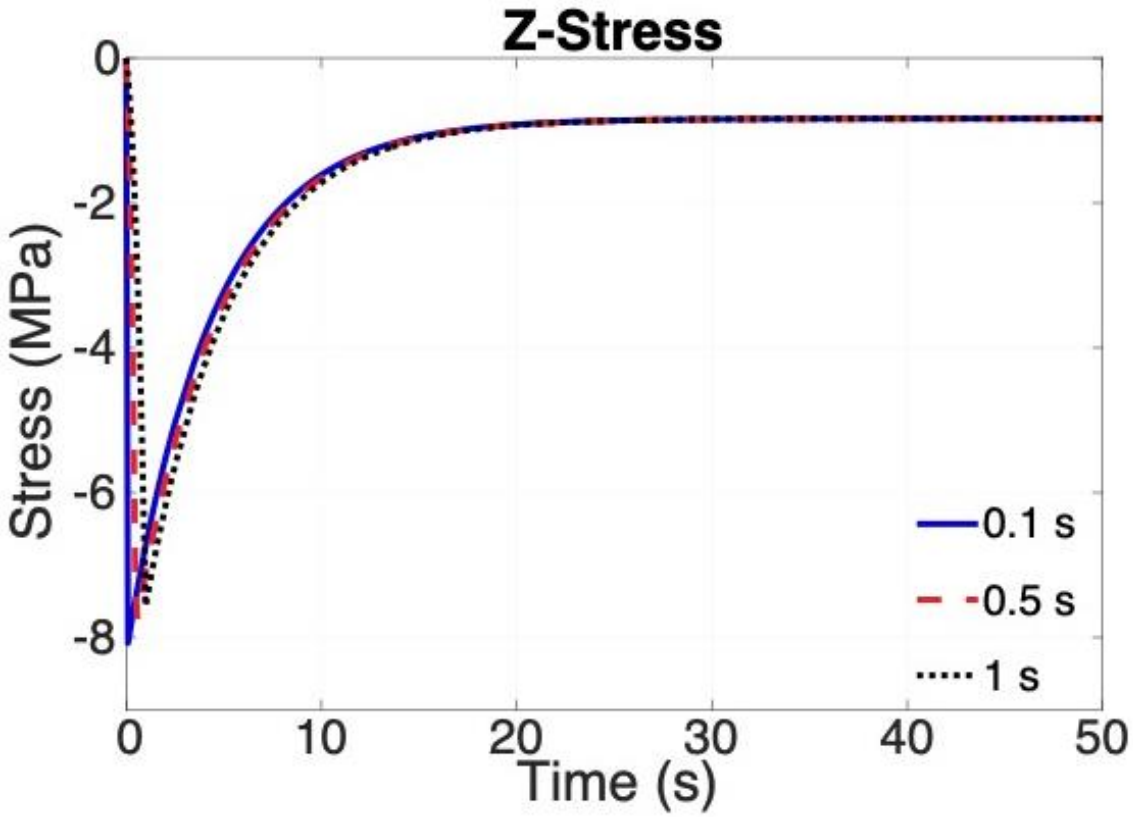

Figure A3. Z-stress with respect to the loading rate.

APPENDIX B

SUPPLEMENTARY MATERIALS FOR CHAPTER 4

Cluster Validation and Ensemble Clustering

Cluster validation uses a minimum spanning tree classification combined with a validation index (**S1**) to make a data-driven decision on the optimum number of clusters for a given dataset.

$$\boldsymbol{validation\ index} = \frac{\boldsymbol{cluster\ compactness}}{\boldsymbol{cluster\ separation}} \quad \textbf{(S1)}$$

The optimum number of clusters for a given dataset is the minimum of the validation index. Then, this number of clusters is used to evaluate the hierarchical cluster outputs. Ensemble clustering evaluates multiple hierarchical clustering outputs to determine the percentage of times each metabolite (from 1 to N) clusters with every other metabolite within the data set.

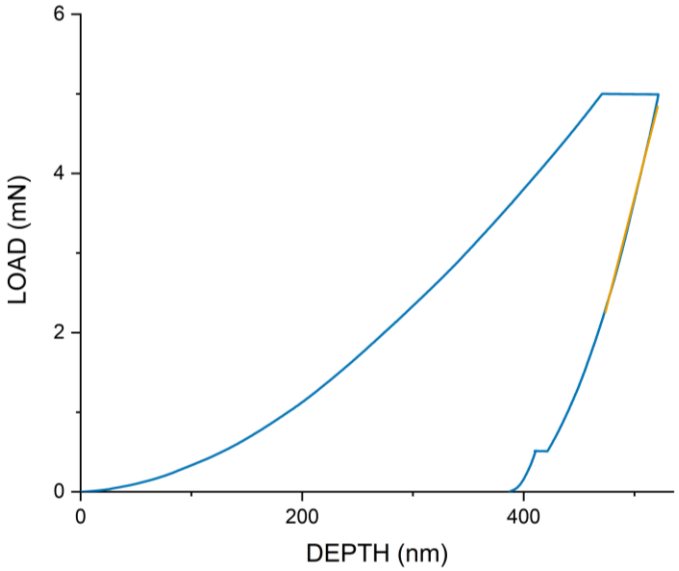

Figure B1. Load-Depth curve showing unloading region used for analysis of modulus properties.

Sham-Injured, Injured, & Contralateral-to-Injured Metabolomic Analysis

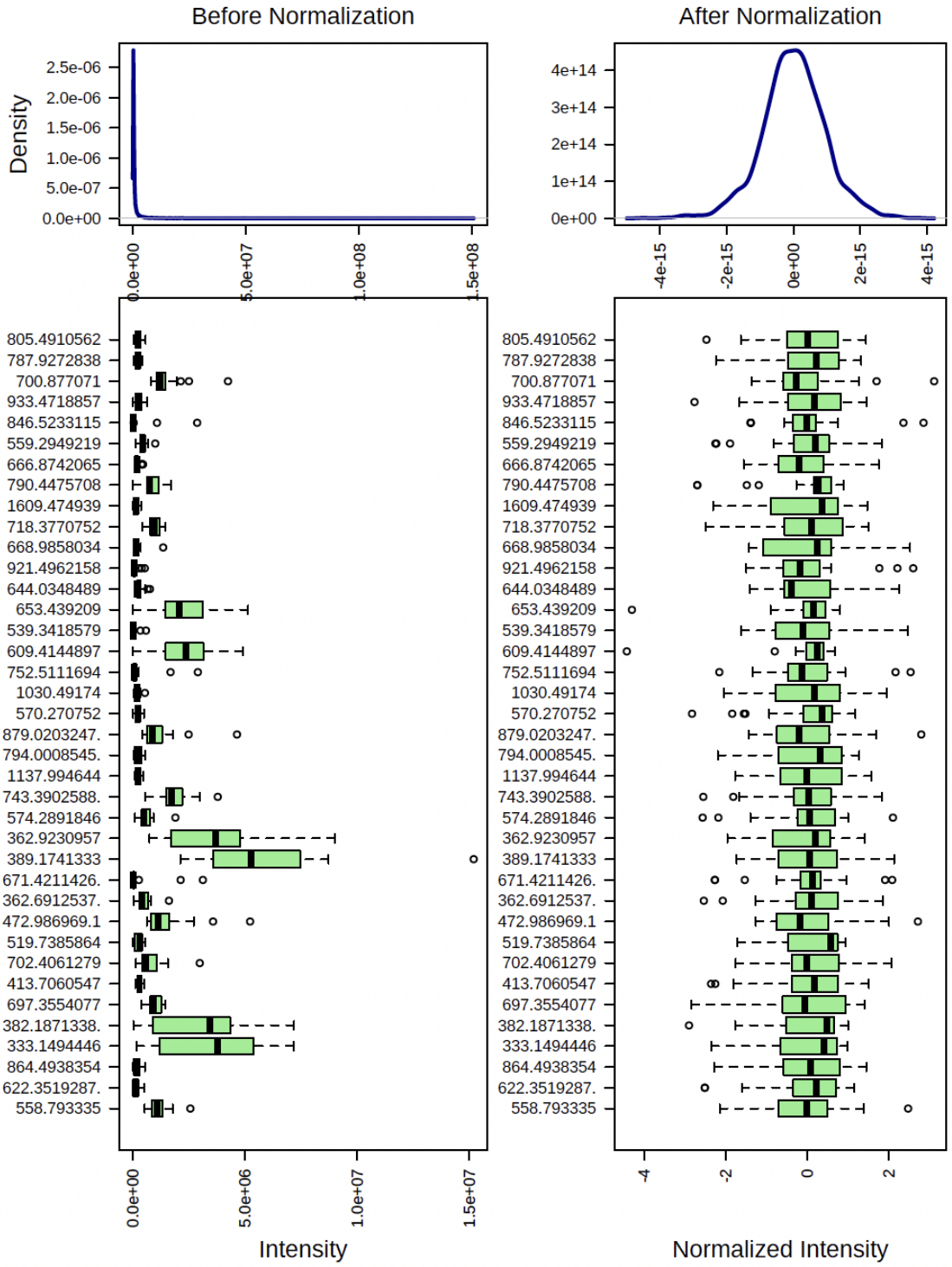

Figure B2. Results from normalization of metabolic data, using log-transform, and auto-scaling.

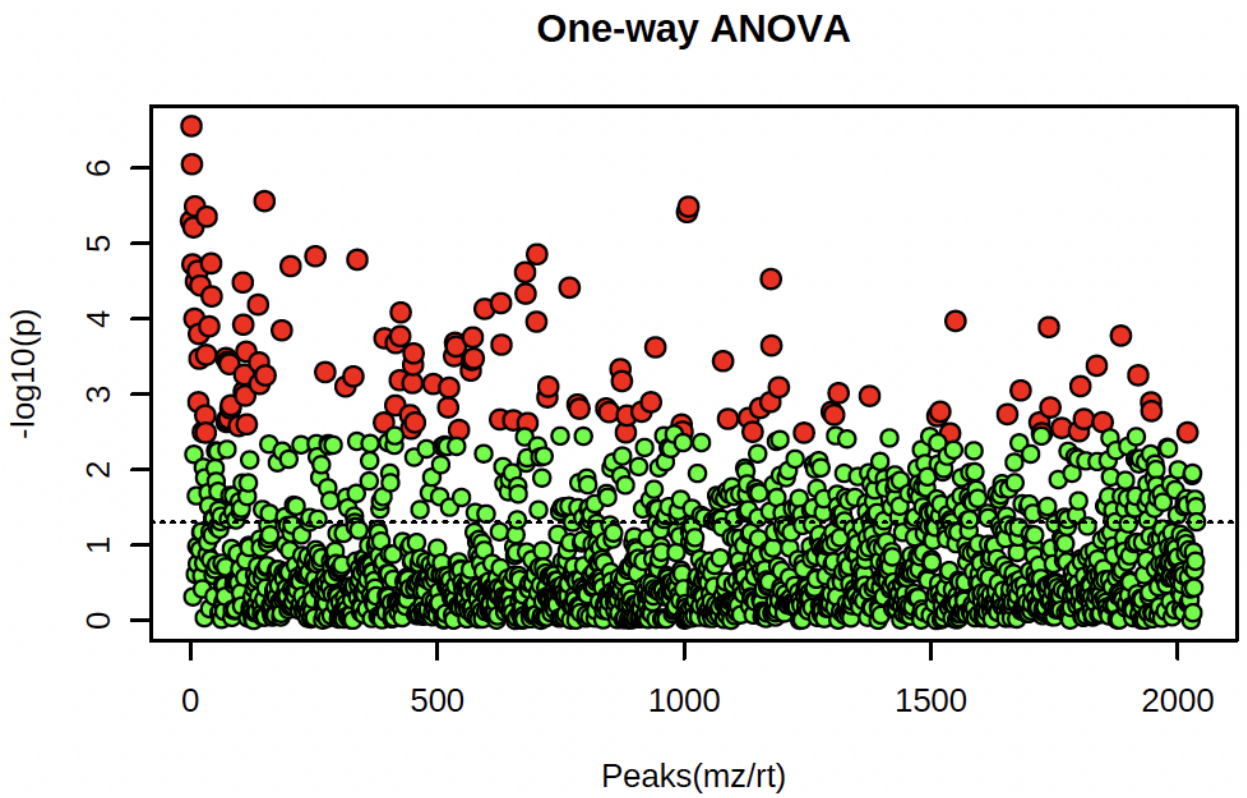

Figure B3. One-way ANOVA showing significant ($p<0.05$) metabolites in red.

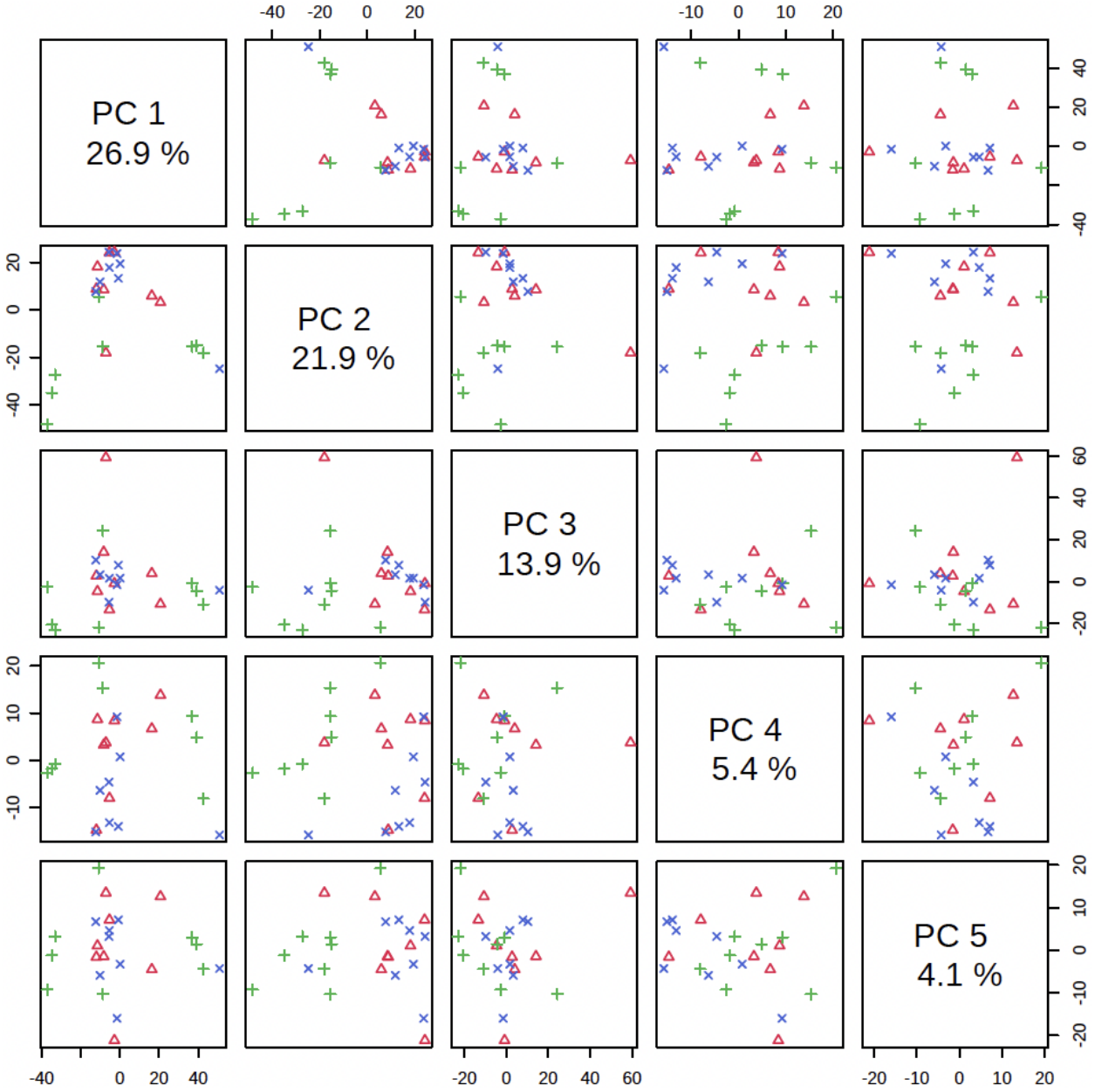

Figure B4: Pair plots for principal component analysis.

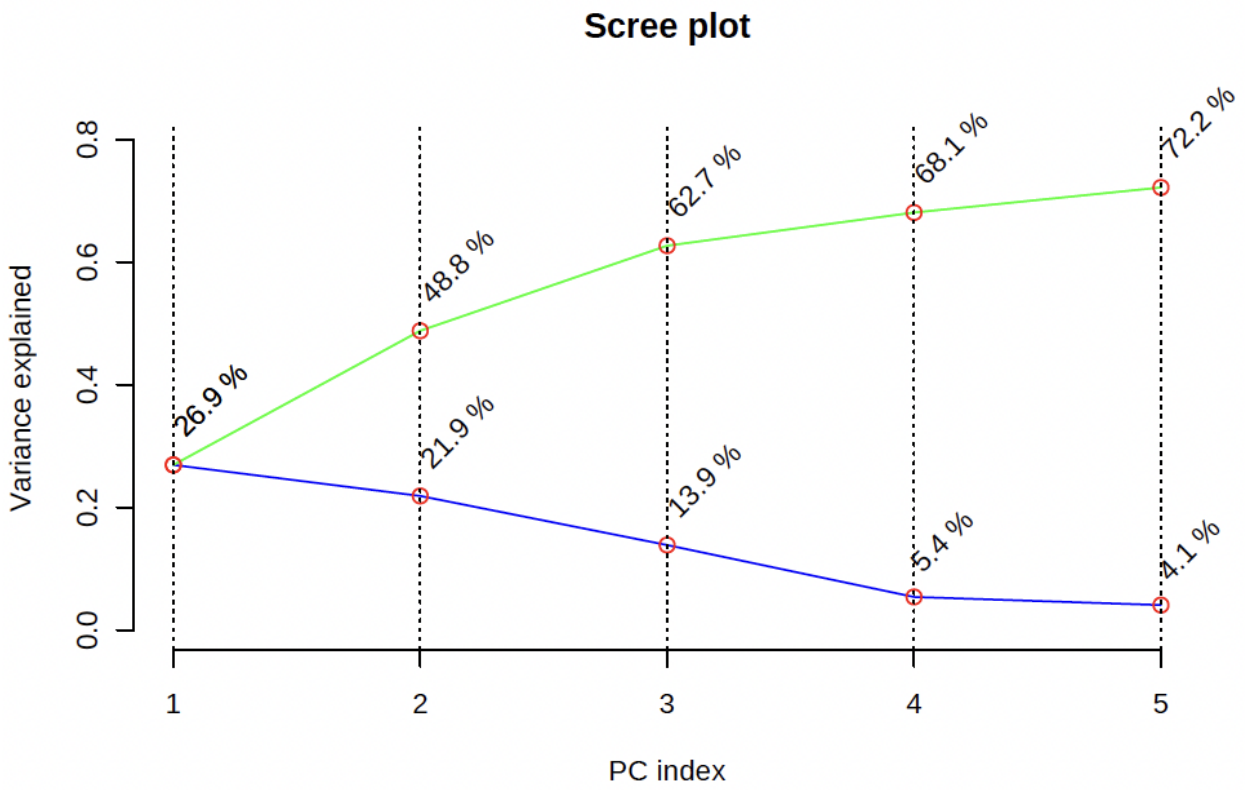

Figure B5. Scree plot for principal component analysis.

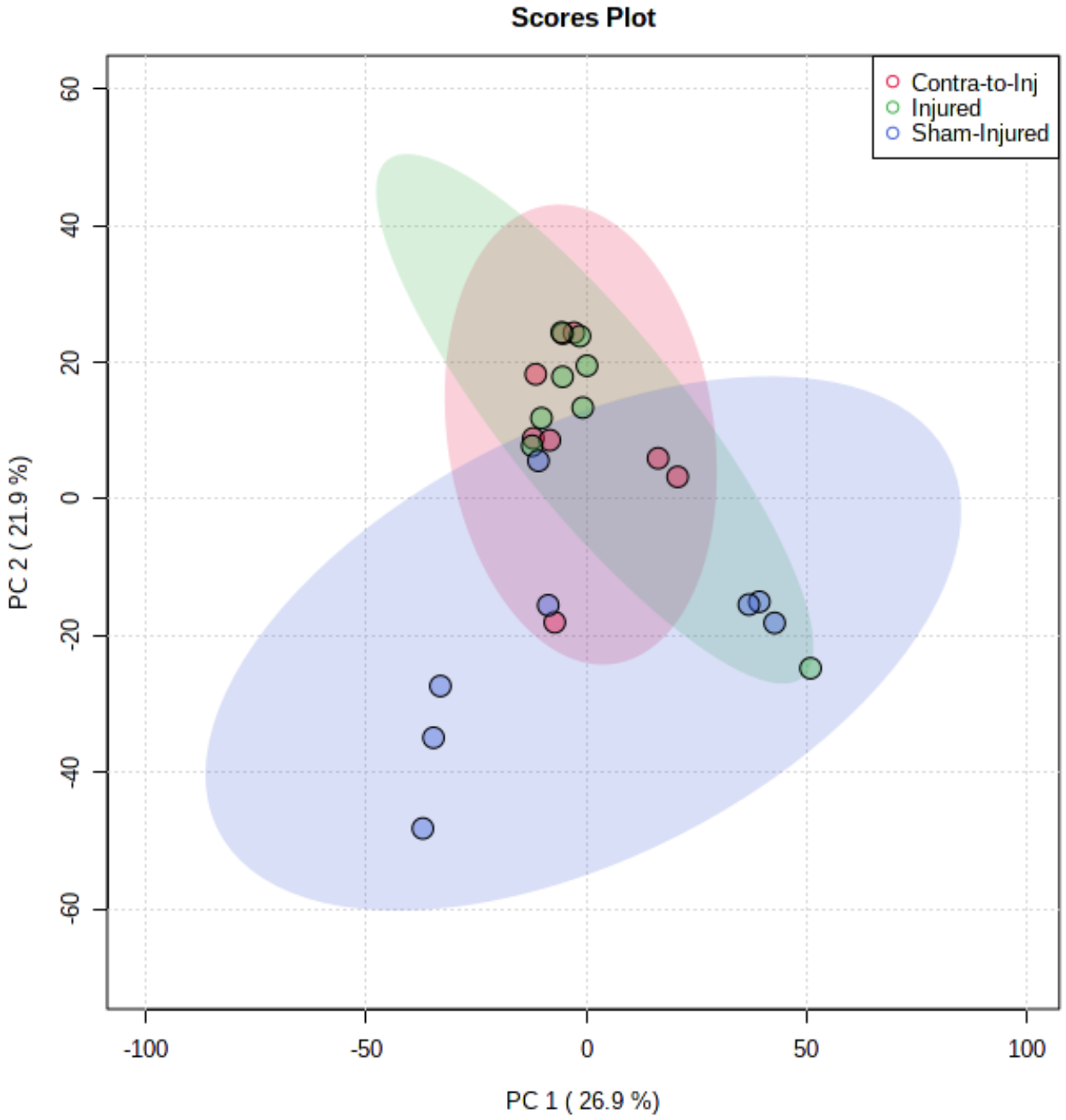

Figure B6. Principal component analysis 2D score plot of PC1 v. PC2

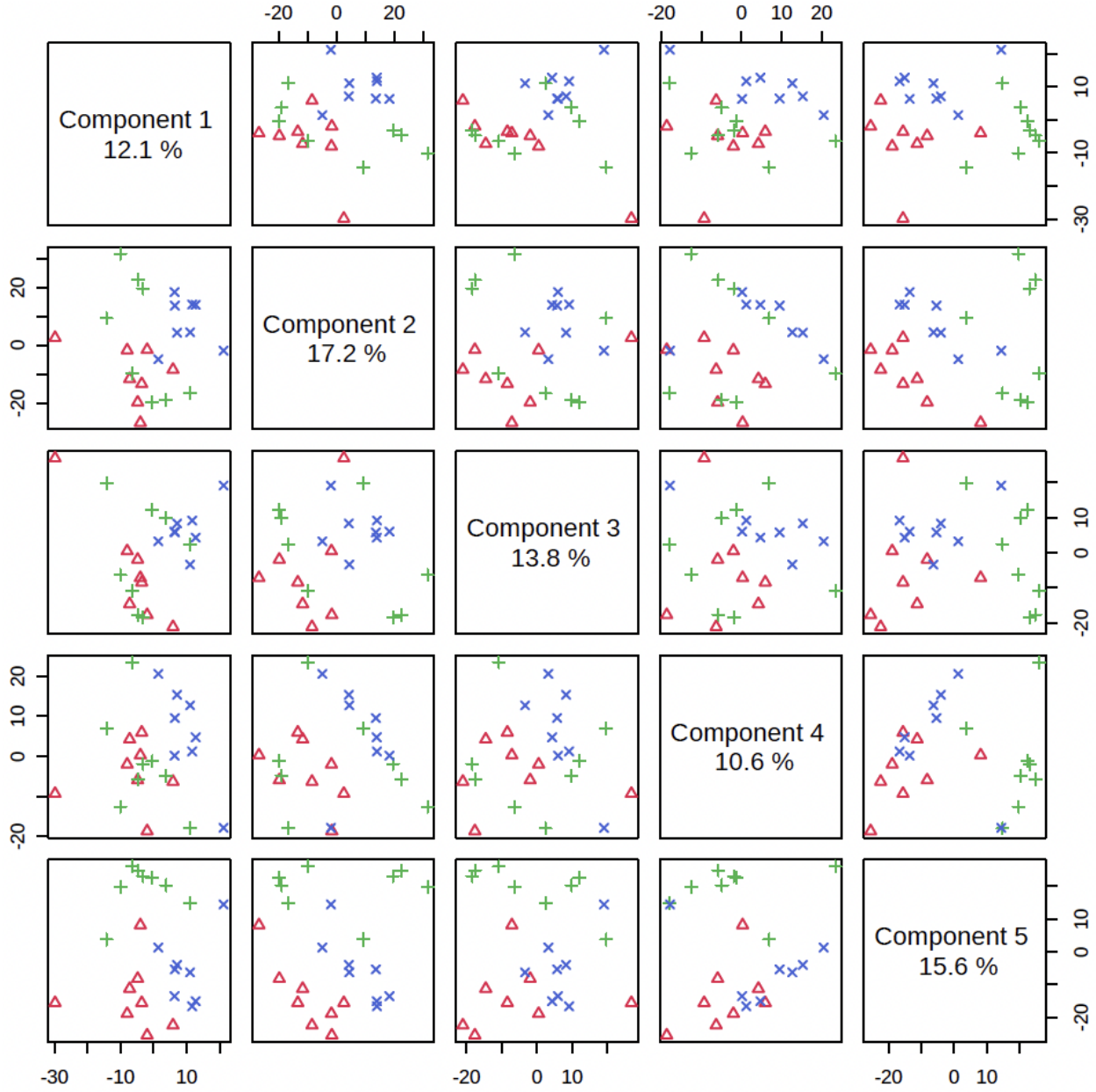

Figure B7. Principal component analysis 2D score plot of PC1 v. PC2

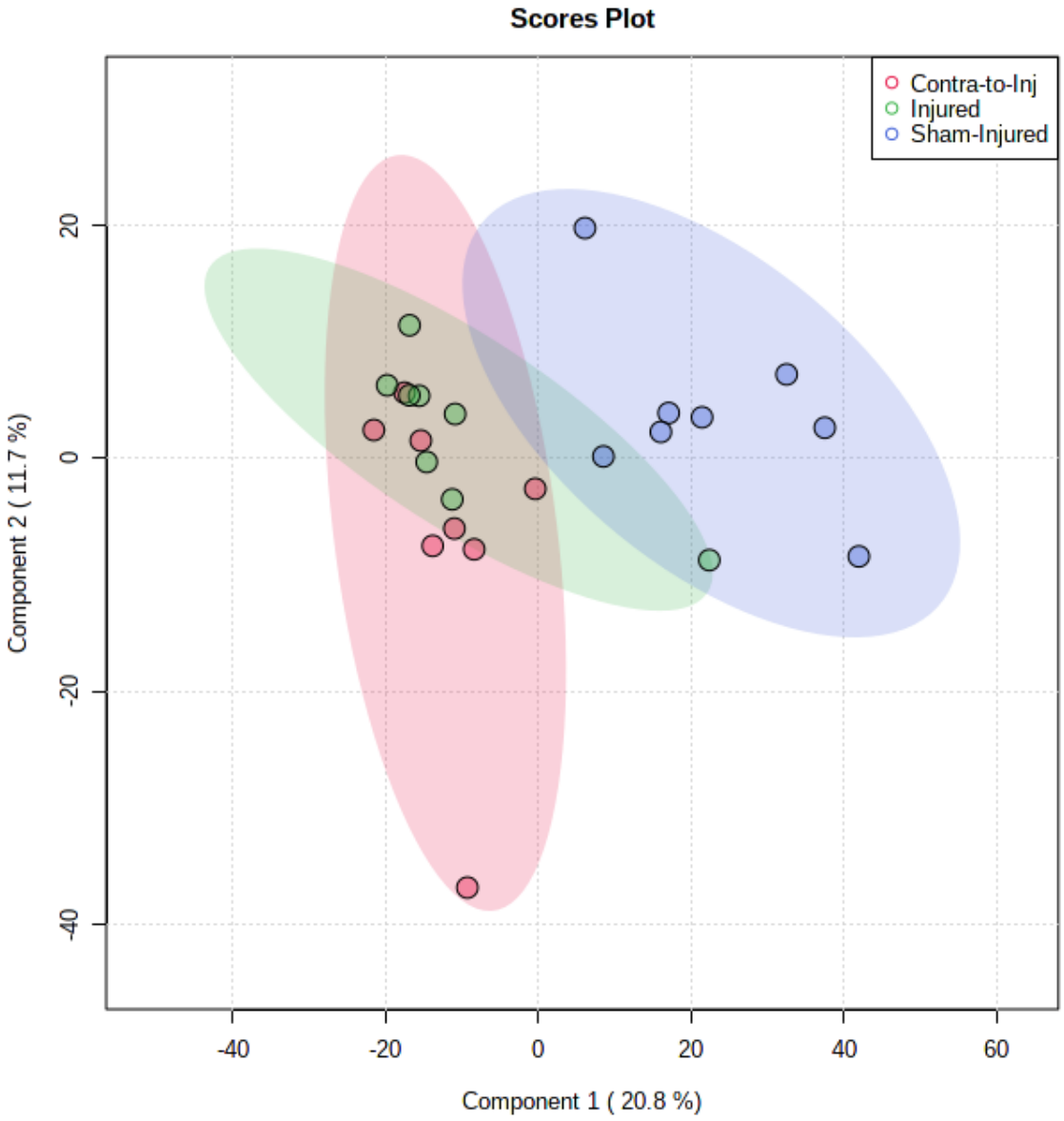

Figure B8. Partial least squares – discriminant analysis 2D score plot of Component 1 v. Component 2.

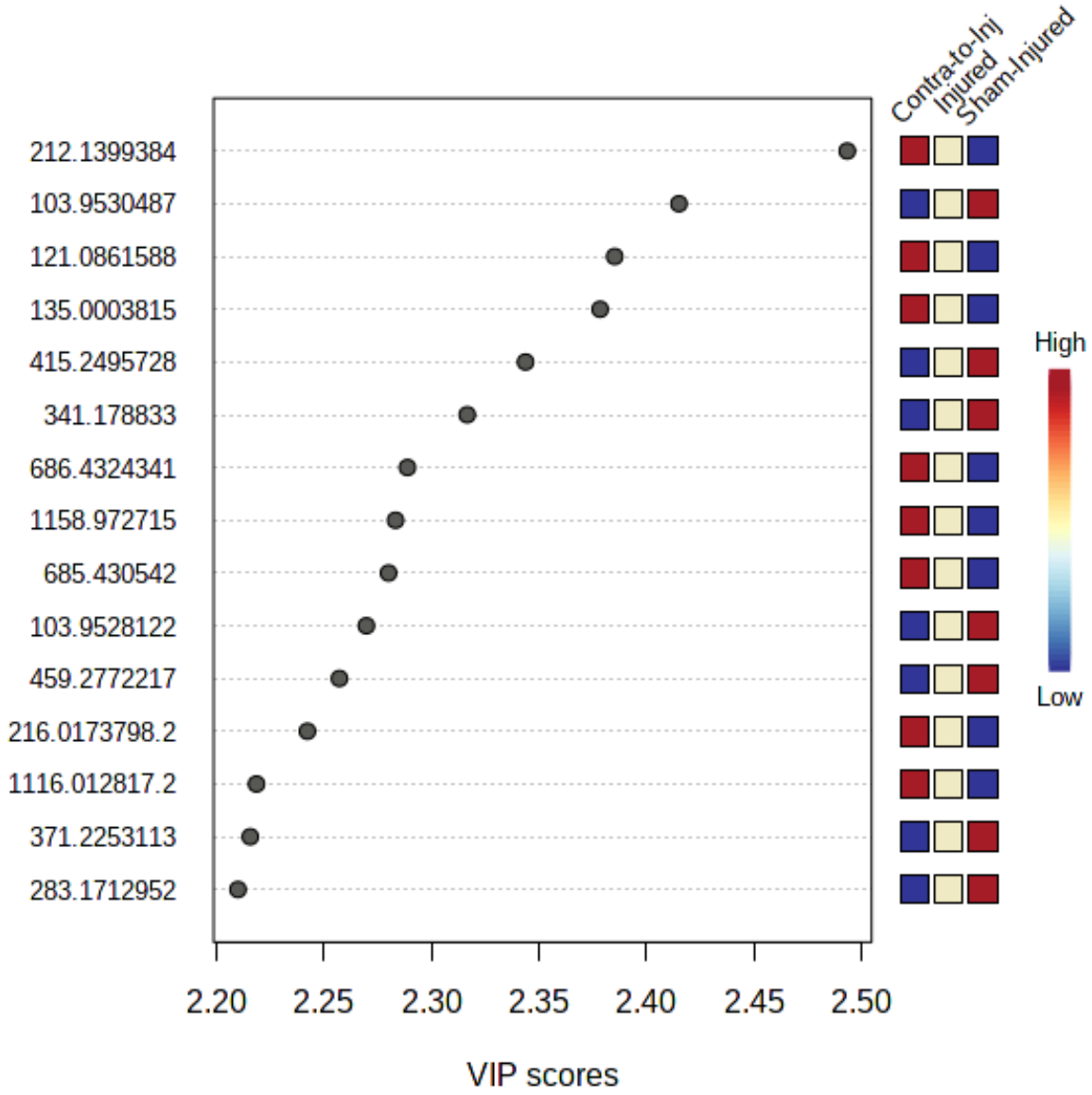

Figure B9: Variable importance projections from partial least squares – discriminant analysis

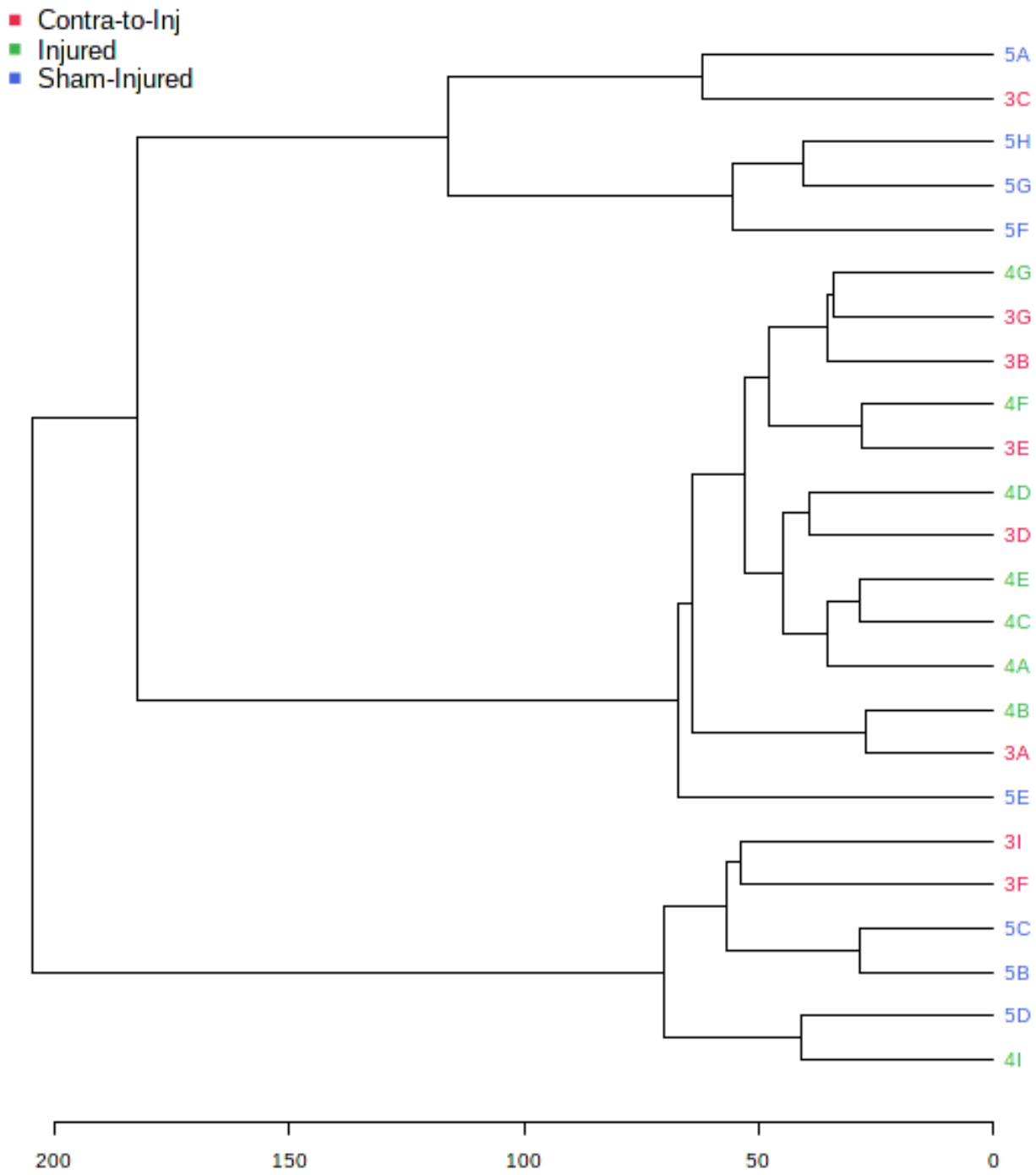

Figure B10: Dendrogram of hierarchical clustering of metabolic data with groups Contralateral-to-Injured, Injured, and Sham-Injured synovial fluid.

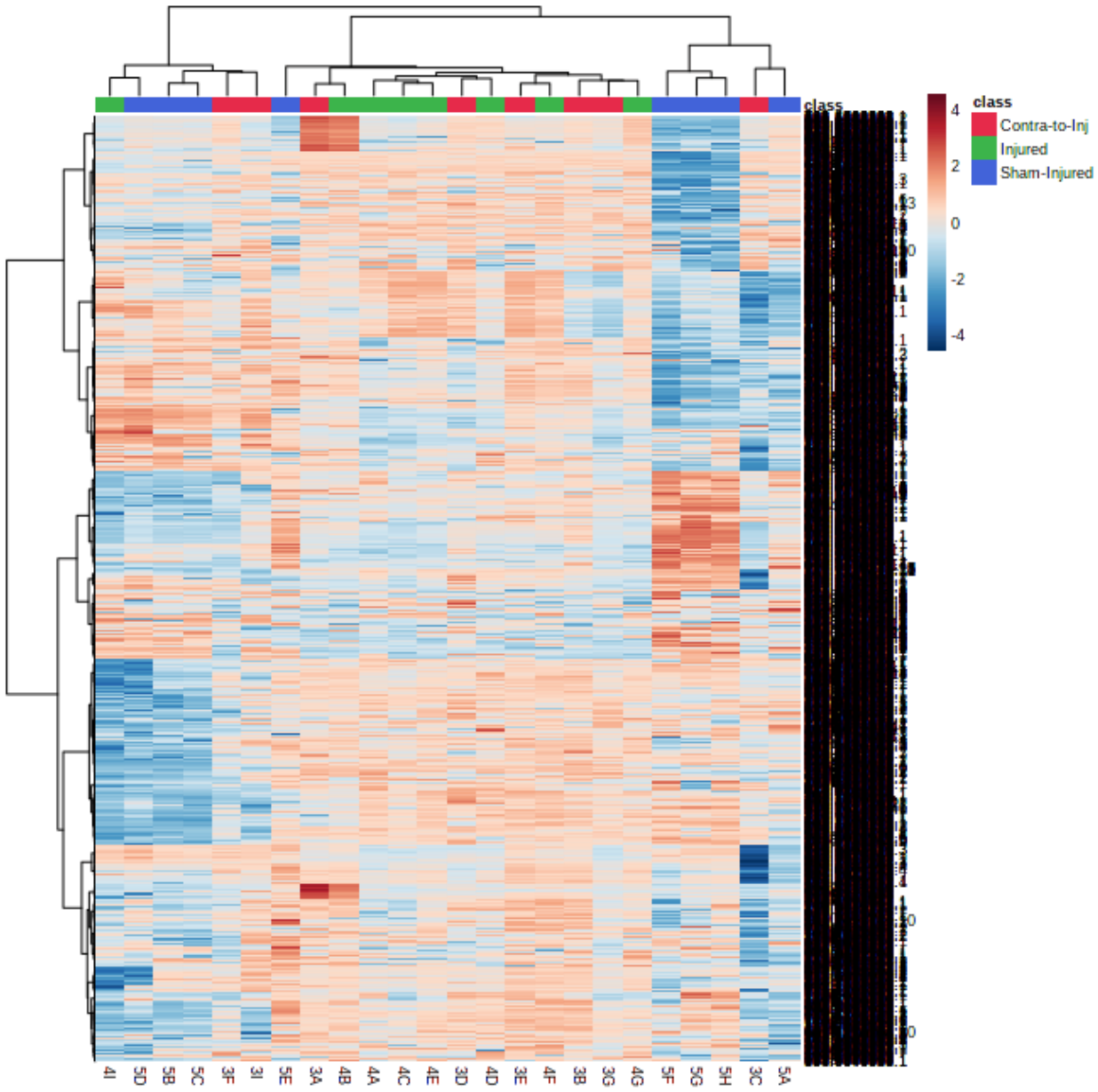

Figure B11. Clustergram of the metabolic data from Contralateral-to-Injured, Injured, and Sham-Injured synovial fluid data.

Clustering Validation and Ensemble Clustering

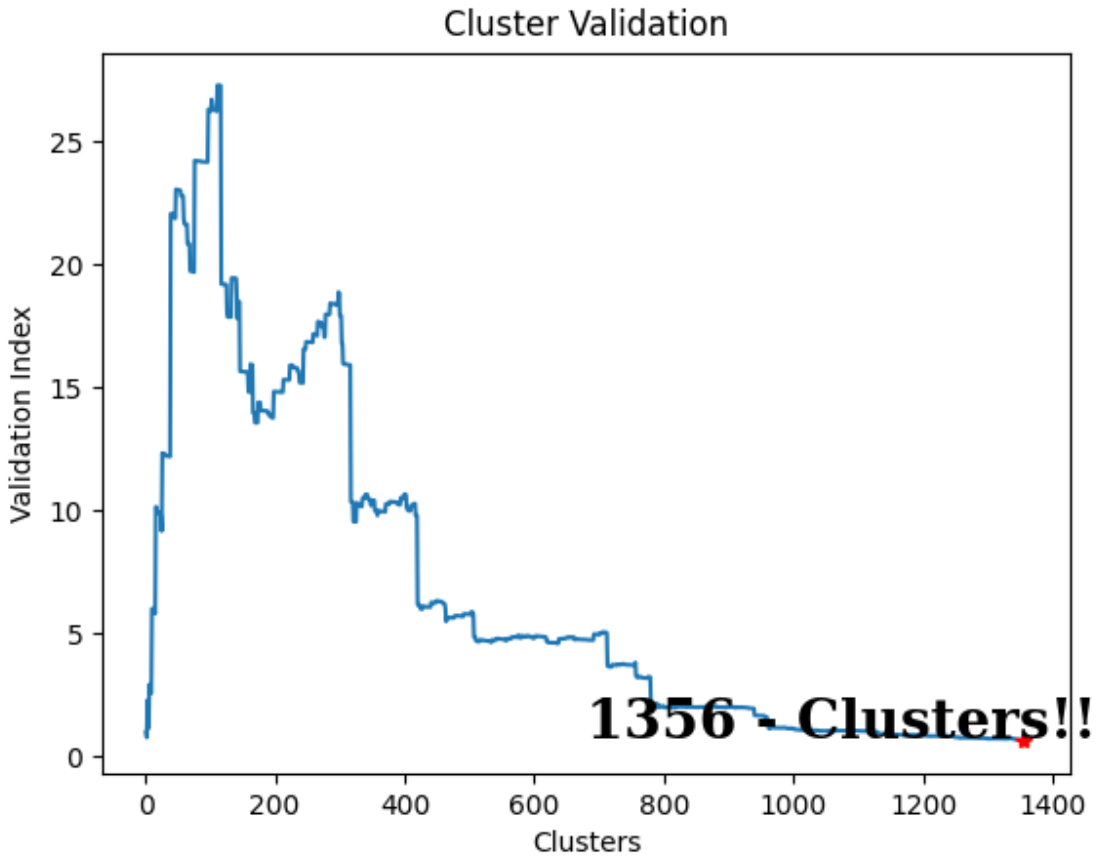

Figure B12. Clustering validation results for three group comparison.

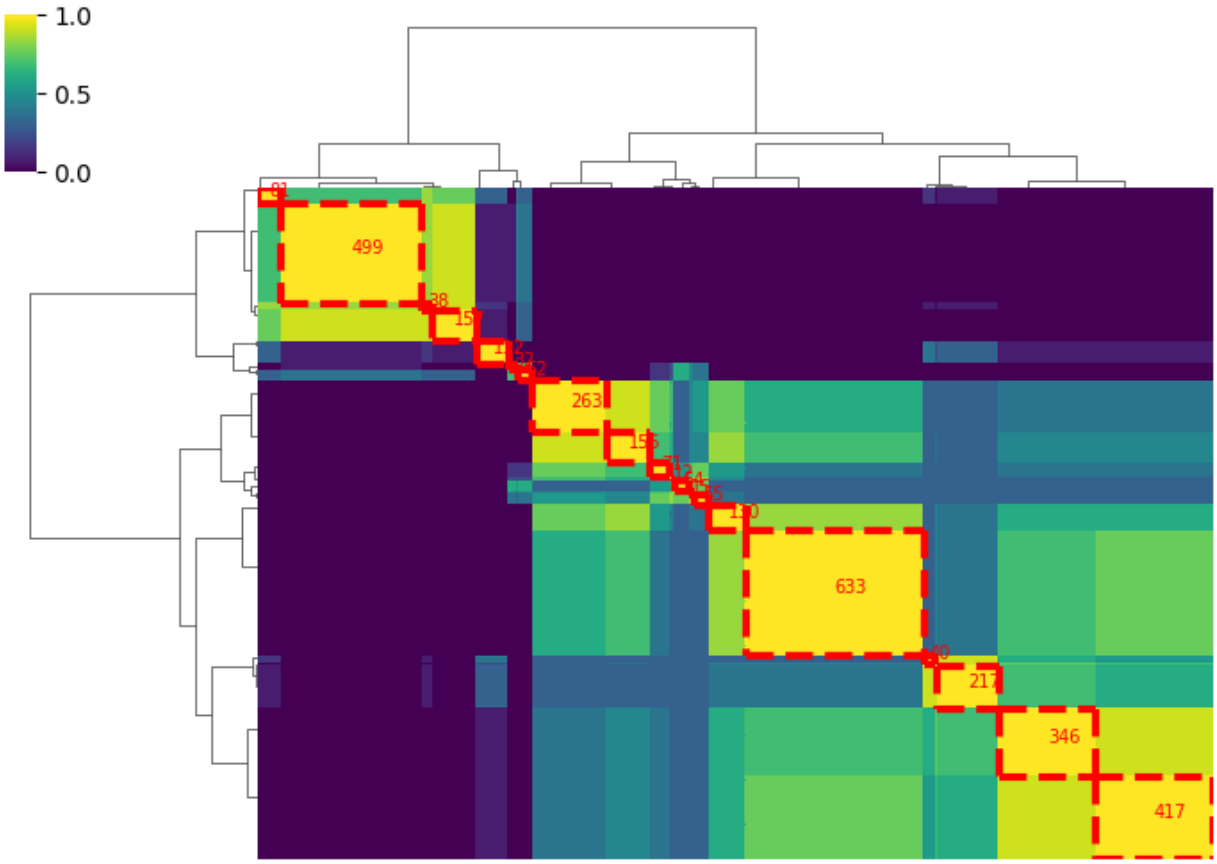

Figure B13. Ensemble clustering result. Red-dashed boxed represent metabolites that clustered together in each of the clustering solutions considered.

Sham-Injured & Injured Metabolomic Analysis

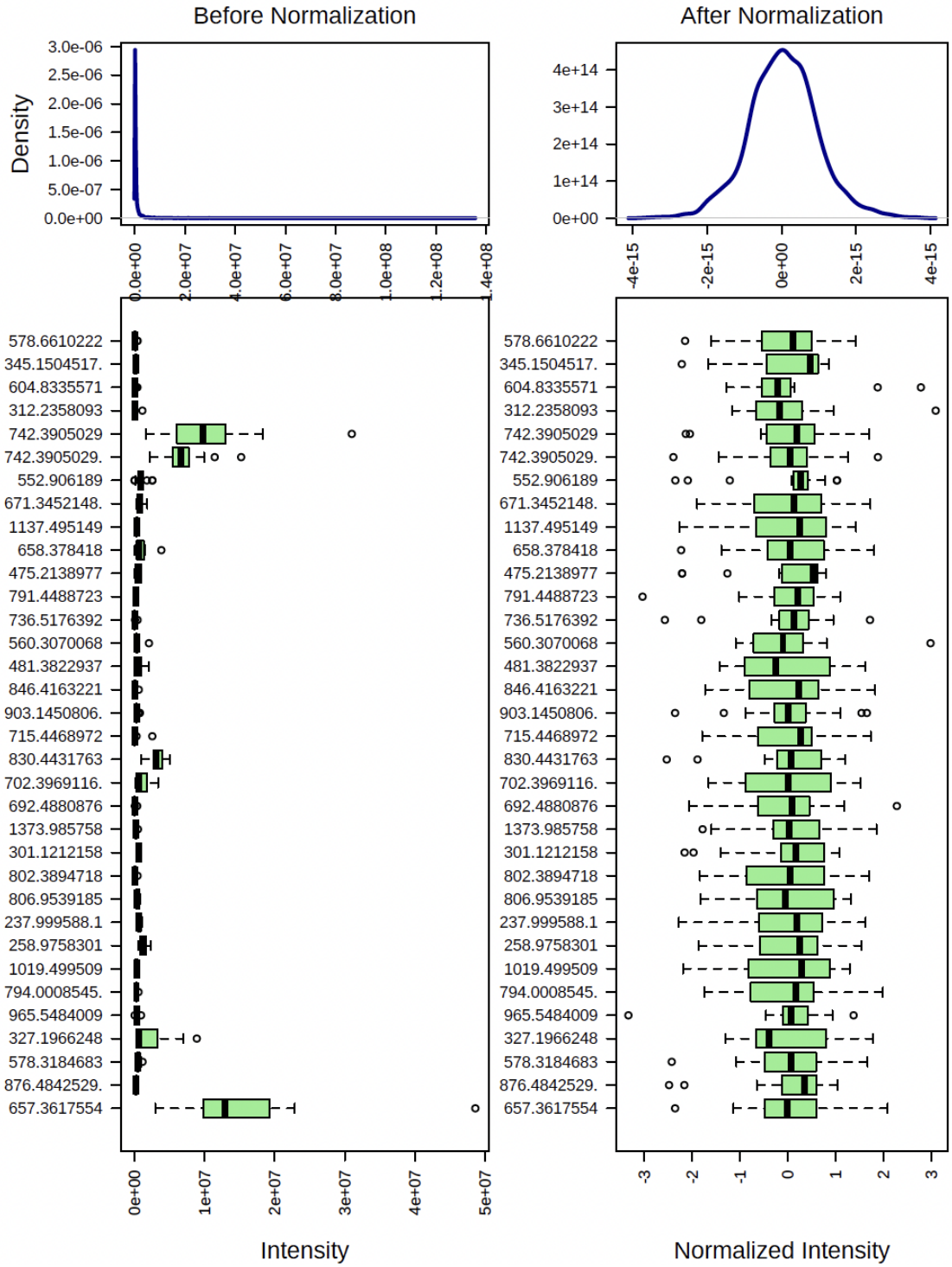

Figure B14. Normalization results for Sham-Injured v. Injured comparison.

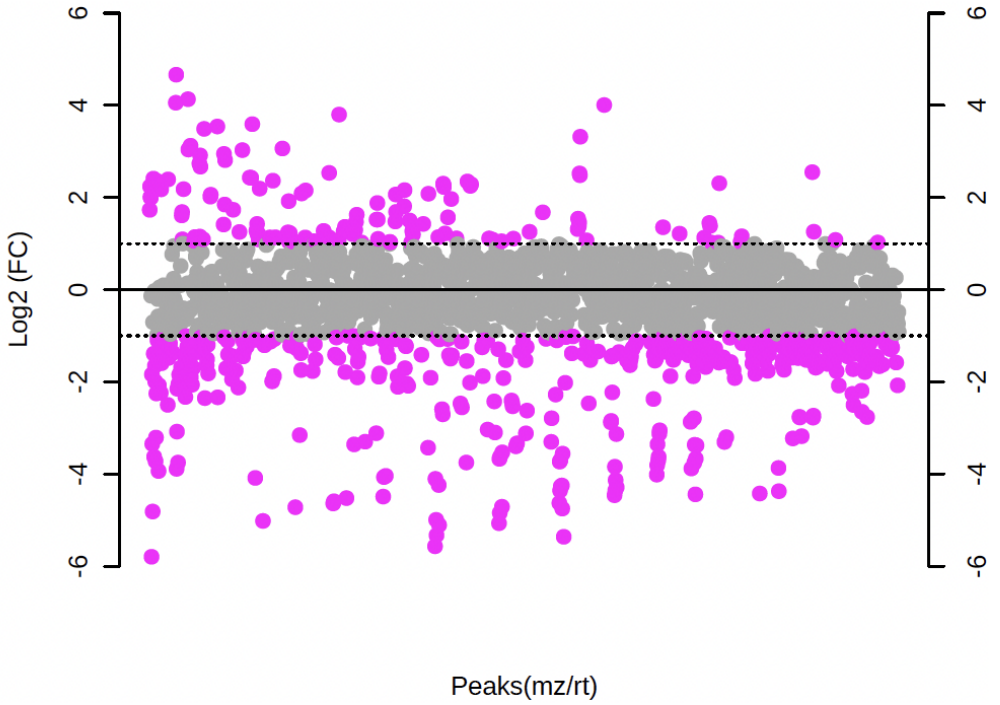

Figure B15. Fold change analysis.

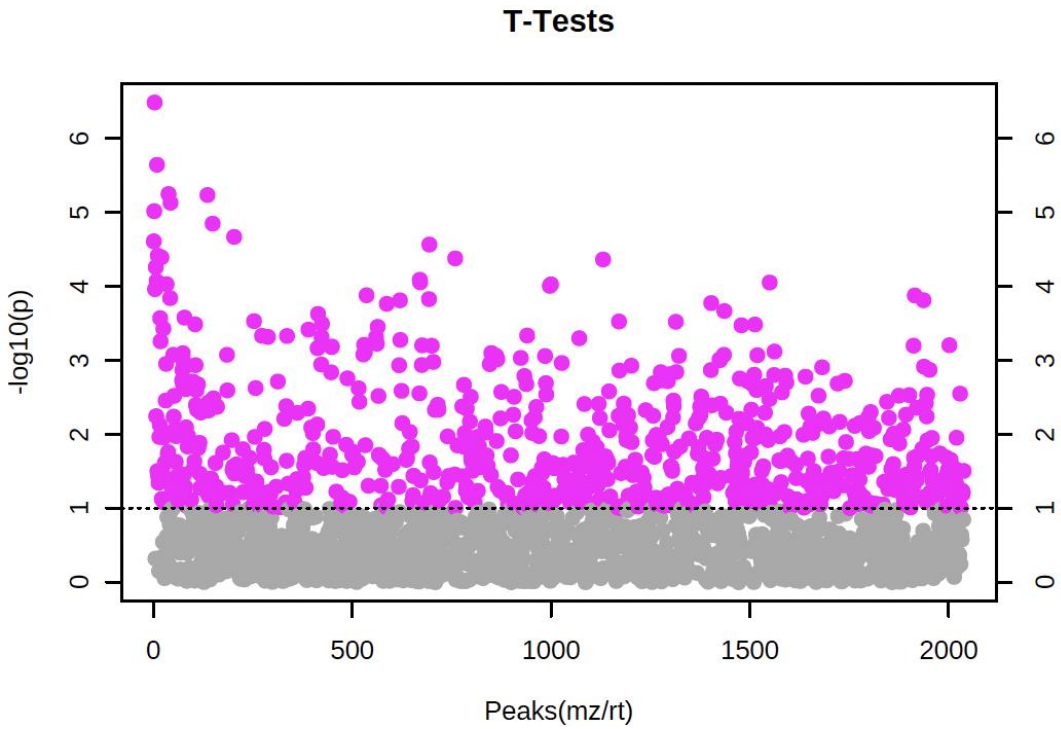

Figure B16. T-test results showing significantly different metabolites in magenta.

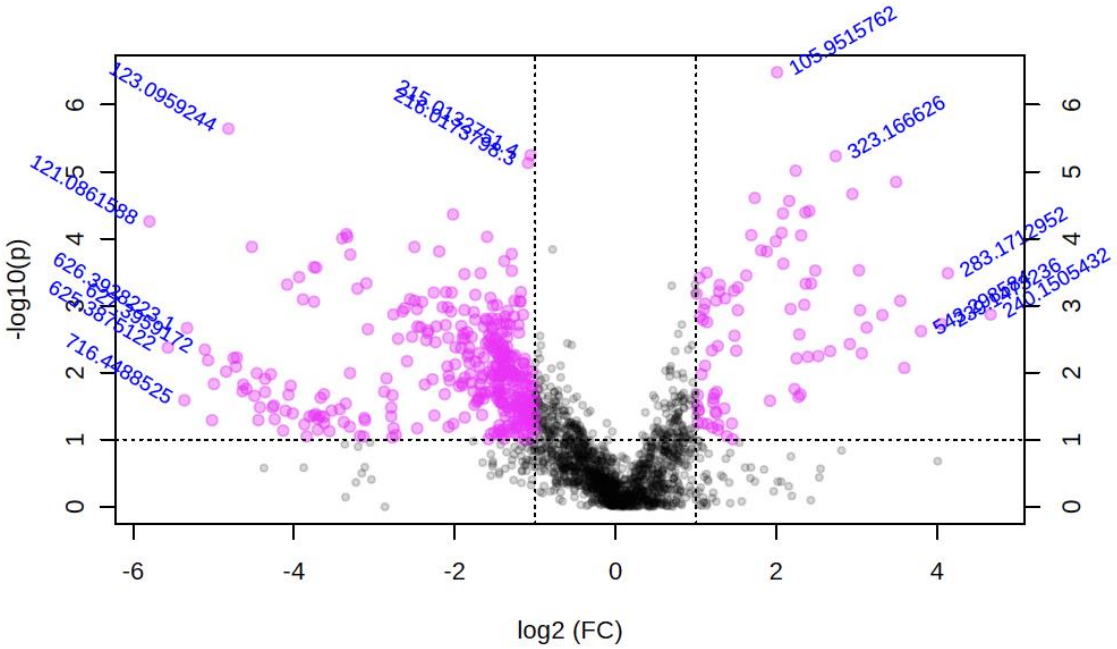

Figure B17. Volcano plot showing the up, and down regulated metabolites in magenta.

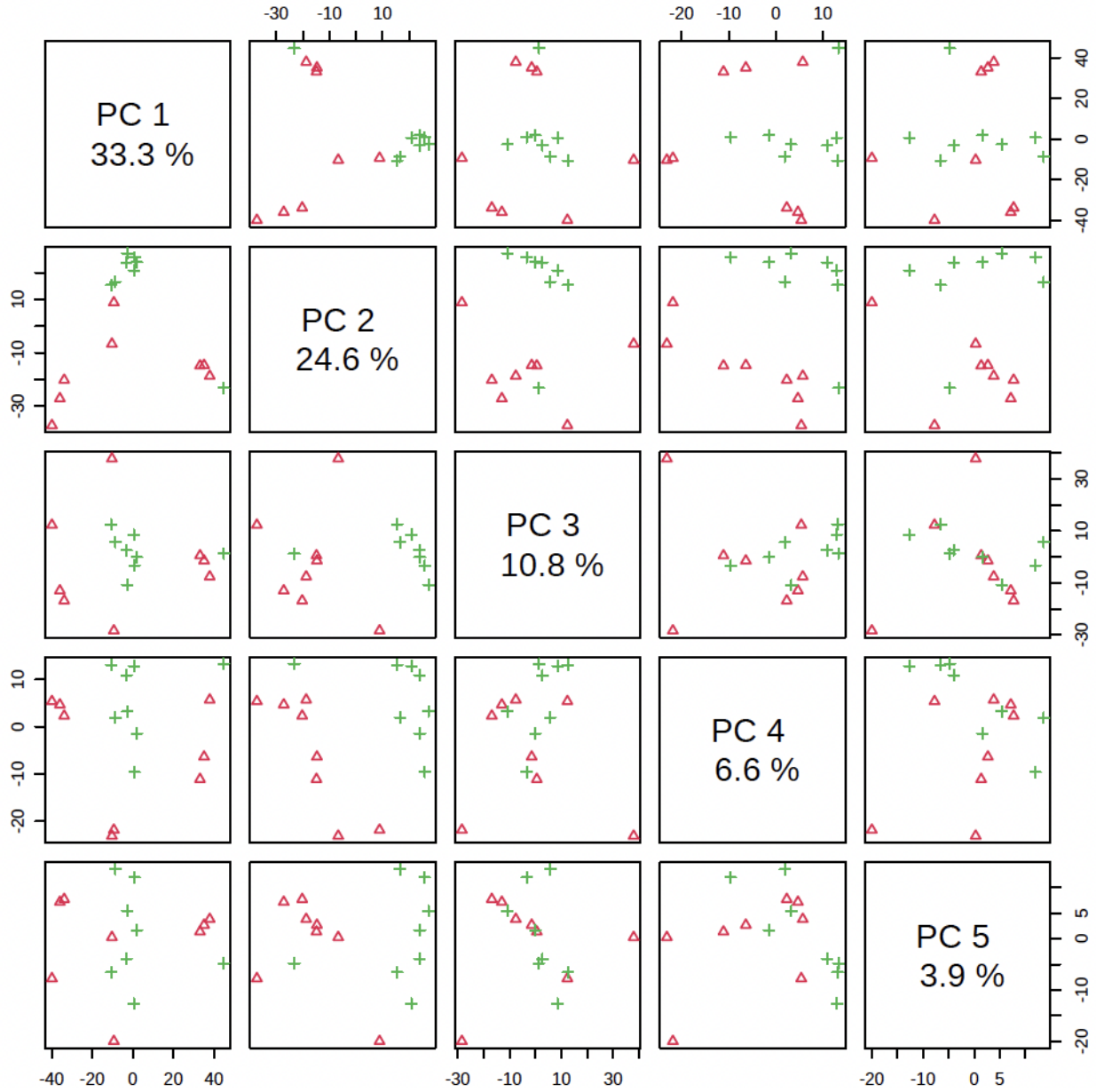

Figure B18. Pairs plot for principal component analysis

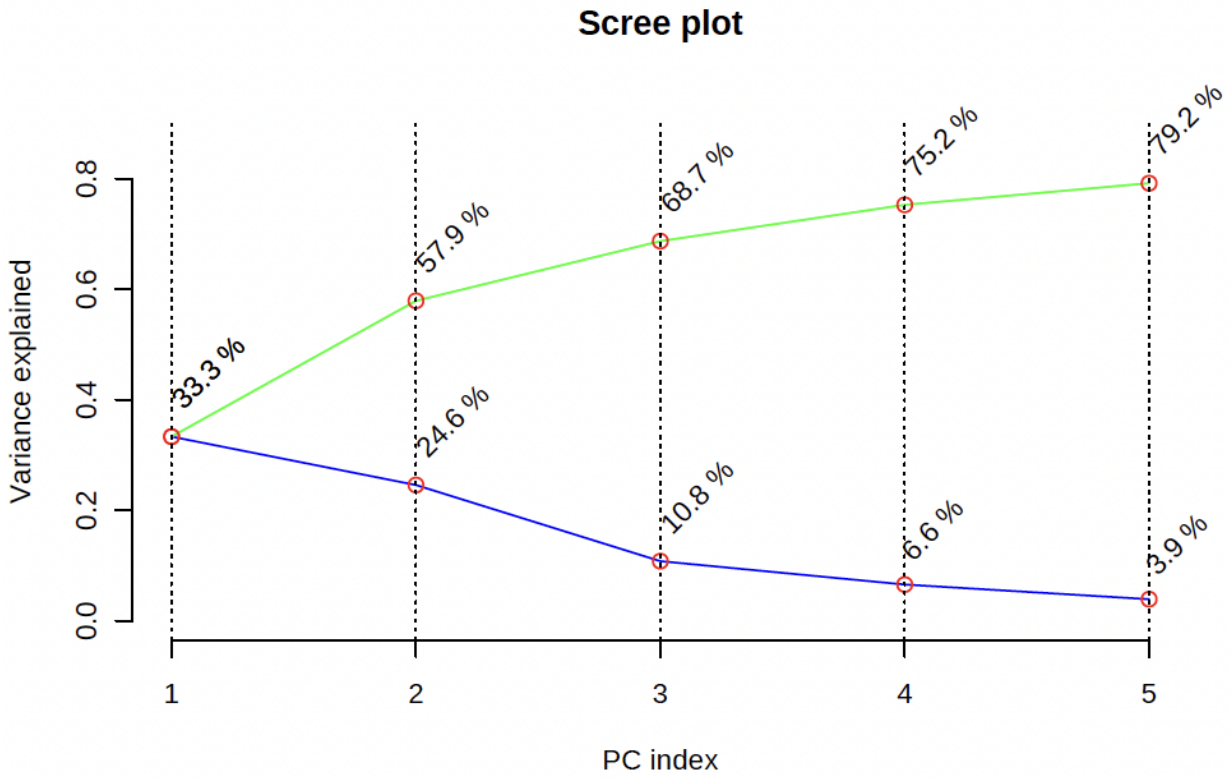

Figure B19. Scree plot from principal components analysis.

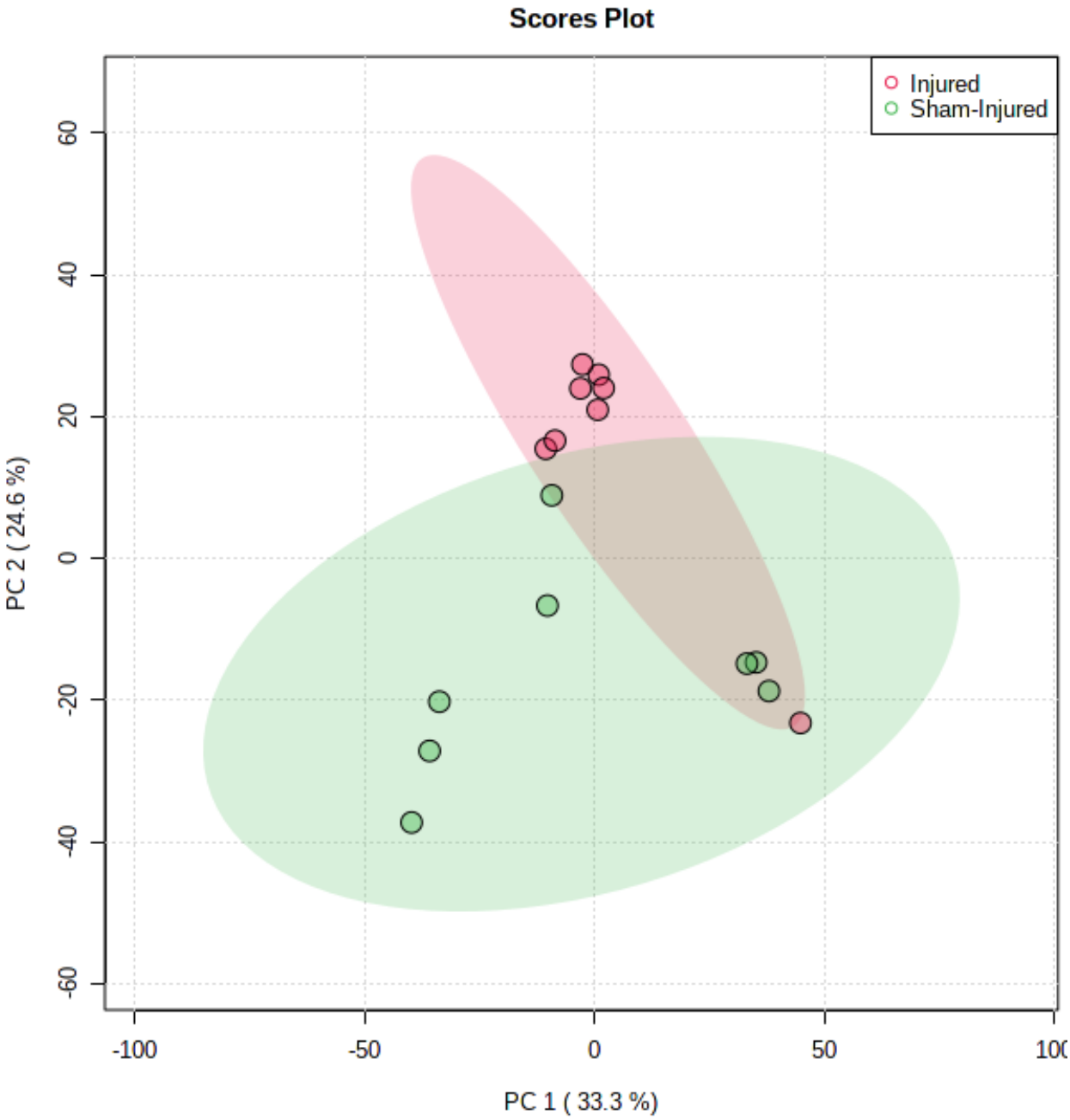

Figure B20. 2D scores plot for principal component analysis.

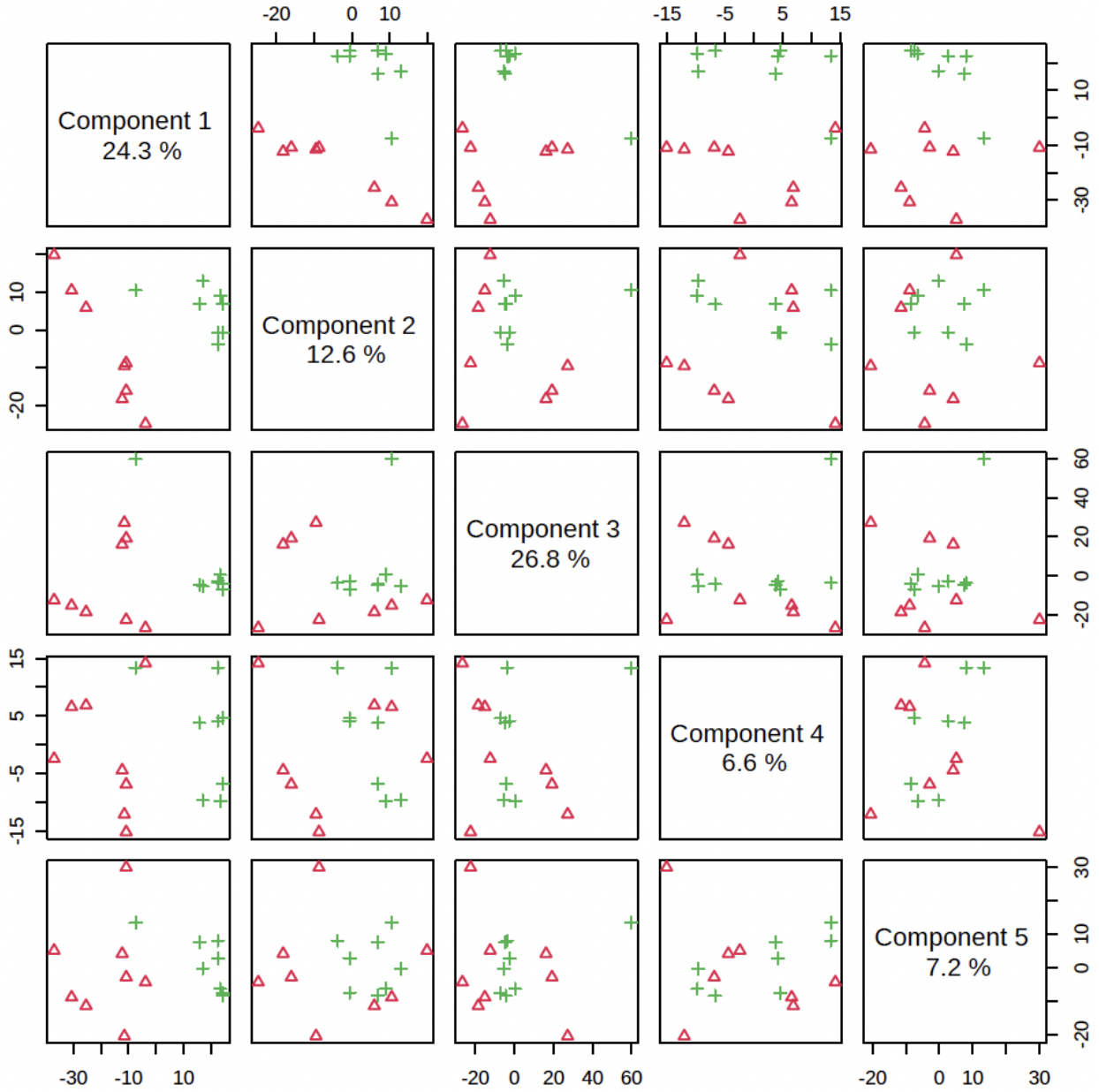

Figure B21. Pairs plot for partial least square – discriminant analysis.

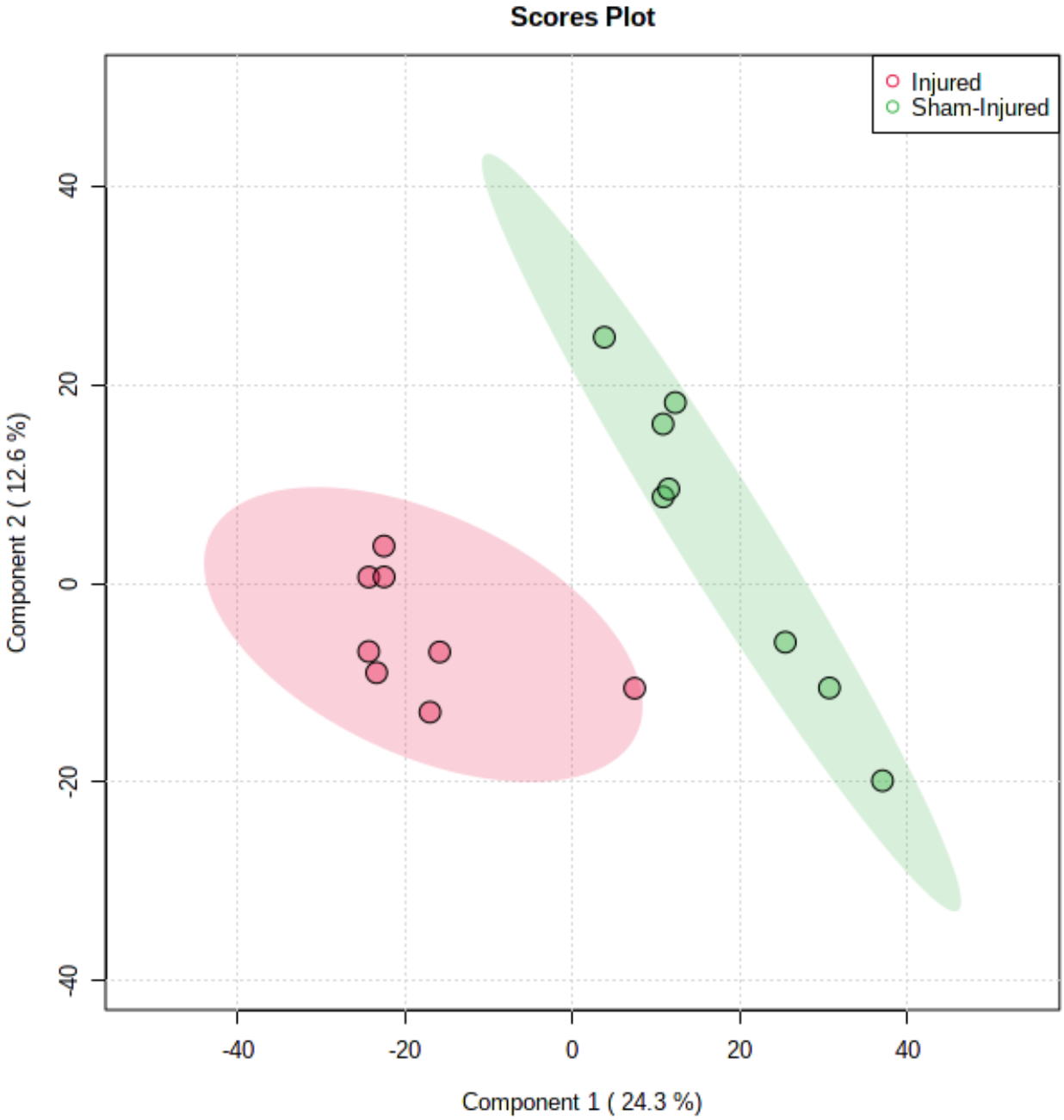

Figure B22. Partial least squares – discriminant analysis 2D scores plot.

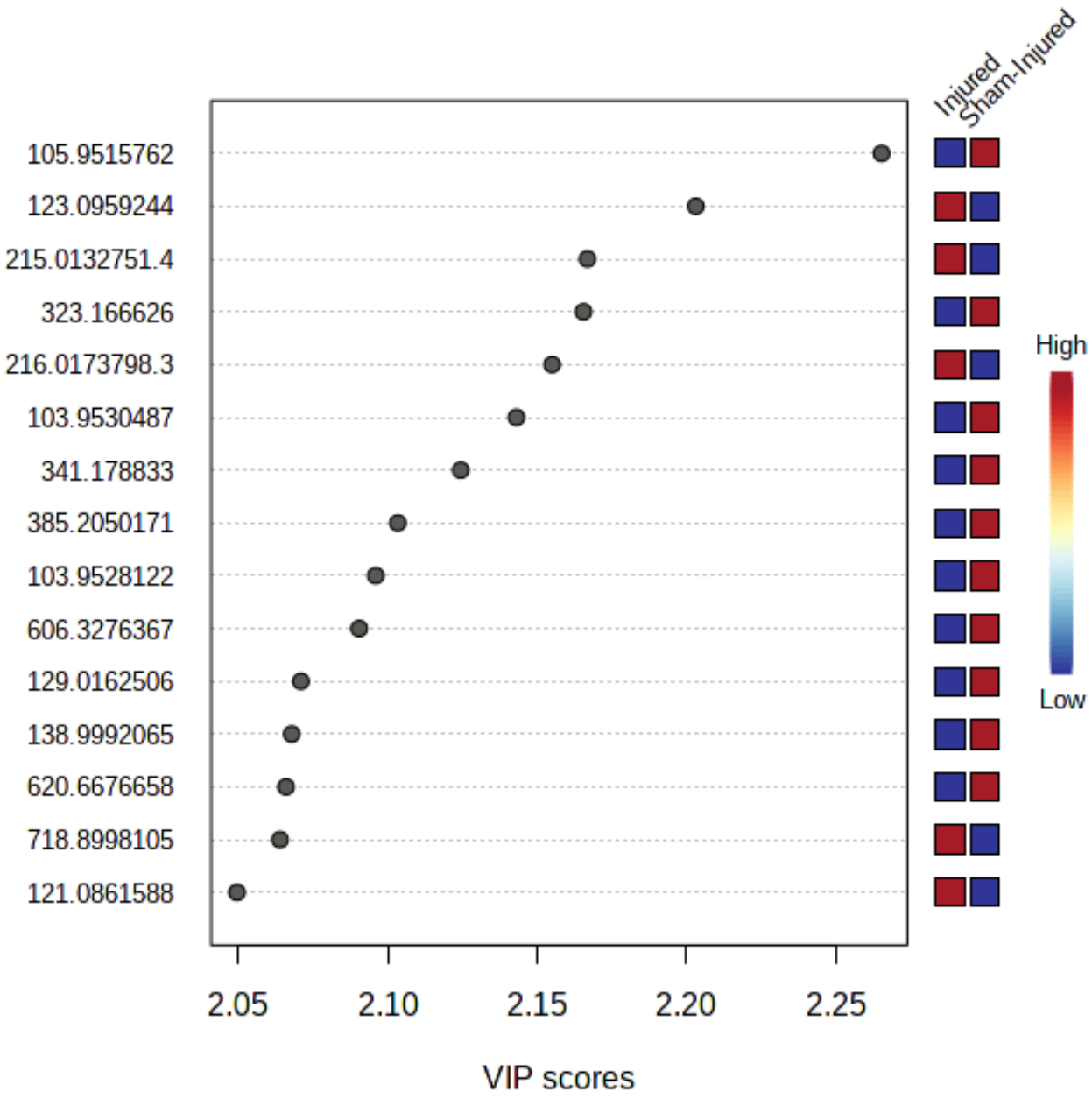

Figure B23. Partial least squares – discriminant analysis variable importance projections

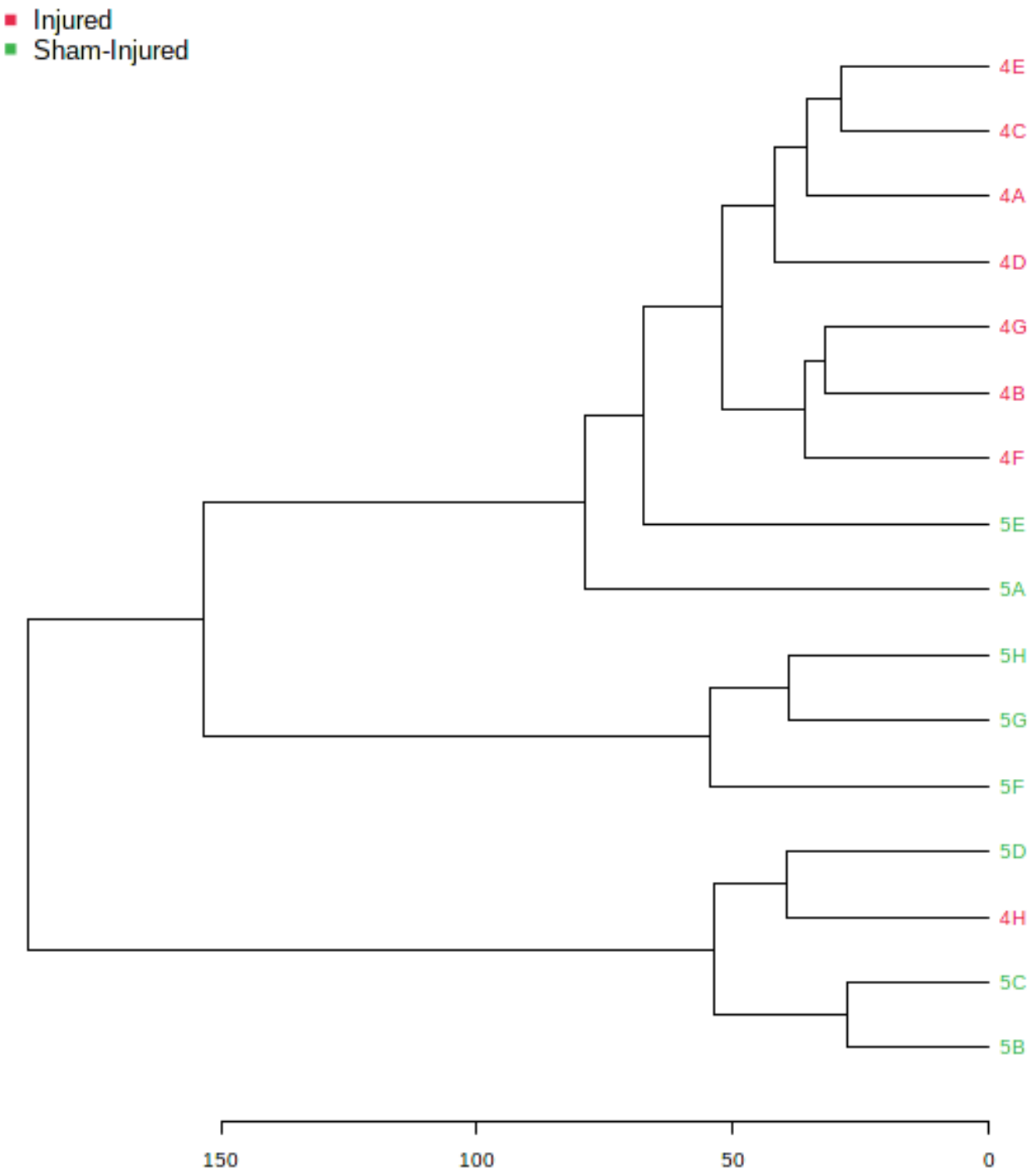

Figure B24. Hierarchical clustering of Sham-Injured v. Injured metabolic profiles.

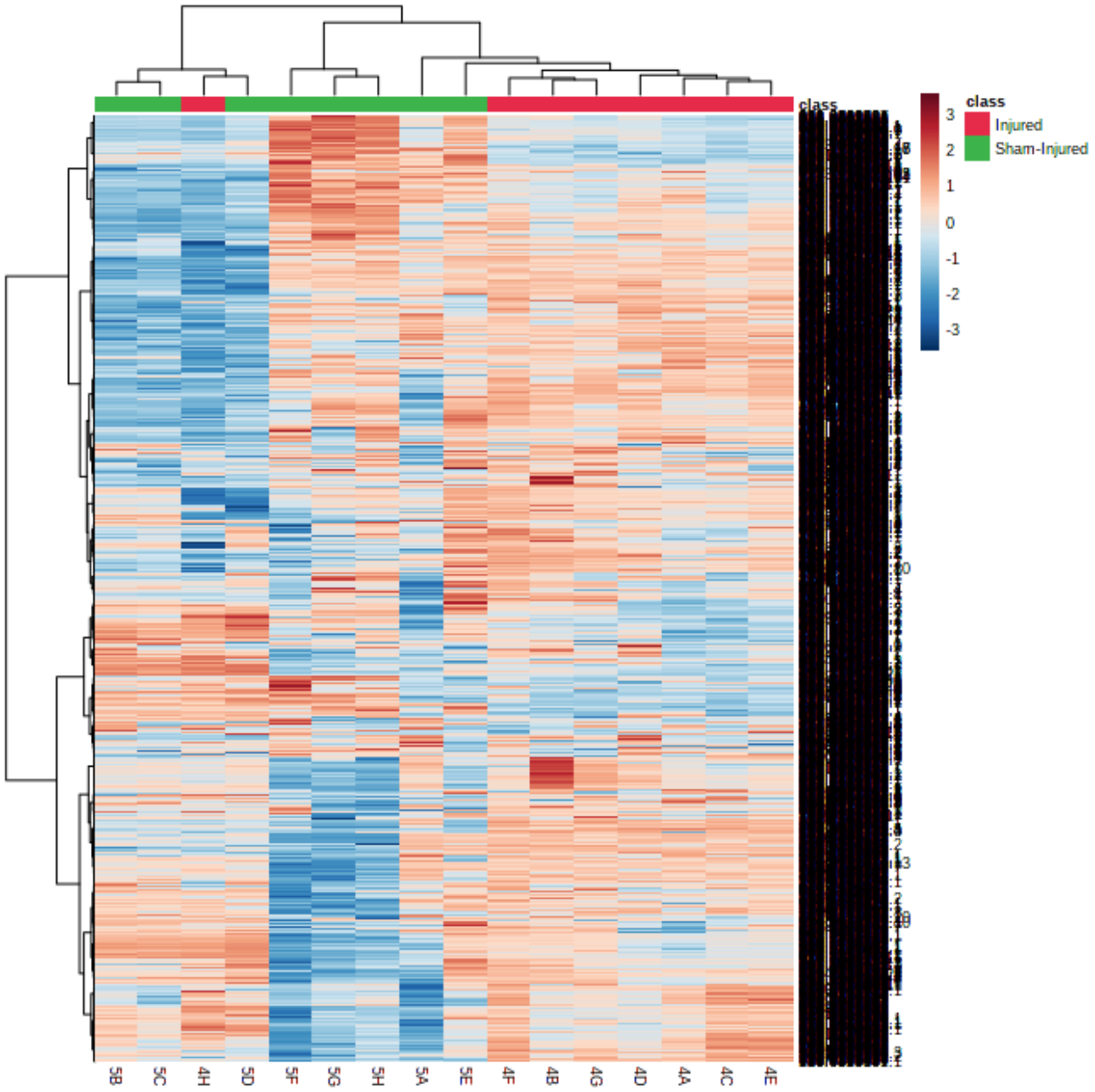

Figure B25. Clustergram of the hierarchical clustering.

Confidence Intervals for Injured v. Sham-Injured.

Confidence intervals were calculated by:

$$(\overline{X_1} - \overline{X_2}) \pm t^* \sqrt{\frac{s_1^2}{n_1} + \frac{s_2^2}{n_2}}$$

Where, $\overline{X_1}$ is mean intensity of m/z value for injured mice, $\overline{X_2}$ is mean intensity of m/z value for sham-injured mice, s_1^2 is the variance of the m/z value for injured mice, s_2^2 is the variance of the m/z value for sham-injured mice, and n_1 is the number of injured synovial fluid samples, and n_2 is the number of sham-injured synovial fluid samples.

The lower and upper limits of the confidence interval were then converted back to the original scale and can be interpreted as: ## times larger/smaller as the injured synovial fluid metabolite intensity.

Clustering Validation and Ensemble Clustering of Sham-Injured and Injured Metabolic Profiles

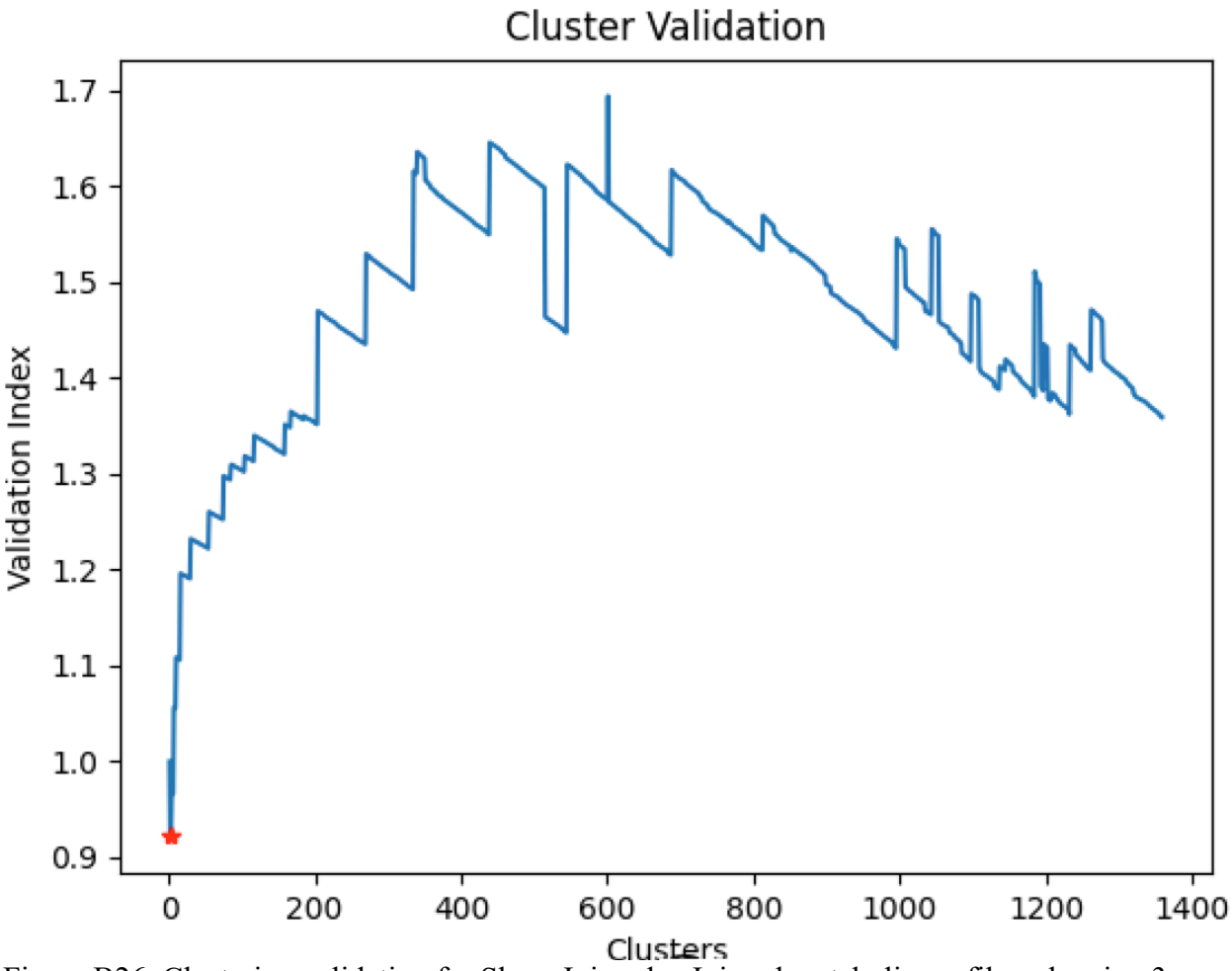

Figure B26. Clustering validation for Sham-Injured v. Injured metabolic profiles, showing 3 clusters is optimal.

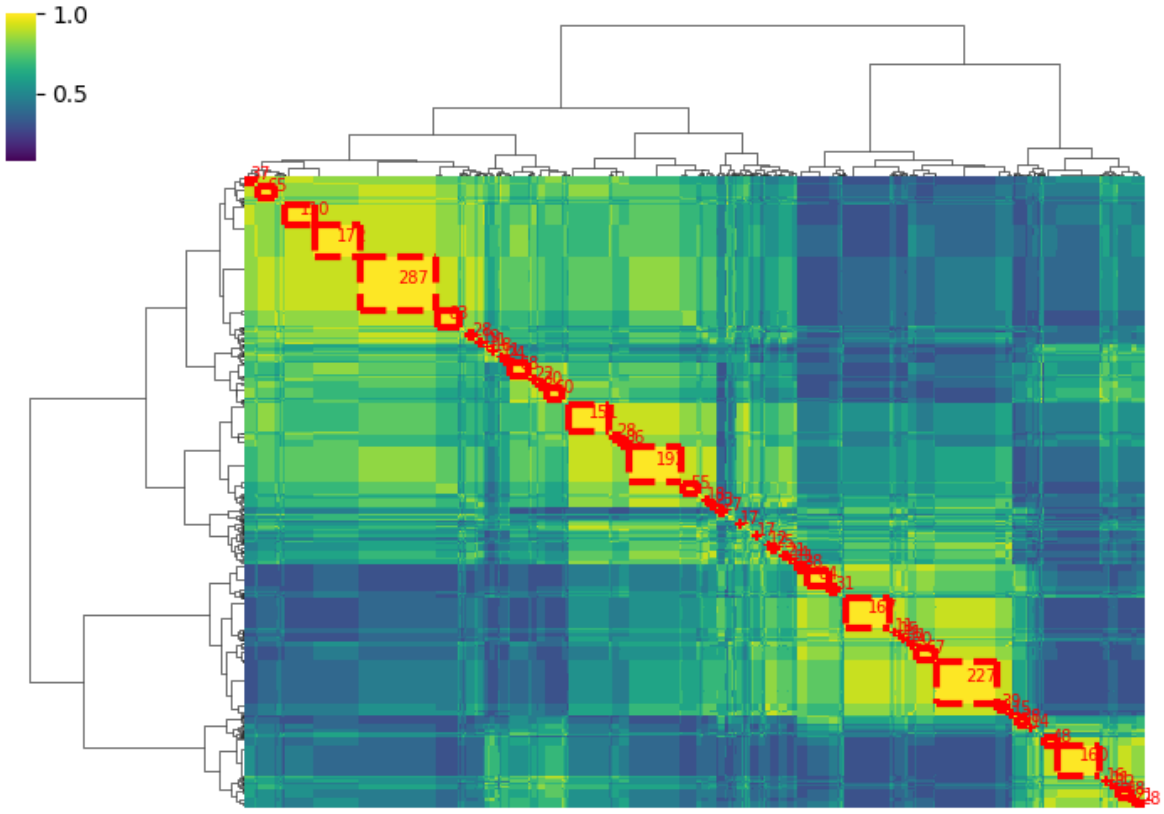

Figure B27. Ensemble clustering results for Sham-Inured and Injured synovial fluid data.

Contralateral-to-Injured & Injured Metabolomic Analysis

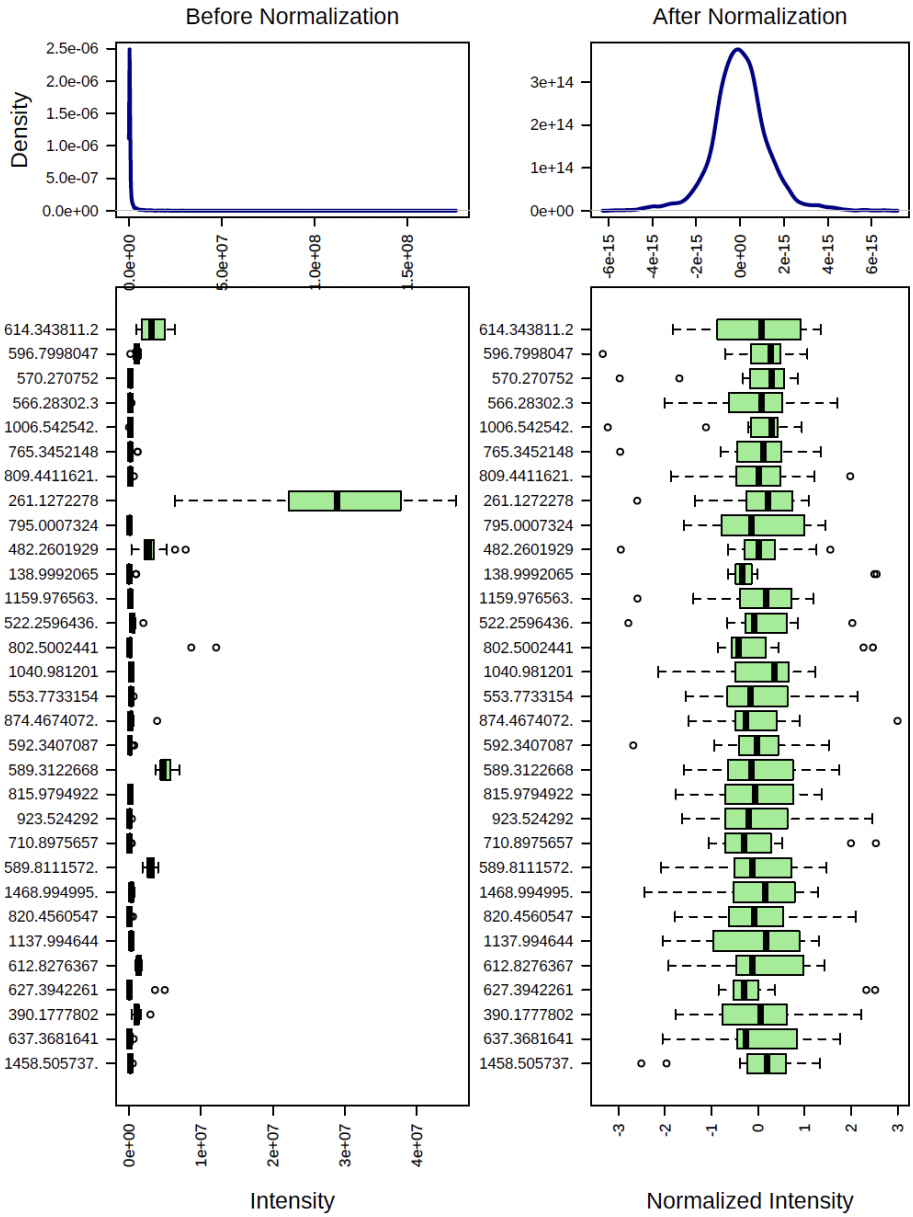

Figure B28. Normalization results for Contralateral-to-Injured metabolic data.

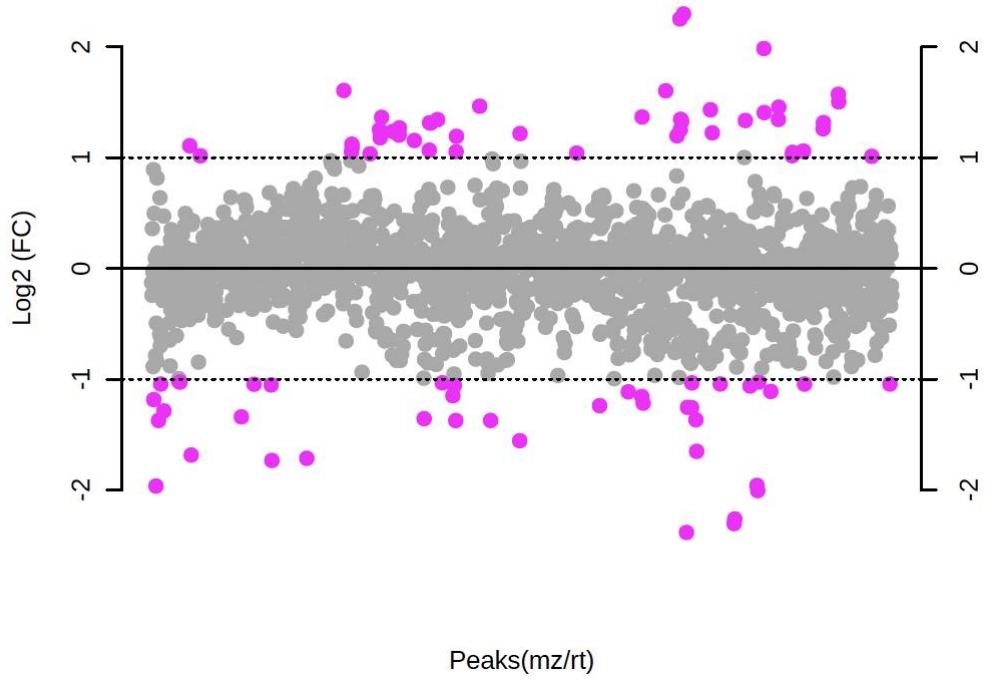

Figure B29. Fold change results.

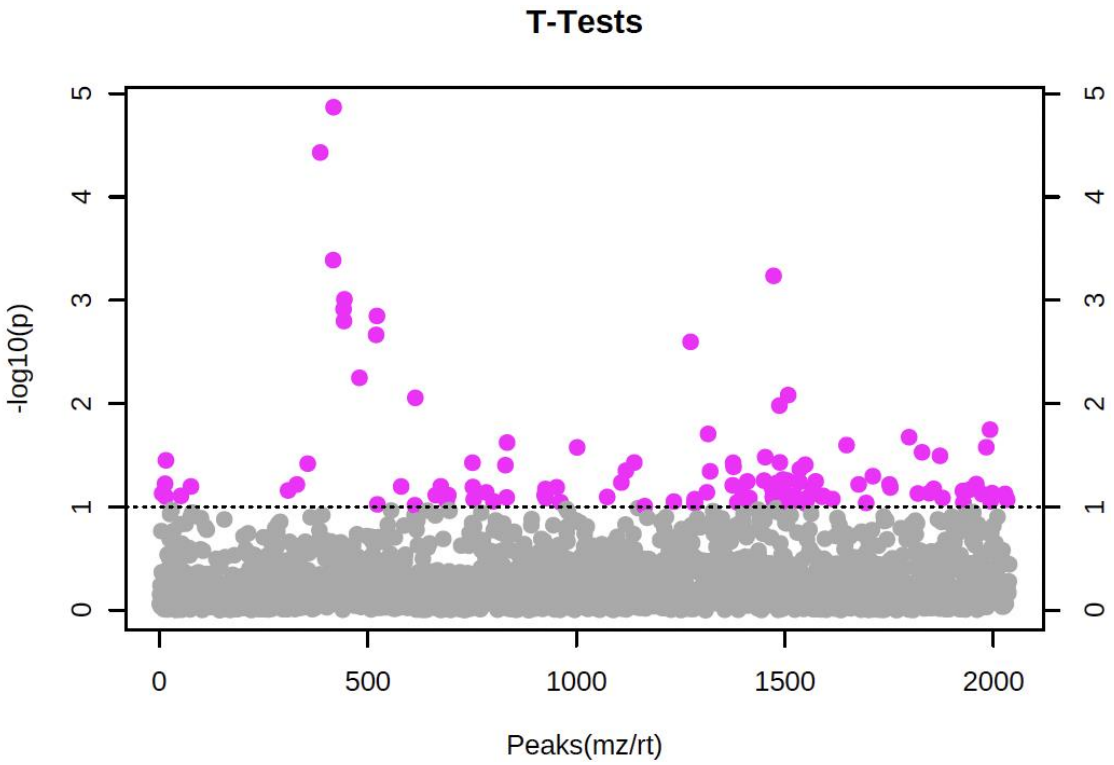

Figure B30. T-test results showing significant metabolites in magenta.

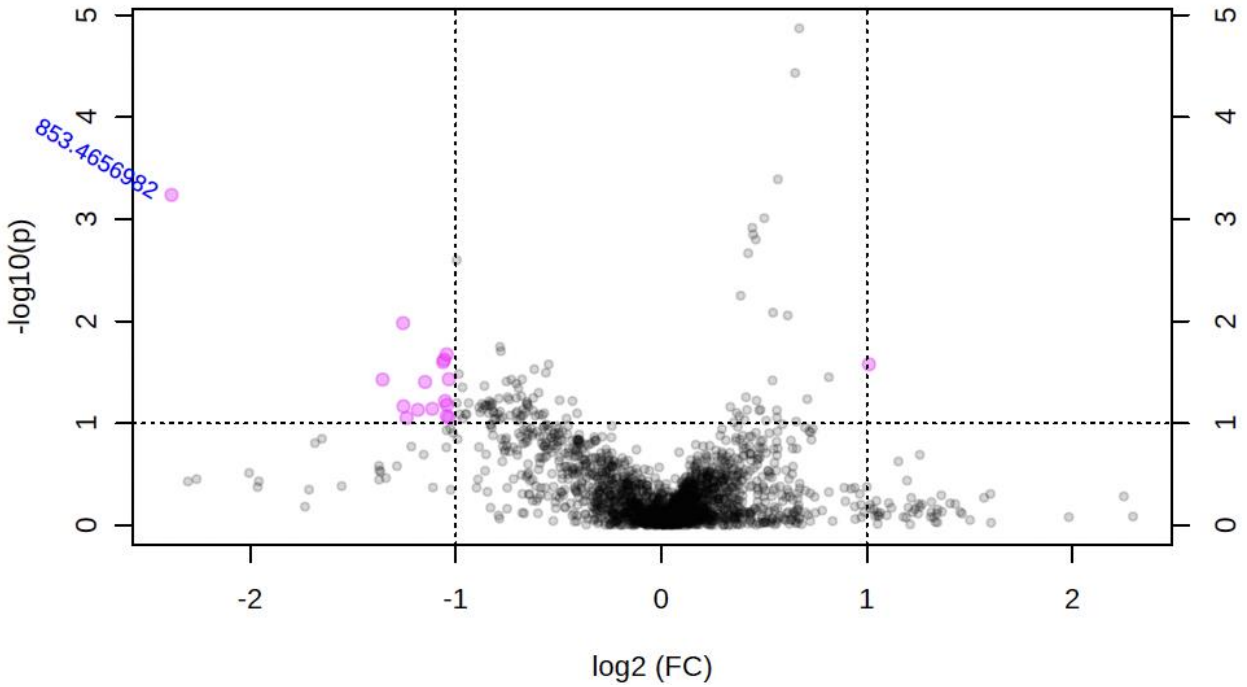

Figure B31. Volcano plot showing dysregulated metabolites in magenta

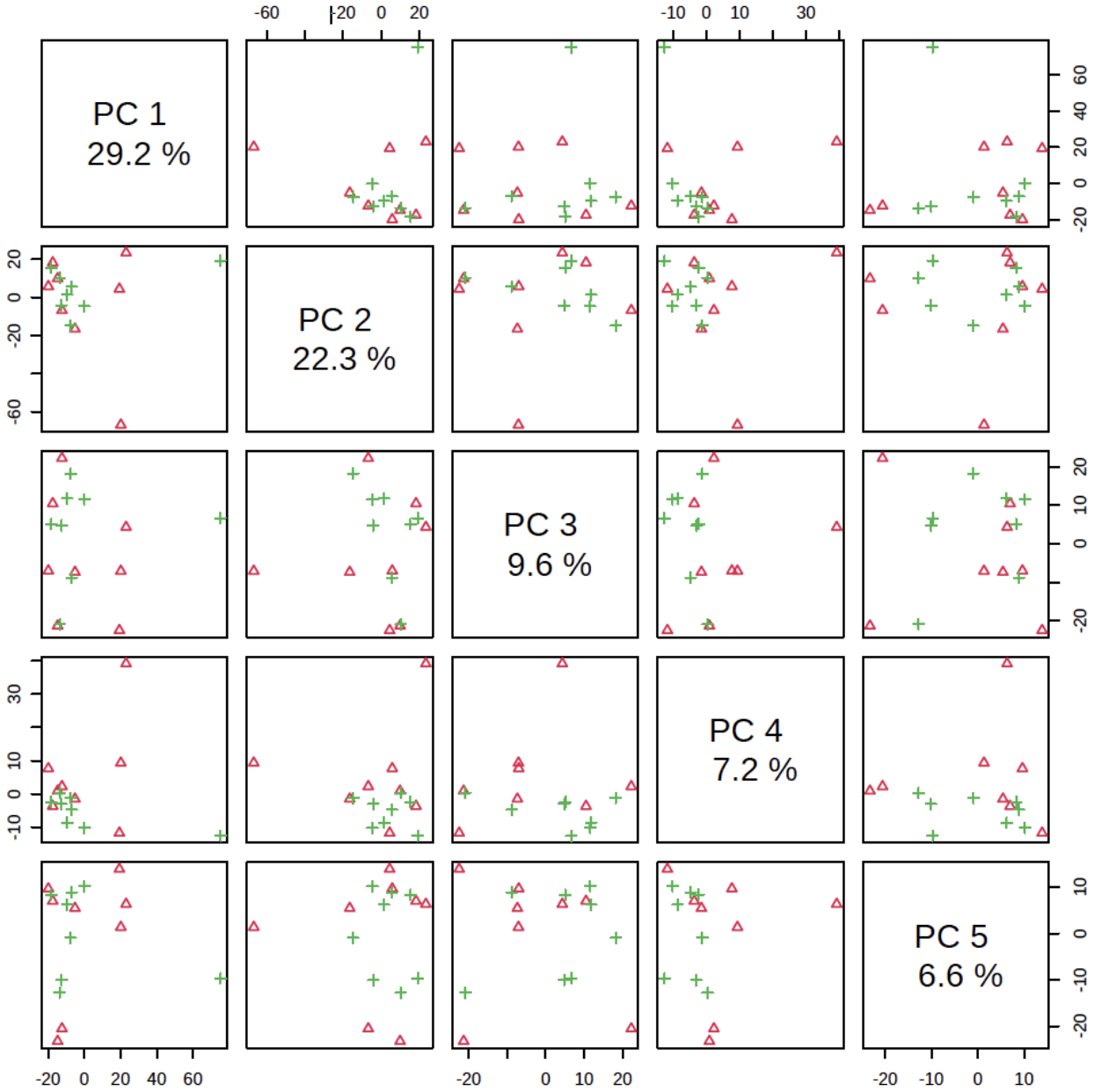

Figure B32. Principal component analysis pair plots

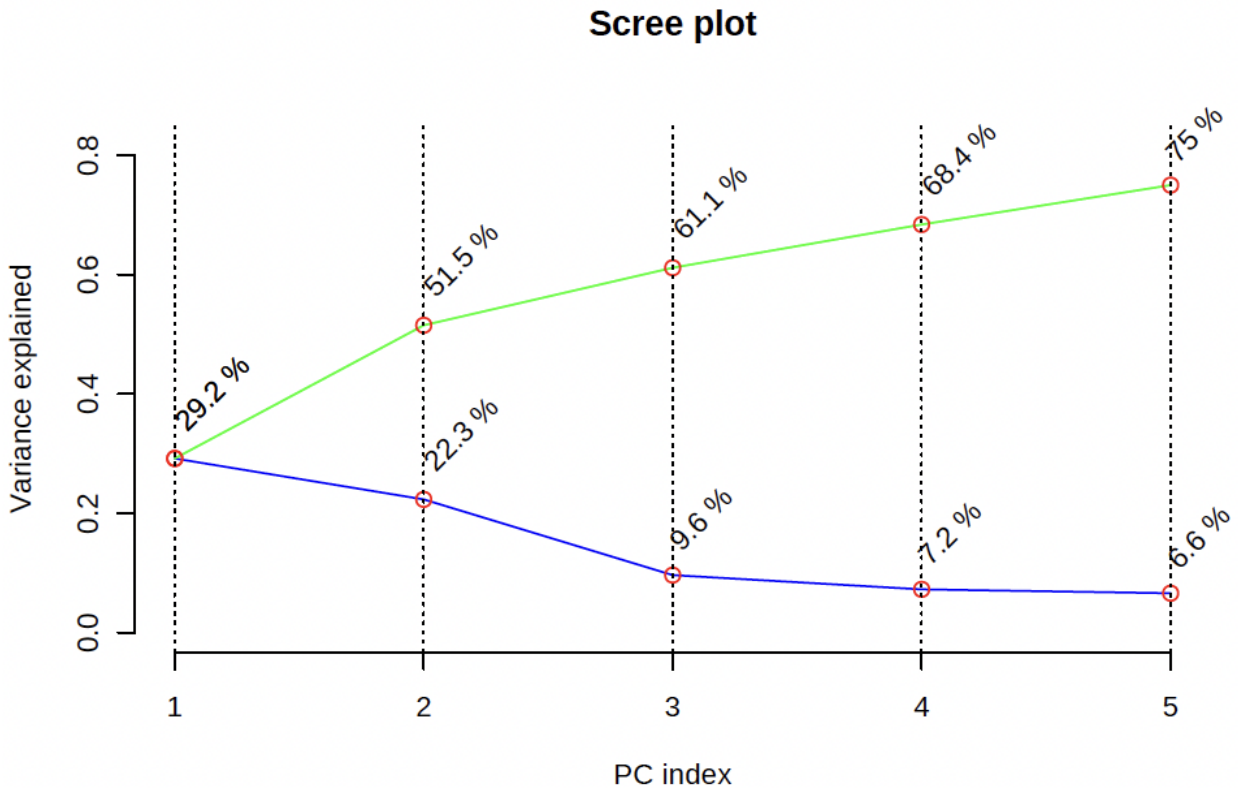

Figure B33. Principal components analysis scree plots

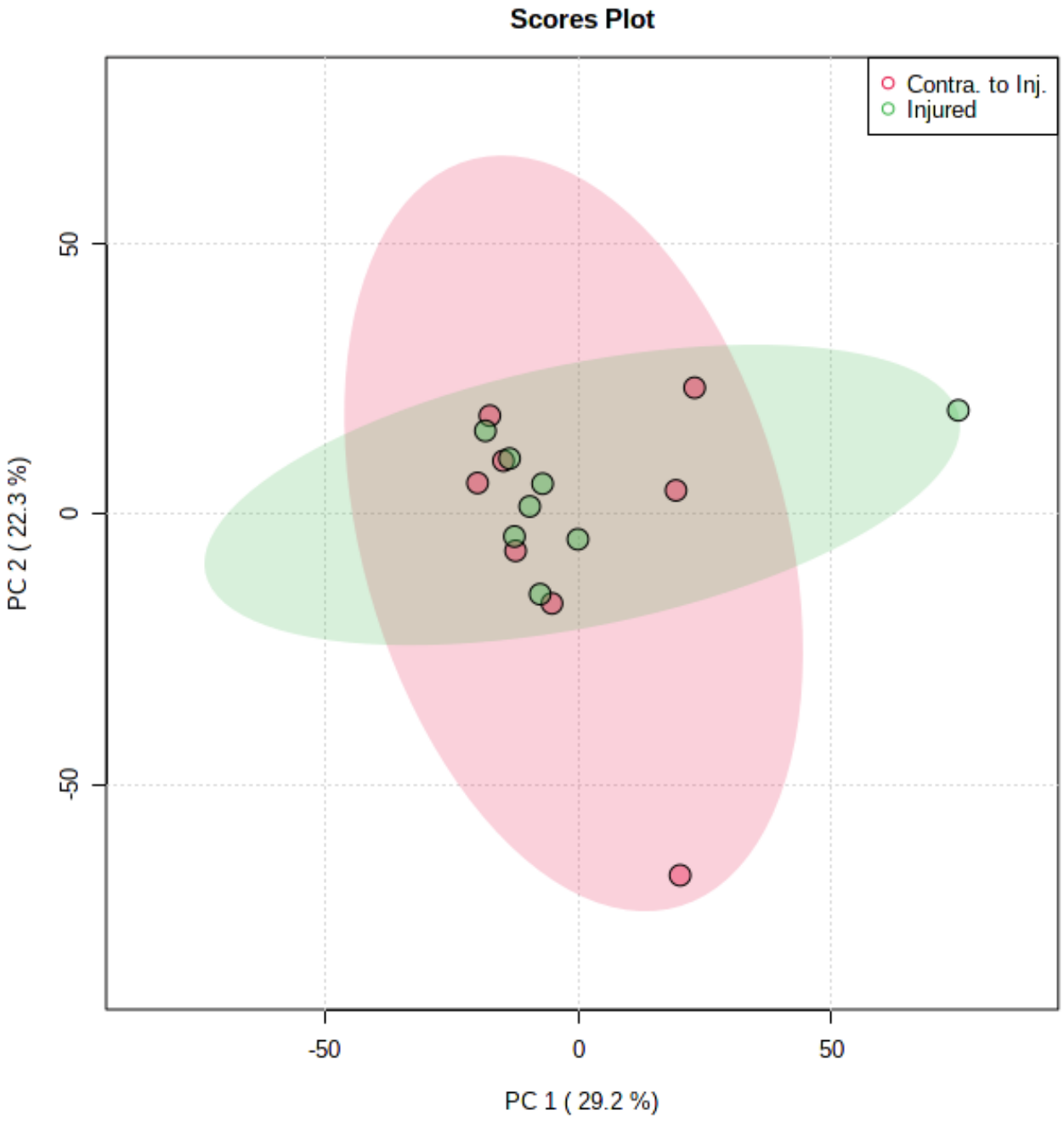

Figure B34. Principal components analysis 2D score plots.

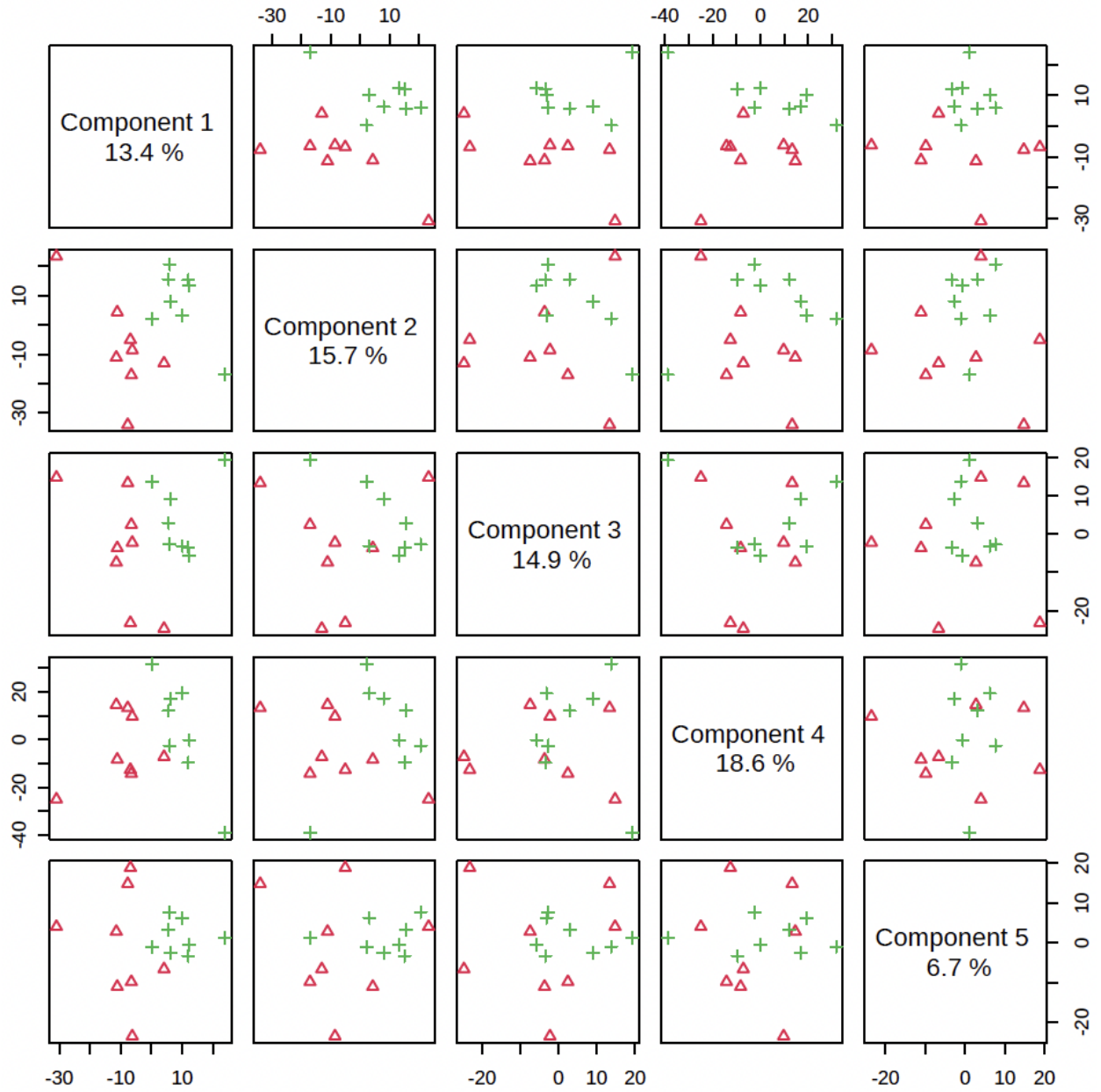

Figure B35. Partial least squares-discriminant analysis pairs plots

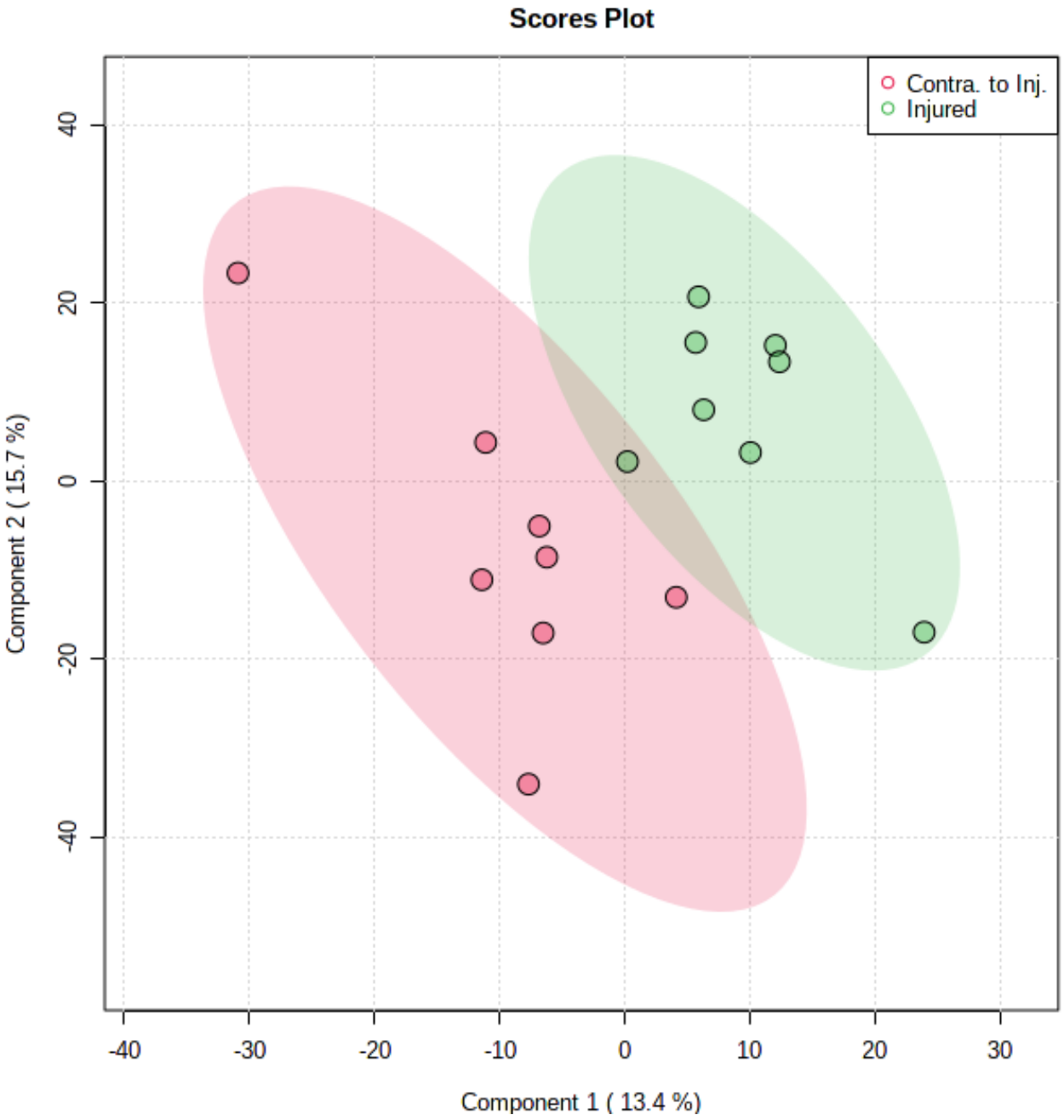

Figure B36. 2D scores plot

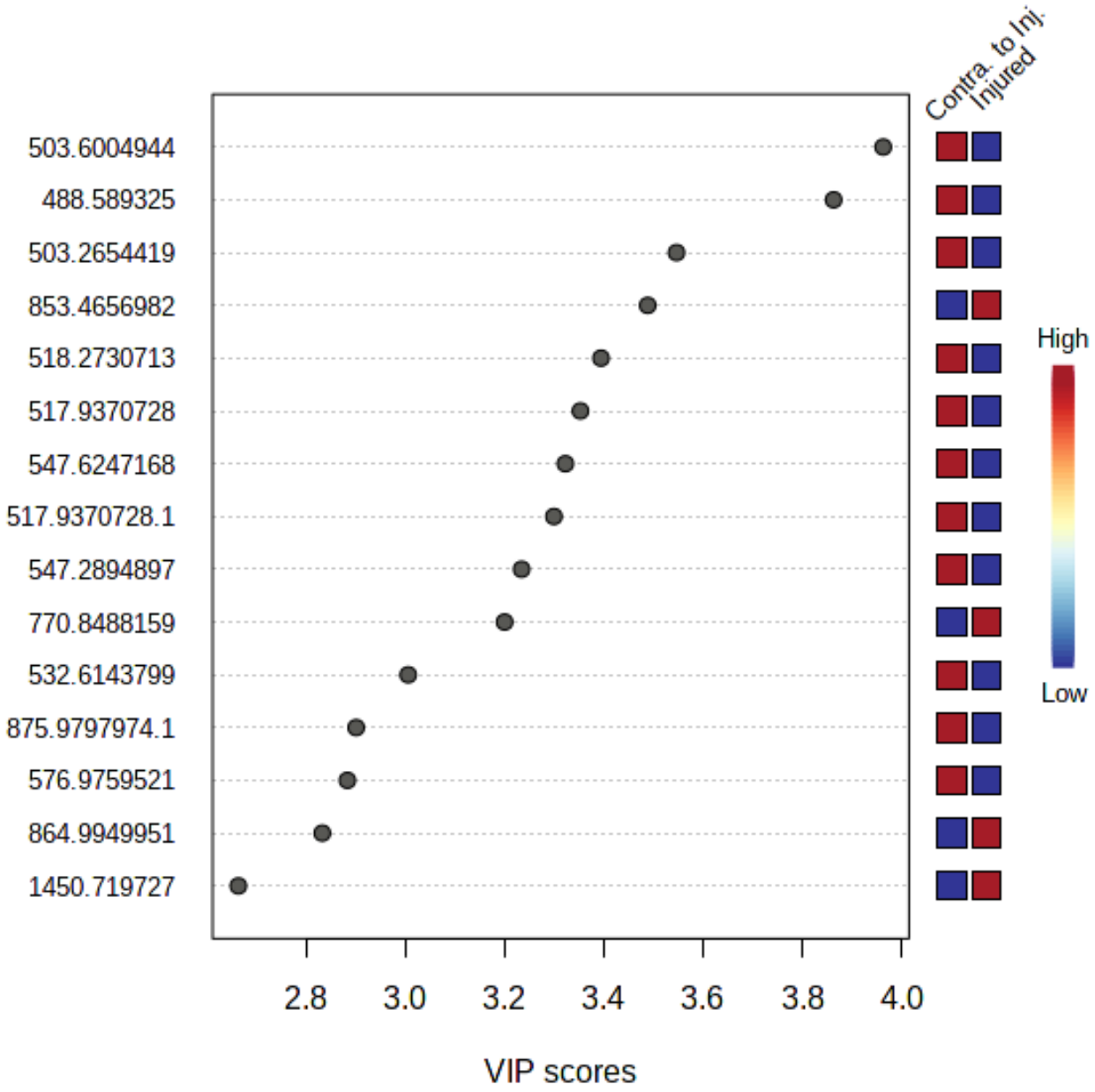

Figure B37. Partial least squares-discriminant analysis VIP scores

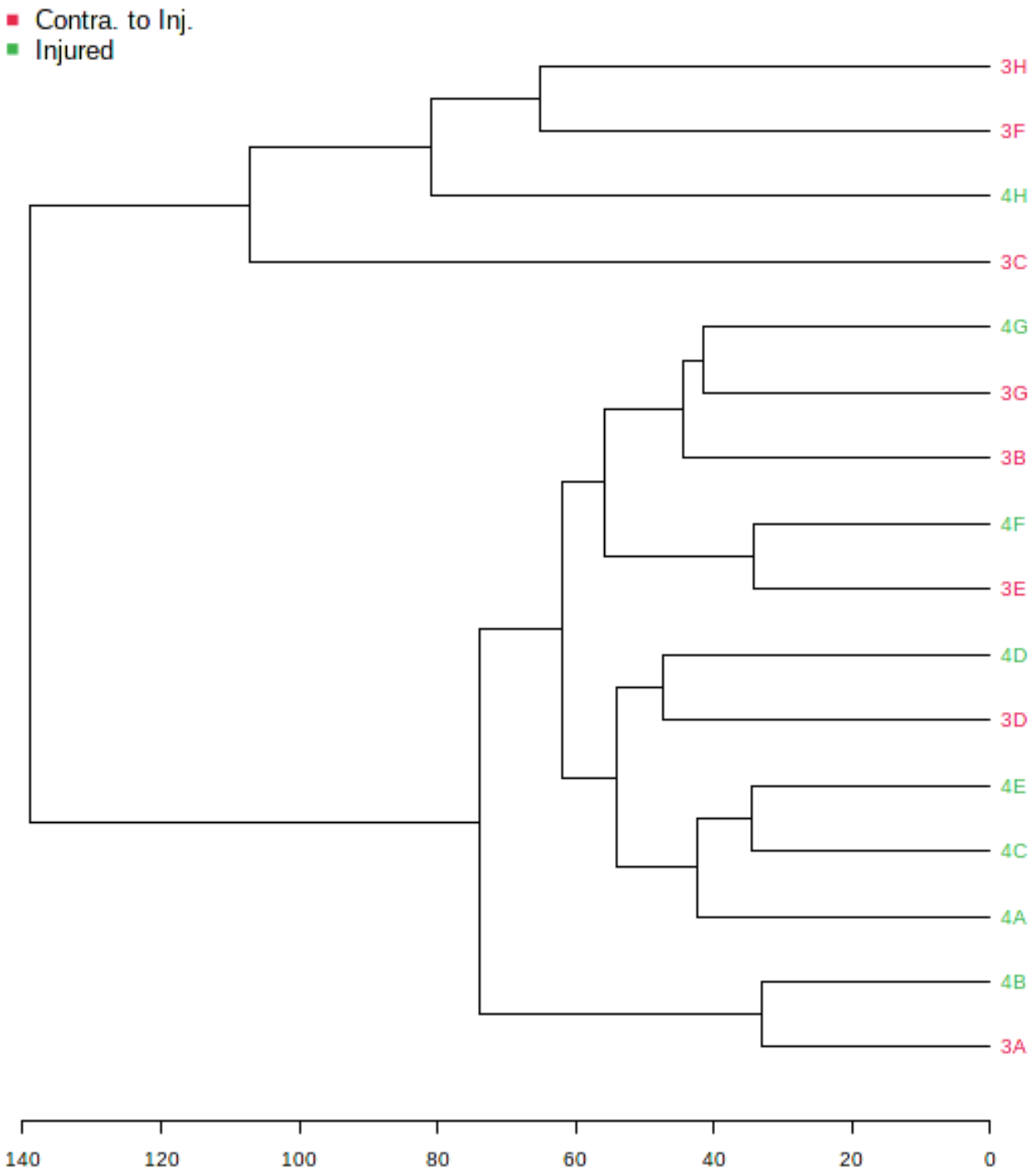

Figure B38. Dendrogram

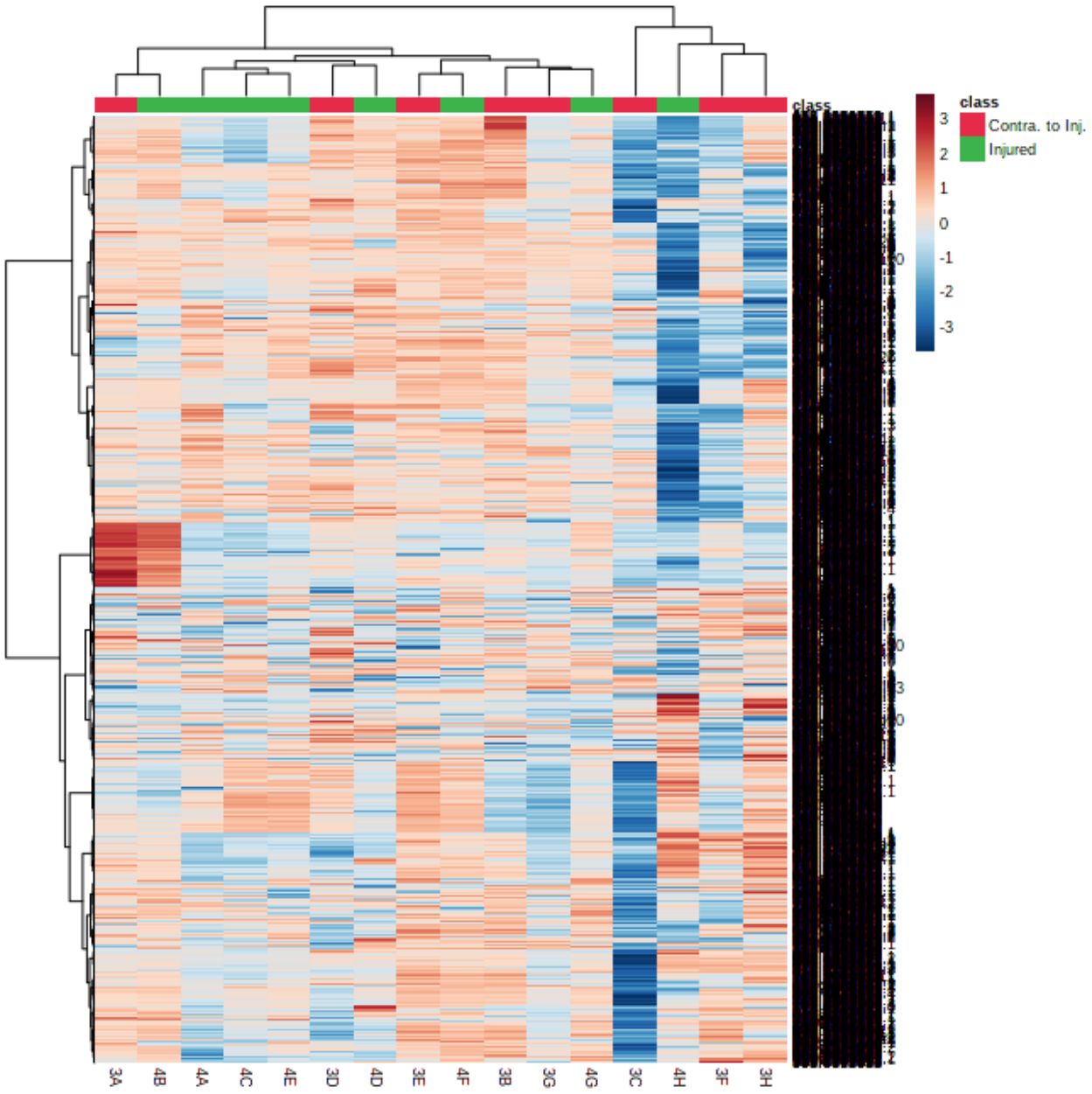

Figure B39. Clustergram

APPENDIX C

SUPPLEMENTARY MATERIALS FOR CHAPTER 5

Sample Harvest and Extraction

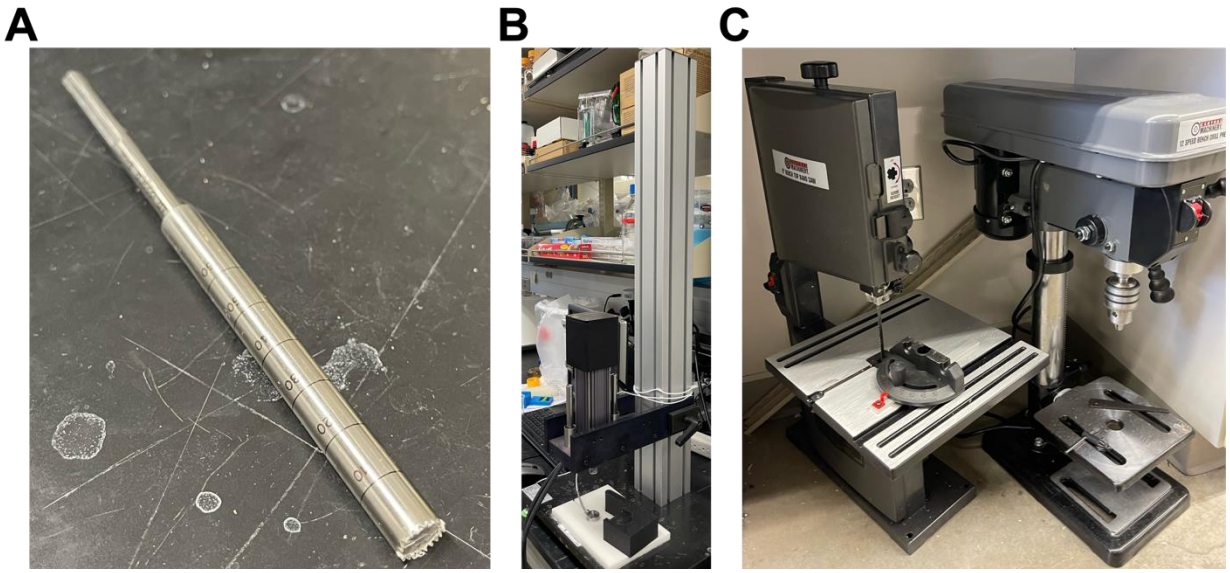

Figure C1 Machinery and tools used to extract cores A) Arthrex Osteochondral Autograft Transfer System, coring reamer B) Load frame used to cyclic compression, and pre-load only studies C) Central Machinery Bench Top band saw, (left), and Central Machinery, 12-speed bench drill press (right) used to extract the osteochondral cores.

Bioreactor Development

A two-chamber bioreactor was designed and manufactured for these studies (**Figure C1**). A 1.5”x1.5”x1-3/16” base with a 15/16” diameter (3/8” depth), and a threaded hole on bottom for attachment to the load cell. The top chamber of the bioreactor is separated by a 1/32” rubber sheet of 1.5”x1.5”x1/32” from the base and includes four vertical through holes to secure the two chambers, as well as two horizontal through-holes (separated by 90°) to circulate fluid during experimental runs. Two identical bioreactors were manufactured using polysulfone (McMaster-Carr, Elmhurst, IL USA). The bioreactors included shims in both chambers to match fluid volumes (~2mL). The shim in the bottom chamber (*i.e.,* bone fluid chamber) was 3D printed with a ~7mm hole at ~2.4mm in depth, allowing for the press fit of the bone side of

osteochondral samples. Control experiments were performed with an impermeable 8mm diameter aluminum cylinder to test for leakage between the bottom and top chambers.

Confocal Imaging Studies

After injecting 2mL of 13μM Dextran into the bone chamber, the injection port was sealed. A peristaltic pump attached to the upper fluid chamber, and 2mL of neat PBS added to cartilage chamber. For pure-diffusion studies the bioreactor was placed into a 3D printed holder, a timer started, and the pump started. For cyclic compression studies the bioreactor was attached to the load cell, pre-loaded (3.5N, ~70kPa) with encoder position recorded to set the 0% strain position. After which the pump was started in tandem with the cyclic compression. Upon completion osteochondral cores were removed from bioreactors, and the cartilage was removed from the osteochondral core using a razor blade. The disc of cartilage was halved, and one half was placed into a custom-built sample holder. Samples were Saran-wrapped to preserve hydration ahead of confocal imaging. Confocal imaging was done immediately after experiments finished. The custom-built sample holder was placed into a custom-built jig, that separated the cartilage sample from the water immersion using a glass cover slip. Samples were imaged on an upright CLSM, using a 10X water immersion objective. After placing the sample holding device into the machine and locating the cartilage surface, we utilized two lasers of 488nm and 595 nm with emission windows of 500-585nm (488nm laser), and 602-720nm (595nm laser), respectively. For the 595 nm laser we used a 75% laser intensity. The 488nm laser excited the calcein embedded within an epoxy component of the confocal sample holder. Three sets of z-stacks were taken, with one at each radial edge, and one at the midline of the tissue.

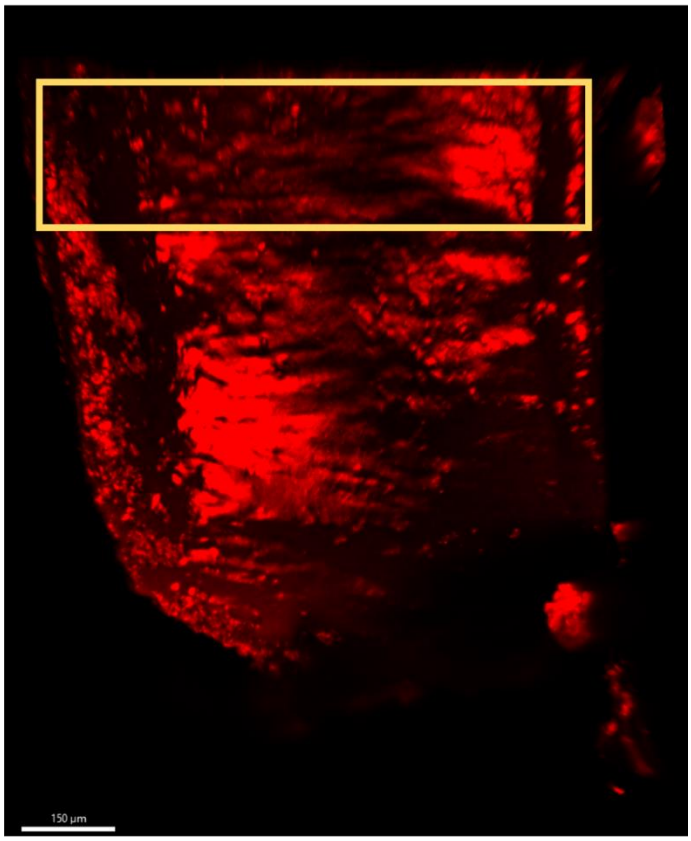

Figure C2 Selection of ROI that avoids curvature of articular surface allowing for depth measurements.

Confocal Imaging Analysis

After imaging, the z-stacks were analyzed using Imaris 9.8 (Bitplane). The cartilage surface tilted to varying degrees for some samples. Thus, we rotated the z-stacks to ensure consistent measurement locations relative to the surface. After rotation, we the maximum intensity projection (MIP) was prepared for each z-stack. The MIPs were analyzed using a custom Matlab script. Briefly, the images were rotated so the articular surface was aligned with the x-axis, and a region of interest was selected (see example below). Using this region of interest, we calculated the mean fluorescence intensity per normalized distance increment (0 to 1, where 1 is the

articular surface). From these data we determined the maximum intensity, normalized distance corresponding to the maximum intensity, mean and median intensities of each sample.

Statistical Analysis: Analysis of Imaging Parameters

Maximum intensity, normalized distance corresponding to the maximum intensity, mean and median intensities at 15, 30, 60, and 120 minutes were analyzed using mixed model analysis of variance (ANOVA). Fixed effects for maximum intensity, mean and median intensity include strain magnitude (no-loading, 5% mean strain, 10% mean strain), time-point (15, 30, 60, 120 minutes), sample location (radial edges, and mid-line). The random effects included location of femur where core was extracted and the specimen. The model included interactions between fixed effects. Mean, and median intensities of each sample were natural log-transformed to meet assumptions of ANOVA. For normalized distance corresponding to the maximum intensity we analyzed each strain magnitude separately, as the full mixed model did not meet assumptions of ANOVA. Fixed effects were imaging location, and time points. Random effects were specimenID and location.

Results from Statistics on Imaging Data Parameters

Maximum Intensity

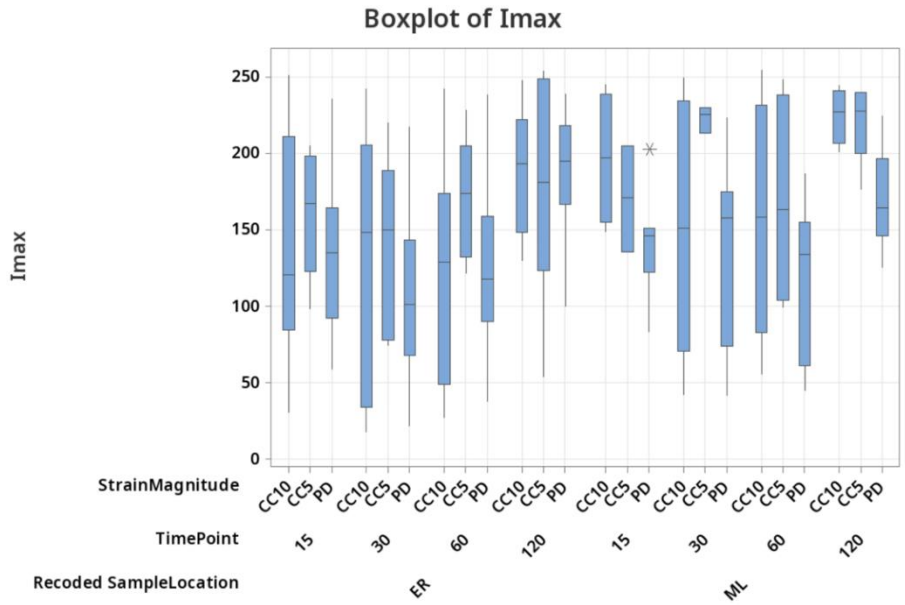

Figure C3 Box plots of the maximum intensity for each group considered in our analyses.

Variance Components

Source	Var	% of Total	SE Var	Z-Value	P-Value
specimanID	168.435113	5.29%	158.020299	1.065908	0.143
Location	207.571783	6.52%	184.877167	1.122755	0.131
Error	2805.355886	88.18%	311.634953	9.002058	0.000
Total	3181.362782				

-2 Log likelihood = 2052.327110

Tests of Fixed Effects

Term	DF Num	DF Den	F-Value	P-Value
Recoded SampleLocation	1.00	162.07	8.56	0.004
StrainMagnitude	2.00	119.55	7.18	0.001
TimePoint	3.00	173.49	5.76	0.001
Recoded SampleLocation*StrainMagnitude	2.00	162.07	2.11	0.125
Recoded SampleLocation*TimePoint	3.00	162.07	0.73	0.534
StrainMagnitude*TimePoint	6.00	166.41	0.41	0.873
Recoded SampleLocation*StrainMagnitude*TimePoint	6.00	162.07	0.69	0.654

Figure C4 Results from our mixed-model ANOVA with dependent variable of maximum intensity from imaging studies.

Tukey Simultaneous Tests for Differences of Means

Difference of StrainMagnitude Levels	Difference of Means	SE of Difference	DF	Simultaneous 95% CI	T-Value	Adjusted P-Value
CC5 - CC10	7.4	14.2	73.688	(-26.2, 41.0)	0.52	0.860
PD - CC10	-28.2	10.7	155.862	(-53.5, -2.8)	-2.63	0.026
PD - CC5	-35.6	11.3	164.142	(-62.4, -8.7)	-3.14	0.006

Tukey Simultaneous Tests for Differences of Means

Difference of TimePoint Levels	Difference of Means	SE of Difference	DF	Simultaneous 95% CI	T-Value	Adjusted P-Value
30 - 15	-8.4	13.3	177.239	(-43.0, 26.2)	-0.63	0.922
60 - 15	-17.5	13.2	171.739	(-51.6, 16.7)	-1.33	0.546
120 - 15	31.2	13.1	172.737	(-2.9, 65.3)	2.37	0.087
60 - 30	-9.1	12.9	168.988	(-42.5, 24.4)	-0.70	0.895
120 - 30	39.6	13.0	177.866	(5.9, 73.2)	3.05	0.014
120 - 60	48.6	12.3	174.020	(16.6, 80.7)	3.94	0.001

Tukey Simultaneous Tests for Differences of Means

Difference of Recoded SampleLocation Levels	Difference of Means	SE of Difference	DF	Simultaneous 95% CI	T-Value	Adjusted P-Value
ML - ER	24.91	8.52	162.074	(8.10, 41.73)	2.93	0.004

Individual confidence level = 95.00%

Figure C5 Simple main effect comparisons for significant effect imaging location, strain magnitude and time point, respectively.

Distance Corresponding to Maximum Intensity

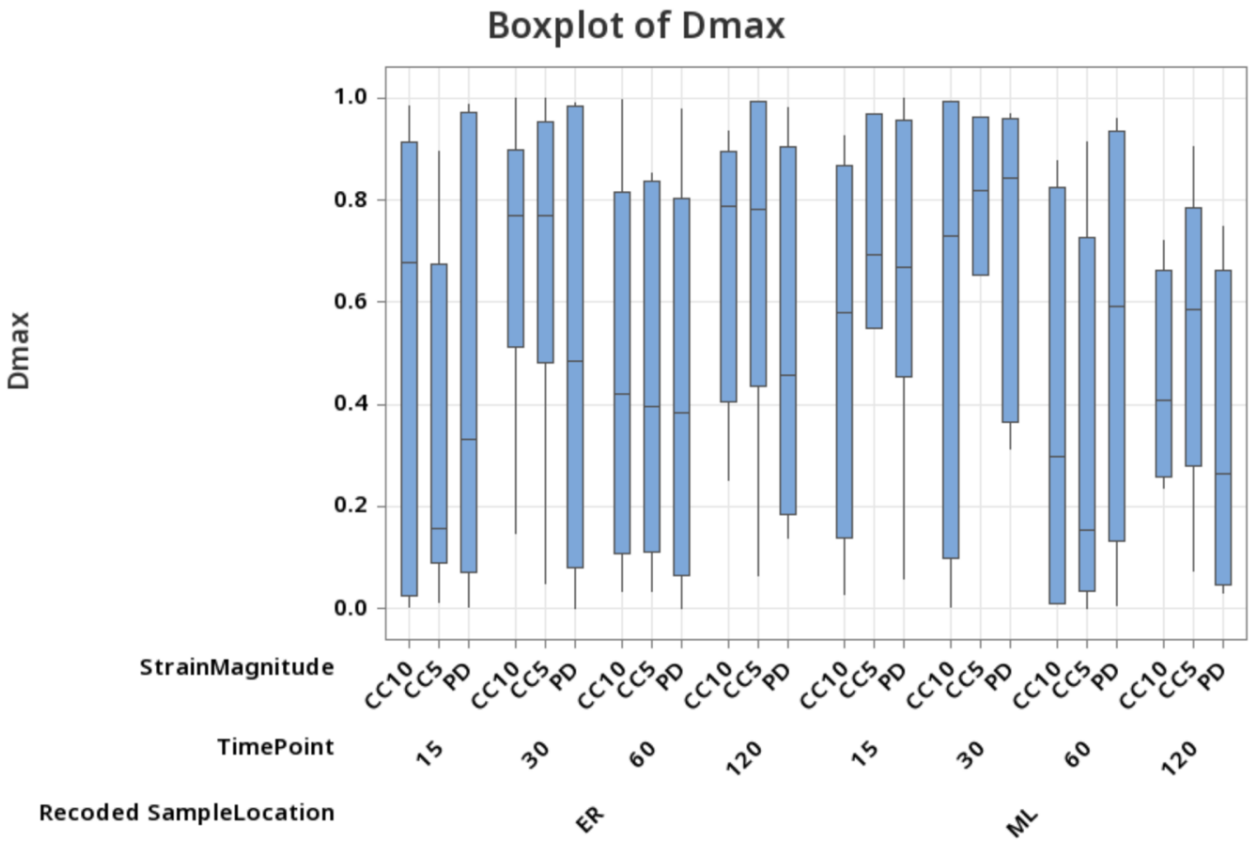

Figure C6 Boxplots of the normalized distance (Dmax) of the maximum intensity in the imaging experiments.

Group: Pure Diffusion

Variance Components

Source	Var	% of Total	SE Var	Z-Value	P-Value
specimanID	0.006667	4.85%	0.009322	0.715156	0.237
Location	0.001992	1.45%	0.010500	0.189746	0.425
Error	0.128673	93.69%	0.020293	6.340809	0.000
Total	0.137332				

-2 Log likelihood = 112.405926

Tests of Fixed Effects

Term	DF Num	DF Den	F-Value	P-Value
Recoded SampleLocation	1.00	80.41	0.56	0.458
TimePoint	3.00	34.07	0.78	0.514
Recoded SampleLocation*TimePoint	3.00	80.41	1.40	0.249

Group: CC5

Variance Components

Source	Var	% of Total	SE Var	Z-Value	P-Value
specimanID	0.000000	0.00%	*	*	*
Location	0.003431	3.05%	0.015300	0.224250	0.411
Error	0.108945	96.95%	0.027941	3.899121	0.000
Total	0.112376				

-2 Log likelihood = 48.161296

Tests of Fixed Effects

Term	DF Num	DF Den	F-Value	P-Value
Recoded SampleLocation	1.00	30.41	0.31	0.580
TimePoint	3.00	20.36	1.75	0.188
Recoded SampleLocation*TimePoint	3.00	30.41	1.52	0.228

Group: CC10

Variance Components

Source	Var	% of Total	SE Var	Z-Value	P-Value
specimanID	0.000000	0.00%	*	*	*
Location	0.000000	0.00%	*	*	*
Error	0.126014	100.00%	0.026276	4.795832	0.000
Total	0.126014				

-2 Log likelihood = 61.105548

Tests of Fixed Effects

Term	DF Num	DF Den	F-Value	P-Value
Recoded SampleLocation	1.00	46.00	1.02	0.317
TimePoint	3.00	46.00	0.91	0.442
Recoded SampleLocation*TimePoint	3.00	46.00	0.24	0.865

Figure C7 Mixed model ANOVA result for experimental groups of Pure Diffusion, CC5, and CC10 for imaging results.

Median Intensity

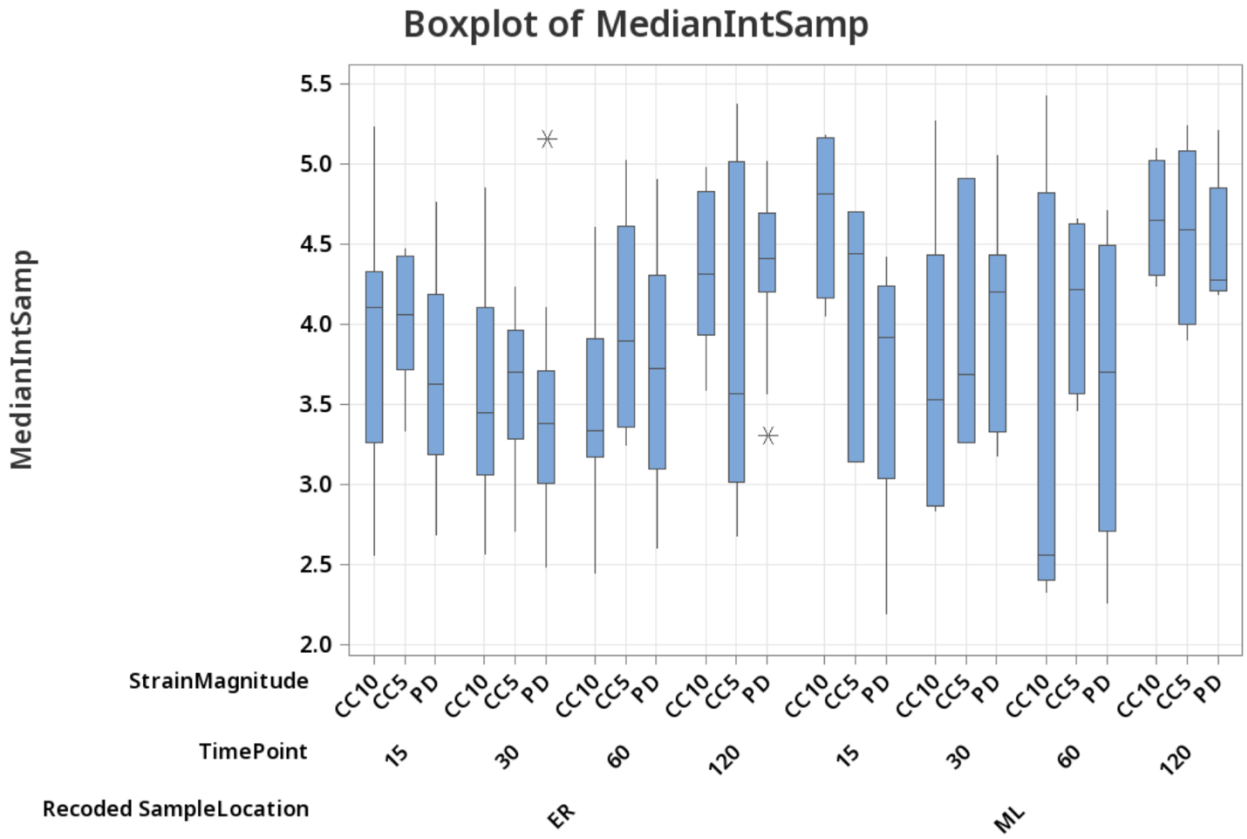

Figure C8 Boxplots of Median Intensity for each group.

Variance Components

Source	Var	% of Total	SE Var	Z-Value	P-Value
specimanID	0.014940	3.05%	0.020652	0.723417	0.235
Location	0.029261	5.97%	0.024646	1.187216	0.118
Error	0.445707	90.98%	0.049765	8.956229	0.000
Total	0.489907				

-2 Log likelihood = 474.946491

Tests of Fixed Effects

Term	DF Num	DF Den	F-Value	P-Value
Recoded SampleLocation	1.00	160.43	4.82	0.029
StrainMagnitude	2.00	95.69	1.03	0.361
TimePoint	3.00	174.92	7.69	0.000
Recoded SampleLocation*StrainMagnitude	2.00	160.43	0.22	0.800
Recoded SampleLocation*TimePoint	3.00	160.43	0.69	0.560
StrainMagnitude*TimePoint	6.00	168.21	2.05	0.061
Recoded SampleLocation*StrainMagnitude*TimePoint	6.00	160.43	0.78	0.587

Figure C9 Results of mixed model ANOVA with dependent variable of median intensity.

Tukey Simultaneous Tests for Differences of Means

Difference of Recoded SampleLocation Levels	Difference of Means	SE of Difference	DF	Simultaneous 95% CI	T-Value	Adjusted P-Value
ML - ER	0.236	0.107	160.428	(0.024, 0.448)	2.20	0.029

Tukey Simultaneous Tests for Differences of Means

Difference of TimePoint Levels	Difference of Means	SE of Difference	DF	Simultaneous 95% CI	T-Value	Adjusted P-Value
30 - 15	-0.243	0.167	177.897	(-0.676, 0.190)	-1.46	0.466
60 - 15	-0.258	0.164	173.978	(-0.684, 0.168)	-1.57	0.397
120 - 15	0.402	0.165	173.432	(-0.026, 0.829)	2.44	0.074
60 - 30	-0.015	0.161	171.763	(-0.433, 0.403)	-0.09	1.000
120 - 30	0.645	0.162	178.570	(0.224, 1.066)	3.98	0.001
120 - 60	0.660	0.154	175.594	(0.259, 1.061)	4.27	0.000

Individual confidence level = 98.97%

Figure C10. Simple main effect comparisons for imaging location, and time points, respectively.

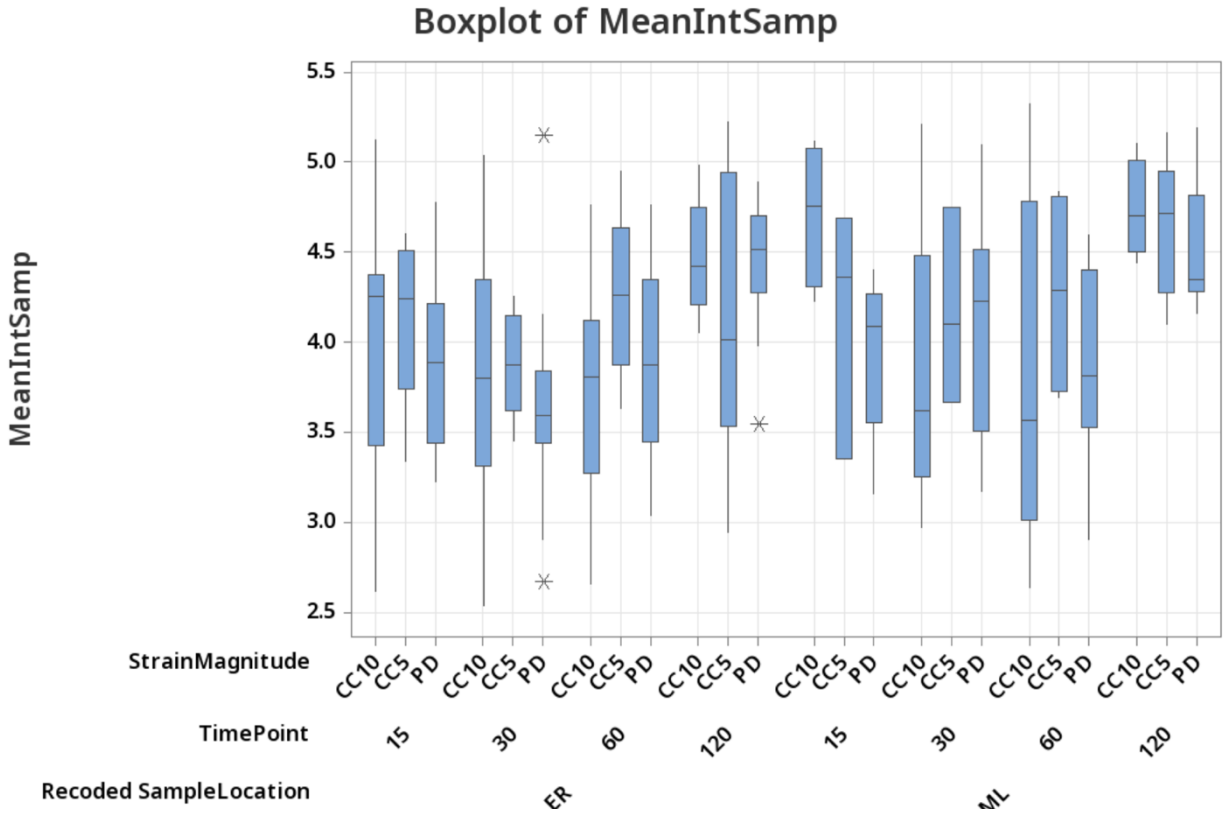

Figure C11. Box plot of mean intensity results for each group and timepoint in the imaging experiments.

Variance Components

Source	Var	% of Total	SE Var	Z-Value	P-Value
specimanID	0.020661	6.46%	0.018377	1.124245	0.130
Location	0.021770	6.81%	0.016948	1.284535	0.099
Error	0.277384	86.73%	0.030828	8.997931	0.000
Total	0.319815				

-2 Log likelihood = 393.752412

Tests of Fixed Effects

Term	DF Num	DF Den	F-Value	P-Value
Recoded SampleLocation	1.00	161.93	5.31	0.022
StrainMagnitude	2.00	124.76	1.84	0.162
TimePoint	3.00	174.16	7.91	0.000
Recoded SampleLocation*StrainMagnitude	2.00	161.93	0.25	0.783
Recoded SampleLocation*TimePoint	3.00	161.93	0.51	0.674
StrainMagnitude*TimePoint	6.00	168.33	1.67	0.130
Recoded SampleLocation*StrainMagnitude*TimePoint	6.00	161.93	0.82	0.558

Figure C12. Mean intensity results for mixed model ANOVA of imaging experiments.

Tukey Simultaneous Tests for Differences of Means

Difference of Recoded SampleLocation Levels	Difference of Means	SE of Difference	DF	Simultaneous 95% CI	T-Value	Adjusted P-Value
ML - ER	0.1952	0.0847	161.926	(0.0280, 0.3624)	2.30	0.022

Individual confidence level = 95.00%

Tukey Simultaneous Tests for Differences of Means

Difference of TimePoint Levels	Difference of Means	SE of Difference	DF	Simultaneous 95% CI	T-Value	Adjusted P-Value
30 - 15	-0.167	0.132	176.755	(-0.511, 0.176)	-1.26	0.588
60 - 15	-0.149	0.131	173.238	(-0.488, 0.191)	-1.14	0.667
120 - 15	0.369	0.130	172.897	(0.030, 0.707)	2.83	0.027
60 - 30	0.019	0.128	170.998	(-0.314, 0.351)	0.14	0.999
120 - 30	0.536	0.129	177.883	(0.202, 0.871)	4.16	0.000
120 - 60	0.518	0.123	174.476	(0.199, 0.836)	4.22	0.000

Individual confidence level = 98.97%

Figure C13. Simple main effects for locations (top) and timepoints (bottom) using mixed model ANOVA.

Table C1. Summary statistics for each strain magnitude at beginning, peak and equilibrium (mean ± standard error).

Strain Magnitude	*Beginning*	*Peak*	*Equilibrium*
Impermeable	4.47±0.50	4.89±0.26	3.55±0.76
Pure Diffusion	2.95±0.58	9.11±1.75	4.84±1.31
Pre-load only	5.41±1.35	18.58±7.40	4.56±0.83
5% mean strain	14.32±5.96	21.19±8.76	8.07±3.30
10% mean strain	5.52±1.18	13.70±5.49	5.23±1.37